UNIVERSITY OF SOUTHAMPTON

FACULTY OF ENGINEERING, SCIENCE, AND MATHEMATICS
School of Chemistry

# Estimations of dipolar couplings in multiple-spin systems by solid-state NMR

ANDREA C. SAUERWEIN

Thesis for the degree of Doctor of Philosophy

August 2010

UNIVERSITY OF SOUTHAMPTON

ABSTRACT

FACULTY OF ENGINEERING, SCIENCE, AND MATHEMATICS
SCHOOL OF CHEMISTRY

Doctor of Philosophy

# ESTIMATIONS OF DIPOLAR COUPLINGS IN MULTIPLE-SPIN SYSTEMS BY SOLID-STATE NMR

by Andrea C. Sauerwein

Dipolar couplings contain valuable structural information, since they are proportional to the inverse cube of the distance between the two spins in a spin-pair. This distance information can then be used in structure calculations of molecules such as polymers, glasses and biomolecules e.g. proteins or DNA. One of the major challenges in solid-state NMR, however, is the determination of the dipolar coupling of a spin-pair within a multiple-spin system, especially in the case of weak couplings. Those weak couplings are often attenuated by the presence of stronger couplings and thus are hard to determine.

In this thesis the problem of dipolar coupling estimations in multiple-spin systems is addressed and a new methodology to overcome the current difficulties is discussed. This novel method combines spherical tensor analysis (STA) and off-magic angle spinning to enable estimations of dipolar couplings in a spin echo-based experiment. Experiments are conducted using a switched-angle spinning probe which permits a precise mechanical switching of the rotation angle up to 20° off the magic angle, along with an independent measurement of the spinning angle via a Hall-effect device. To combine spherical tensor analysis with a spin echo experiment it is necessary to introduce into the pulse sequence rotations around an appropriate set of Euler angles. This is accomplished by converting the Euler angles into a set of phases that can be applied to the pulse sequence. The effect of the inserted rotation is a modulation of the general spherical signal component according to the corresponding Wigner matrix element. To select spherical signal components resembling a specific rank-component-pathway during the experiment, it is necessary to utilise N such pulse sequences–each having a different NMR signal corresponding to a new set of Euler angles. Spherical signal components may then be constructed from a linear superposition of the experimental data. If the STA of the spin echo experiment is carried out at several spin echo times it is possible to follow a time dependent build-up of the spherical signal components. This build-up is sensitive to the dipolar coupling strength. The robustness of this method derives from the facility to correct build-up curves for relaxation-induced dampening, given the assumption that the relaxation of higher-rank spherical tensors is equal to that of the rank one spherical tensors.

# Contents

# List of Figures

# List of Tables

**Declaration of Authorship**

I, Andrea C. Sauerwein, declare that the thesis entitled “Estimations of dipolar couplings in multiple-spin systems by solid-state NMR” and the work presented in the thesis are both my own, and have been generated by me as the result of my own original research. I confirm that:

- this work was done wholly or mainly while in candidature for a research degree at this University;
- where any part of this thesis has previously been submitted for a degree or any other qualification at this University or any other institution, this has been clearly stated;
- where I have consulted the published work of others, this is always clearly attributed;
- where I have quoted from the work of others, the source is always given. With the exception of such quotations, this thesis is entirely my own work;
- I have acknowledged all main sources of help;
- where the thesis is based upon work done by myself jointly with others, I have made clear exactly what was done by others and what I have contributed myself;
- none of this work has been published before submission.

Signed: .....
Date: .....

*For my parents, who encouraged me,*
*and for Greg, who is there for me.*

# Acknowledgements

I would like to thank my supervisor, my colleagues, my friends and my family for the various types of support they offered me during my PhD.

Special thanks go to my supervisor Malcolm H. Levitt, for having faith in the dipolar recoupling project and for pushing it forward. His ability to give simple explanations of difficult concepts often helped me to get started on a new methodology and his encouragement throughout the thesis was invaluable especially when the project — as was so often the case — seemed to hit a dead end.

All past and present members of the Levitt group have been very supportive and we had a lot of stimulating discussions.

I would like to thank Ildefonso Marin-Montesinos for introducing me to the research topic of recoupling in multiple-spin systems and for a very intensive introduction to the hardware and software available in our laboratory.

When I started writing my own pulse programs it was Marina Carravetta who took the time to explain the pulse programming on our Varian and Bruker systems. Throughout my PhD she has been very supportive and answered many practical questions.

I would like to thank Ole G. Johannessen for sharing his technical knowledge and for always helping out when the equipment did not work as expected. He helped Salvatore Mamone and I and later Pierre Thureau and I with the difficulties we encountered when setting up the SAS-DOTY-probe.

I enjoyed sharing periods of the homonuclear recoupling project with Sergey

Maltsev, Pierre Thureau and Maria Concistrè. I would like to thank them for their collaboration as well as Michael Tayler who was involved in some theoretical aspects of the research.

I experienced great assistance from Maria Concistrè, Giuseppe Pileio, Michael Tayler and Malcolm H. Levitt when encountering experimental difficulties towards the end of my PhD thesis. We would all spend long hours in the lab to track down the problem.

I would also like to thank people from outside Southampton, including P. K. Madhu, Mithun Goswami and Subhradip Paul from whom I learned a lot about homonuclear decoupling. Furthermore, I would like to thank everyone who discussed my research at Chamonix in 2009, at the FMP (Leibniz-Institut für Molekulare Pharmakologie) in December 2009, and at the EUROMAR 2010 for their feedback.

I would also like to thank the EPSRC for funding.

# Part I

# Introduction

Chapter 1

# Introduction

Towards the end of 1945 the first successful nuclear magnetic resonance (NMR) experiments were carried out independently by Edward M. Purcell, Henry C. Torrey and Robert V. Pound [1] and by Felix Bloch, William W. Hansen and Martin Packard [2]. While Purcell and co-workers carried out their work in the solid-state using paraffin wax as a sample, Bloch and co-workers detected their first NMR signal from the protons of liquid water. For their discovery Purcell and Bloch shared the Nobel Prize in Physics in 1952.

Although NMR originated in physics its application is by no means restricted to physics and since its discovery it has entered different fields such as chemistry, biochemistry and medicine, where it is a valuable tool for the investigation of matter. NMR in the liquid-state developed rapidly and is now routinely used to access information of molecular structures and dynamics. The development of NMR in the solid-state was not as rapid as it faced several difficulties; overcoming these was the main focus of research in the first decades of solid-state NMR. The techniques developed during this period allowed research in solid-state NMR to move on to the development of methods that allow the characterisation of structure and dynamics in complex molecules, especially of those that do not admit to alternative techniques.

This thesis is divided into three parts. In **Part I** I will give an introduction to the basic principles of NMR followed by a description of the difficulties solid-state NMR had to overcome. The resulting standard techniques or the "tool box" of solid-state NMR is established and the aim of my thesis in context with the recent literature is discussed. **Part II** introduces the theoretical concepts of solid-

state NMR as well as two methodologies: dipolar recoupling and spin-echoes. Both methods are basic concepts relating to the research conducted during my PhD, which is presented in **Part III** of this thesis.

Chapter 2

# Basic Principles of Nuclear Magnetic Resonance

## 2.1. Spin Angular Momentum and Magnetic Moment

Particles for which there is no known division into smaller units are called elementary particles. They possess four intrinsic physical properties: mass, electric charge, magnetism and *spin*. While there is a macroscopic counterpart for mass, electrical charge and magnetism allowing us to visualise these properties, there is no such macroscopic counterpart for spin. Thus it difficult to envisage the spin of a particle. Since spin is an intrinsic angular momentum (*spin angular momentum*) and it is not produced by a rotation of the particle it can be described best by quantum mechanics. The magnitude of the spin angular momentum is quantised and its allowed values are given by $\hbar\sqrt{S(S+1)}$, where $\hbar$ is Plank's constant divided by $2\pi$ ($h = 6.62608 \cdot 10^{-34} J \cdot s$) and S is called the *spin quantum number*.

Atoms consist of electrons and nuclei. While electrons are elementary particles themselves nuclei are composed of protons and neutrons, which themselves consist of elementary particles. Accordingly, the properties of a nucleus depend on the elementary particles it consists of, hence, they determine its nuclear spin. The resulting spin quantum number may have an integer or half-integer value. However, only those nuclei with a non-zero spin quantum number possess the magnetic moment necessary to induce an NMR signal. Almost all elements of the periodic table have at least one isotope with a non-zero spin angular momentum. In my thesis I will solely consider those nuclei with a spin quantum

number of $S = 1/2$. Among the most common nuclei in organic solids which posses spin-1/2 are $^{1}$H, $^{13}$C, $^{15}$N and $^{31}$P.

The spin angular momentum can be described a vector $\mathbf{S}$ and its direction is known as the *spin polarisation axis*. Those nuclei with a non-zero spin posses a microscopic *magnetic moment*, represented by the vector $\boldsymbol{\mu}$, which is parallel or anti-parallel to the spin angular momentum:

$$\boldsymbol{\mu} = \gamma \mathbf{S} \tag{2.1}$$

where the proportionality constant $\gamma$ is called *gyromagnetic ratio* or *magnetogyric ratio* and is characteristic for each isotope. Properties of frequently used spin-1/2 nuclei and some of their isotopes are listed in Table 2.1.

Table 2.1: A selection of nuclear isotopes and their properties.

| Nucleus | Spin in the ground state | Natural abundance /% | Gyromagnetic ratio / $10^6 \cdot rad \cdot s^{-1} T^{-1}$ |
|---|---|---|---|
| $^{1}$H | 1/2 | 99.985 | 267.522 |
| $^{2}$H | 1 | 0.014 | 41.066 |
| $^{3}$H | 1/2 | 0 | 285.349 |
| $^{12}$C | 0 | 98.9 | - |
| $^{13}$C | 1/2 | 1.1 | 67.283 |
| $^{14}$N | 1 | 99.6 | 19.338 |
| $^{15}$N | 1/2 | 0.37 | -27.126 |
| $^{31}$P | 1/2 | 100 | 108.394 |

## 2.2. Larmor Precession

NMR experiments are conducted on samples containing a large number of nuclear spins, usually $> 10^{14}$, which interact with each other and with the external magnetic field. Typically, the interactions between molecules in a sample are regarded as small, thus a single molecule is considered an isolated spin-system. The sum of all molecules/isolated spin-systems in the sample is called the *spin ensemble*.

In the absence of an external magnetic field, the orientations of the spin polarisation axes in a spin ensemble are random, i.e. all orientations are equally represented, and therefore do not give rise to any macroscopic magnetic moment. If a magnetic field is applied the spin polarisation responds by precessing around the field, hence, also the microscopic magnetic moment of the spin precesses. This response is called *Larmor precession*. The magnetic moment moves on a cone (Figure 2.1) keeping a constant angle between the spin magnetic moment and the field, where the angle depends only on the initial polarisation of the spin. It is important to note that the nuclear magnetic moments do not align along the external magnetic field, however, there is a weak alignment with the field.

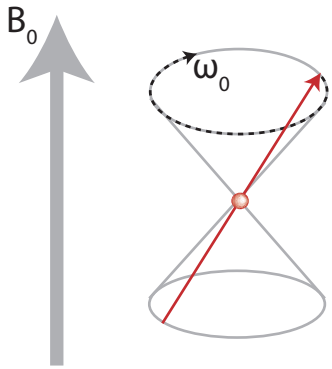


Figure 2.1: Spin precession for a spin possessing $\gamma > 0$.

The Larmor precession is associated with a precession frequency, the *Larmor frequency*:

$$\omega_0 = -\gamma B_0 \tag{2.2}$$

which is directly proportional to the strength of the external magnetic field $B_0$ with the gyromagnetic ratio being the proportionality constant. The sign of $\gamma$ determines the direction of rotation of the Larmor frequency. Spins possessing a negative $\gamma$ have a positive Larmor frequency and rotate anti-clockwise, while those with a positive $\gamma$ have a negative Larmor frequency and rotate clockwise.

## 2.3. Longitudinal Magnetisation

Nuclear magnetic moments are not completely isolated from their molecular environment and are consequently subject to the thermal motion of that environment. Slight fluctuations of the local magnetic fields result in *relaxation* of the

ensemble of magnetic moments into *thermal equilibrium*. In thermal equilibrium the probability of a given nuclear magnetic moment having a component parallel to the external magnetic field is slightly higher than having a component anti-parallel to the external field. The resulting macroscopic net magnetic moment is called *longitudinal magnetisation* and the time it needs to re-establish after thermal equilibrium is disturbed is the *longitudinal* or *spin-lattice relaxation time* denoted $T_1$. However, the excess between those components oriented parallel rather than anti-parallel to the external field is tiny — in the order of $10^{-5}$ — and is described by the *magnetisation vector* $\mathbf{M}$ (Figure 2.2.a).

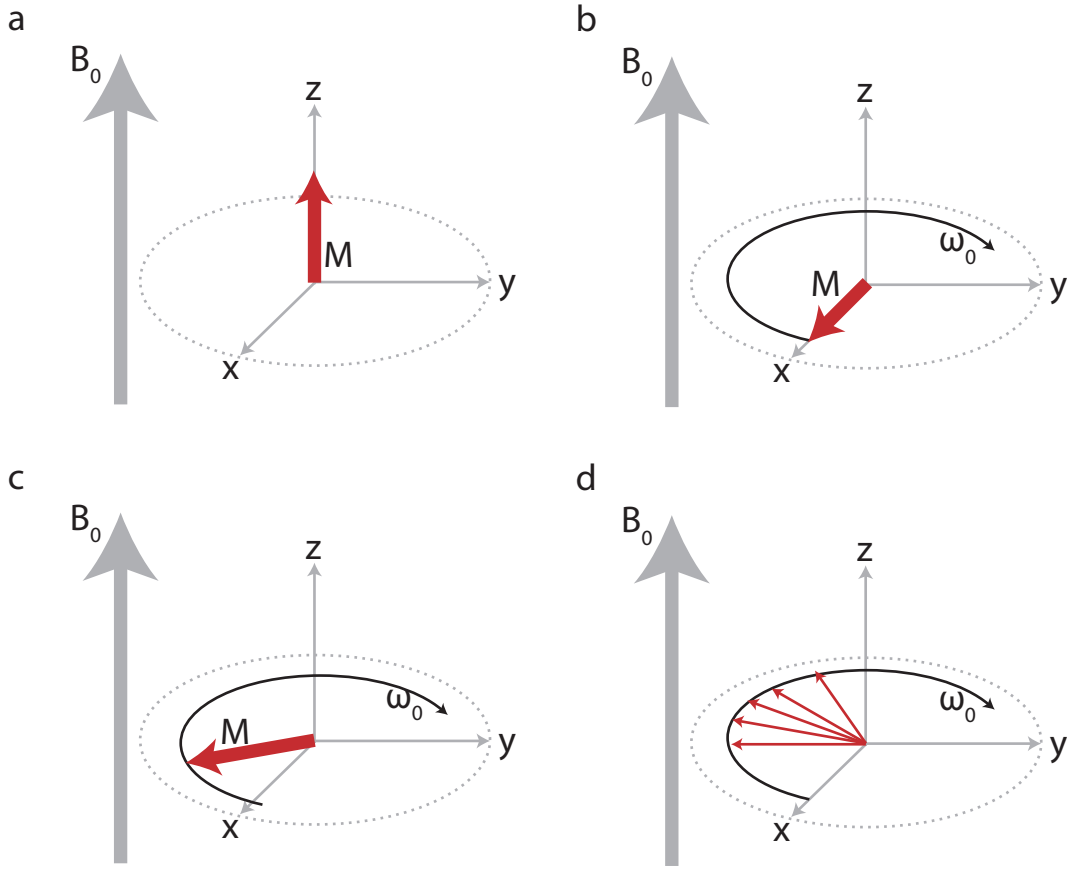


Figure 2.2: (a) The magnetisation vector, $\mathbf{M}$, of a spin ensemble at thermal equilibrium — longitudinal magnetisation. (b) Magnetisation vector after the application of an rf-pulse with a 90°rotation around the y-axis — transverse magnetisation. The magnetisation precesses with the Larmor frequency $\omega_0$ around the field. (c) Transverse magnetisation after some time. (d) After a certain time the transverse magnetisation loses synchrony or coherence.

## 2.4. Transverse Magnetisation and the NMR Signal

Longitudinal magnetisation is very difficult to detect, a difficulty that can be overcome by rotating it into the xy-plane perpendicular to the main magnetic field (Figure 2.2). The rotation of magnetisation is achieved by applying a radio-frequency (rf) pulse — an oscillating magnetic field of a particular duration applied perpendicular to the main field — that rotates all single nuclear magnetic moments by 90°around an axis in the xy-plane transferring the macroscopic net magnetisation into the xy-plane, where it is described as *transverse magnetisation*.

Once the rf-pulse is switched off the single spins precess at their Larmor-frequency around their individual cones. It is the single spin precession which causes the transverse magnetic moments to precess around the external field (Figure 2.2.c-d), while it precesses at the Larmor frequency it is slowly decaying. This decay is a macroscopic phenomenon that depends on the slightly fluctuating microscopic fields, which results in the loss of synchrony between the precessing single magnetic moments. Inevitably, the spin distribution in the xy-plane will be random, hence, the signal will be lost. This process is called *homogeneous decay* and parametrised by the *transverse relaxation time constant* $T_2$.

In an NMR set-up the sample is surrounded by a wired coil which picks up the electrical current induced by the precession of the spins in the sample. This oscillating current is the *NMR signal* or *free induction decay (FID)*. Usually, the NMR signal is the sum of different oscillating modes and can be very complex. Figure 2.3.a-c shows schematically how the NMR signal of two different oscillating modes looks.

Each oscillating mode corresponds to a different spin in an isolated spin-system precessing at its own Larmor frequency. However, it is difficult to analyse the FID, where the response is an amplitude given as a function of time; and is a lot easier to analyse a spectrum in which the amplitude is given as a function of frequency. Such a spectrum can be obtained from the time domain NMR signal by a mathematical transformation called *Fourier transformation* (Figure 2.3.d-f).

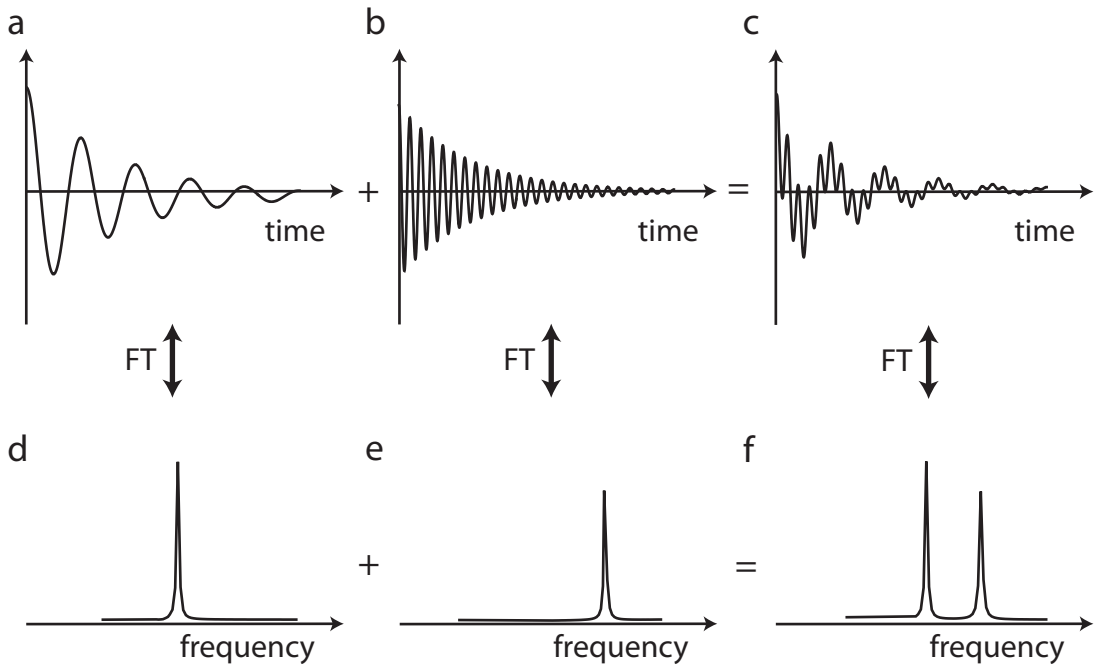


Figure 2.3: An NMR signal composed of two different oscillating modes present in a sample. The oscillating modes (a) and (b) originate from different spins in an ensemble. Their sum (c) is the NMR signal that would be acquired. For analysis purposes the FIDs (a-c) are Fourier transformed to give the NMR spectrum (d-f), a process that is reversible. Generally NMR signals are complex numbers, in which the x-component of the magnetisation forms the real part while the y-component of the magnetisation forms the imaginary part. For simplicity this Figure shows only the real part of the signal.

## 2.5. NMR Interactions

So far, the discussion has concentrated on external NMR interactions i.e. the interactions between nuclear spins and the external magnetic fields. In addition to those external interactions, there are internal interactions which comprise of spins' interactions with their molecular surroundings.

The external magnetic field induces a current in the electron clouds of a sample, which in turn induces a magnetic field. This induced field is experienced by the nuclear spins in addition to the external magnetic field and results in a local magnetic field, which now contains information about the electronic (viz. chemical) structure of the sample. The effect of a local magnetic field on a spin is observed as small difference in the Larmor frequencies of nuclear spins from

different surroundings, and is referred to as *chemical shift*. It is this interaction that is regarded as a spin's "finger-print".

The through space interaction of two nuclear spins is often expressed as the *direct dipole-dipole coupling* or *direct dipolar coupling*, which is proportional to the gyromagnetic ratios of the involved spins and inversely proportional to the cube of the internuclear distance, $r$. Figure 2.4 indicates the range of dipolar couplings for different spin-pairs. Due to their distance dependence, these dipolar couplings are important for molecular structure determinations.

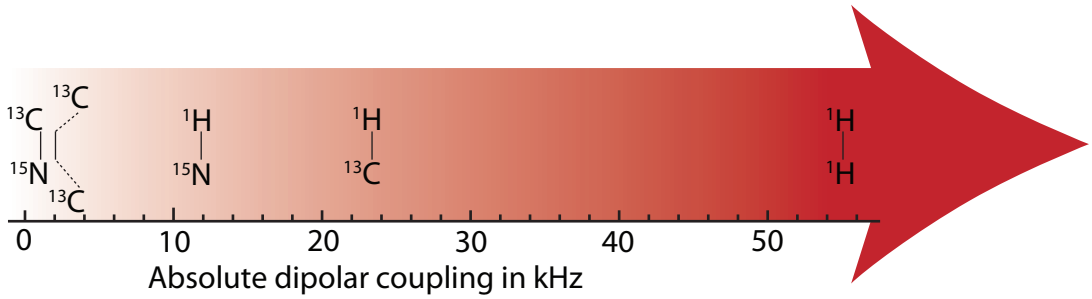


Figure 2.4: The dipolar coupling strengths of frequent spin-pairs in organic compounds are shown, favouring those that are commonly investigated by NMR. Most dipolar couplings indicated are calculated from their average single bond distance, which is 1.47 Å for a $^{13}$C–$^{15}$N single bond, 1.54 Å for a $^{1}$H–$^{15}$N single bond, 1.01 Å for a $^{13}$C–$^{13}$C single bond and 1.09 Å for a $^{1}$H–$^{13}$C single bond. The $^{1}$H–$^{1}$H dipolar coupling, however, is calculated from an intra-methylene group distance of 1.3 Å.

Another spin-spin interaction is the *J-coupling*, also called *indirect dipole-dipole coupling* or *scalar coupling*, where spins do not interact directly with each other, but rather indirectly via bonding electrons. J-couplings exist between adjacent nuclei such as $^{13}$C–$^{13}$C and $^{1}$H–$^{13}$C

The spin-spin interactions described above can occur not only between nuclear spins of the same chemical element, but also between spins of different chemical elements. These interactions are described as *homonuclear* and *heteronuclear*, respectively.

## 2.6. The NMR Experiment

Rf-pulses are the main tool for spin manipulation in NMR spectroscopy; they allow the spectroscopists to control the nuclear spins by suppressing and reintro-

ducing spin interactions. Theoretically these manipulations may be performed without restrictions using carefully designed pulse sequences. Such pulse sequences can be complex and involve many pulses. A pulse sequence is usually depicted by representing each rf-pulse by a rectangle whose height and breadth symbolise its amplitude and duration respectively. A “single excitation” pulse sequence that can be used to excite transverse magnetisation (Figure 2.2.b) is depicted in Figure 2.5. The pulse, i.e. an oscillating magnetic field, is applied along the y-axis, which rotates the net magnetisation **M** around a flip-angle of $(\pi/2)$ rad$\cdot$s$^{-1}$ into the xy-plane. To yield an efficient rotation, the frequency of the pulse — the so called *resonance frequency* — is chosen such that it is resonant to the absolute value of the Larmor frequency.

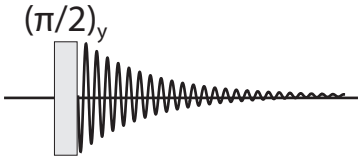


Figure 2.5: Diagram of the single excitation pulse sequence used to excite transverse magnetisation. The flip-angle of the pulse is $\pi/2$ with a phase y, which indicates a rotation about the y-axis.

If experiments involve spins from more than one chemical element then each element is irradiated at its own Larmor frequency. Consequently, the pulse sequence diagrams contain a row for the pulse sequences applied at each Larmor frequency.

Chapter 3

# Introduction to Solid-State NMR

One of the major differences between solid- and liquid-state NMR is that spectra in the solid-state are much broader than those observed in the liquid-state. By way of illustration, consider the case of water in its liquid and solid states. Liquid water has a proton linewidth of 0.1 Hz compared to $10^5$ Hz observed for ice at low temperature so that the solid-state linewidth is six orders of magnitude broader [3]. A schematic representation of the differences in linewidth between water and ice is shown in Figure 3.1.

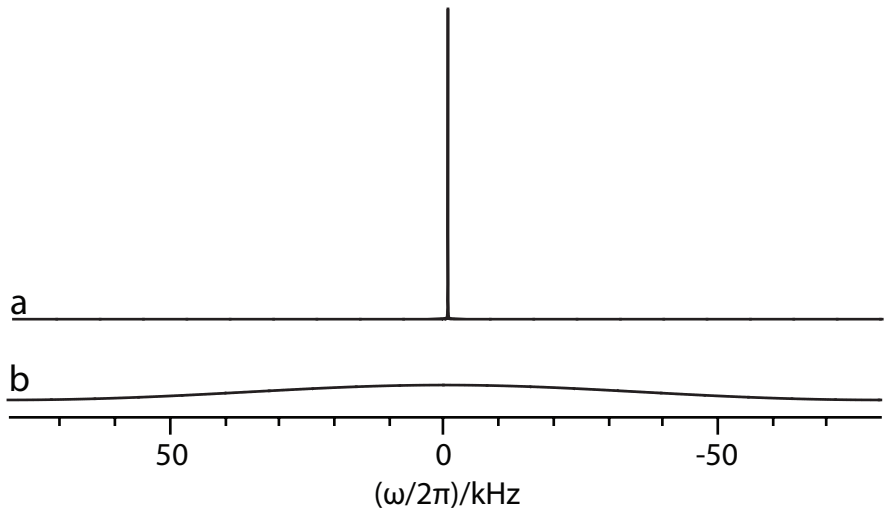


Figure 3.1: Schematic representation of a $^1$H-NMR spectrum to illustrate the differences in linewidth and sensitivity observed between (a) a liquid sample such as water at room temperature and (b) a solid sample such as ice at low temperature.

## 3.1. Different Phases of Matter in NMR

The difference in linewidth between the solid- and the liquid-state originates from the different interactions that are manifested in different physical states of matter. Generally, interactions can be distinguished between those which are *isotropic* i.e. they are uniform in all directions such that the observed value does not depend on the direction, and those which are *anisotropic* i.e. the observed value is different when measured in different directions.

There are two types of liquids, *isotropic liquids* and *anisotropic liquids*. In isotropic liquids molecules undergo translational and rotational mobility (Figure 3.2) which is fast compared to the inverse size of the NMR interactions. Subsequently, anisotropic interactions are averaged to zero and only the isotropic parts of the interactions are observed. It is this averaging of the anisotropic interactions that causes the improved resolution and sensitivity manifested as narrow line in the spectrum of an isotropic liquid (Figure 3.1.a). However, this happens at the expense of losing valuable information that is encoded in the anisotropic interactions.

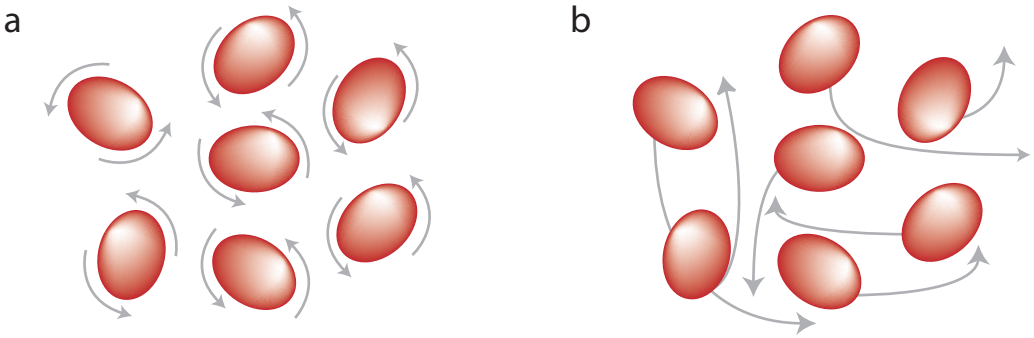


Figure 3.2: Molecular motions in a liquid. (a) rotational mobility and (b) translational mobility. In an isotropic liquid all motion is uniform in all directions.

Contrary to isotropic liquids, anisotropic liquids posses orientational order. A common example of such anisotropic liquids are liquid crystals, which have a preferential ordering with respect to each other resulting from their physical properties such as their shape (Figure 3.3).

This thesis, however, is concerned with the NMR of solid compounds. Solids are characterised by their structural rigidity and resistance to changes in shape or volume. The atoms in a solid are tightly bound to each other, either in a regular

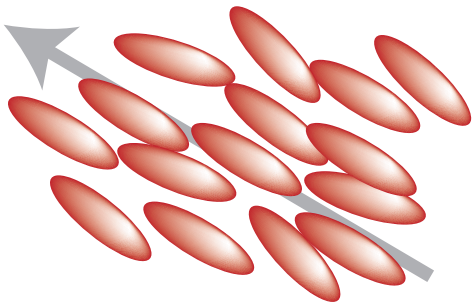

Figure 3.3: Schematic representation of an anisotropic liquid. The molecular mobilities depend on their direction in space.

geometric lattice or irregularly. Solids that posses a regular geometric lattice are called *crystalline solids* (e.g. common salt/sodium chloride) opposed to those in an irregular lattice which are described as *amorphous solids* (e.g. common window glass). The restricted motion in solids causes the anisotropic interactions to be readily observed in most solids and information from these interactions may be exploited. However, it is often very difficult to produce crystalline solids of appropriate size and instead of working with so called *single crystals* it is common in NMR to work with *powdered samples* which typically consist of in the order of $10^8$ crystallites. Each of these crystallites is randomly oriented with re-

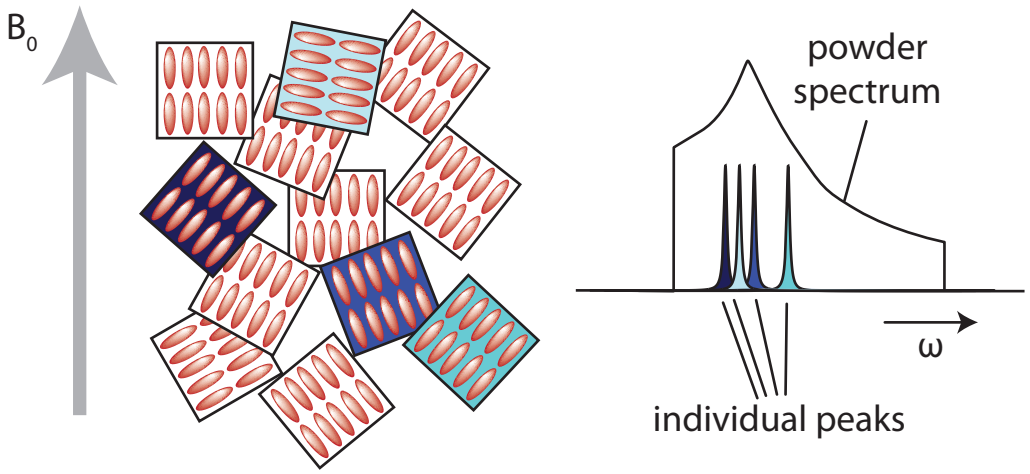


Figure 3.4: The formation of a powder pattern is indicated here. Each crystallite in a powdered samples has an orientation depended contribution to the powder spectrum.

spect to the magnetic field and gives an orientation dependent NMR signal. The solid-state NMR spectrum of a powdered sample corresponds to the the super-

position of signals from each crystallite, which usually results in a broad shape with sharp corners called *powder pattern* (Figure 3.4). For the remainder of this thesis such powdered samples will be studied.

## 3.2. Magic-Angle Spinning

The differences in resolution and sensitivity of NMR spectra of liquids and solids resulted in a rapid development of liquid-state NMR for the analysis of molecular structure and dynamics. Solid-state NMR would have probably never become an important tool for structure determination, if Andrew *et al.* [4; 5] and Lowe [6] had not independently sought to emulate nature and successfully removed the anisotropic broadening from the spectra by rapidly spinning the solid sample around an axis known as the *magic angle*. At the magic angle, $\beta_{RL}$, the angle between the static magnetic field ($B_0$) and the axis of rotation ($z_R$) becomes $\arctan\sqrt{2} \approx 54.74°$ (Figure 3.5).

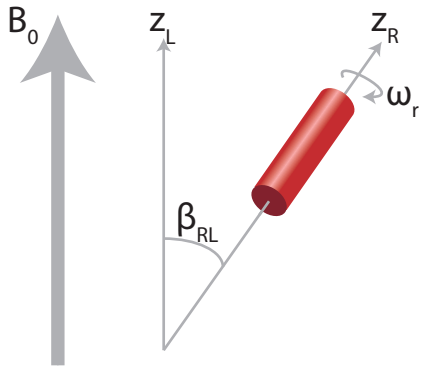


Figure 3.5: Schematic representation of magic-angle spinning of a rotor with the spinning frequency $\omega_r$ around the rotor axis $z_R$. $B_0$ is the external magnetic field and $\beta_{RL}$ is the angle between the static magnetic field ($B_0$) and the axis of rotation ($z_R$), here, it is set to the magic angle.

The extent to which the anisotropic interactions are averaged depends on the frequency of the rotation. Homogeneous interactions, such as the homonuclear dipolar coupling, require fast rotation compared to the interaction — manifested in the linewidth of the static spectrum — to achieve an appreciable narrowing of the resonance. If this rotation is sufficiently fast *magic-angle spinning* (MAS) can average those anisotropic interactions to zero. If the rotation is slower than that satellite lines known as spinning side-bands appear at multiples of the rotation rate. Inhomogeneous interactions, such as the chemical shift anisotropy,

however, show significantly narrowed linewidth even at slow sample rotations. The effect of MAS at different spinning frequencies ($\omega_r/2\pi$) on an NMR spectrum of a powder of glycine is shown in Figure 3.6.

## 3.3. Heteronuclear Decoupling

It is often desirable to study a dilute spin species, such as $^{13}$C and $^{15}$N (denoted S), while suppressing the dipolar couplings between these spins and abundant nuclei, such as $^{1}$H (denoted I). However, these dipolar couplings are often too strong (Figure 2.4) to be averaged to zero by MAS at moderate spinning frequencies and as a result broad lines are observed in the NMR spectrum. The sensitivity and the resolution of the S-spin NMR spectrum can be greatly increased by *heteronuclear decoupling*. The simplest, and until the mid 1990's, also most common method to achieve decoupling in solids is the application of a strong unmodulated rf-field close to the Larmor frequency of the I-spins. This method is called *continuous wave* or *CW decoupling* [7]. The rf-field on the I-spins rotates them continuously, which causes the heteronuclear couplings to be averaged, at the same time the S-spins are unchanged. Decoupling has advanced in recent years and the applied rf-field is often modulated in phase, frequency, and/or amplitude resulting in better performance — i.e. narrower lines — than CW-decoupling. In particular, the two-pulse phase-modulation (TPPM) method [8], SPINAL-64 [9] and similar schemes consistently produce better decoupling [10; 11; 12] than is observed with the CW method.

## 3.4. Cross Polarisation

Magic-angle spinning was one of the key developments in solid-state NMR, however, despite the vast improvements of resolution due to MAS sensitivity remained an issue if low-$\gamma$ nuclei such as $^{13}$C were to be studied. In order to improve sensitivity the presence of strong dipolar couplings between $^{1}$H and low-$\gamma$ nuclei and the high $^{1}$H polarisation can be exploited for signal enhancement. The experiment, shown in Figure 3.7, is called *cross polarisation* (CP) and was first applied by Pines *et al.* in 1972 on a sample of solid adamantane [13].

In a first step magnetisation on the abundant I-spin (usually $^{1}$H) reservoir is rotated by a $90^{\circ}_{y}$-pulse to produce transverse magnetisation. This is followed by

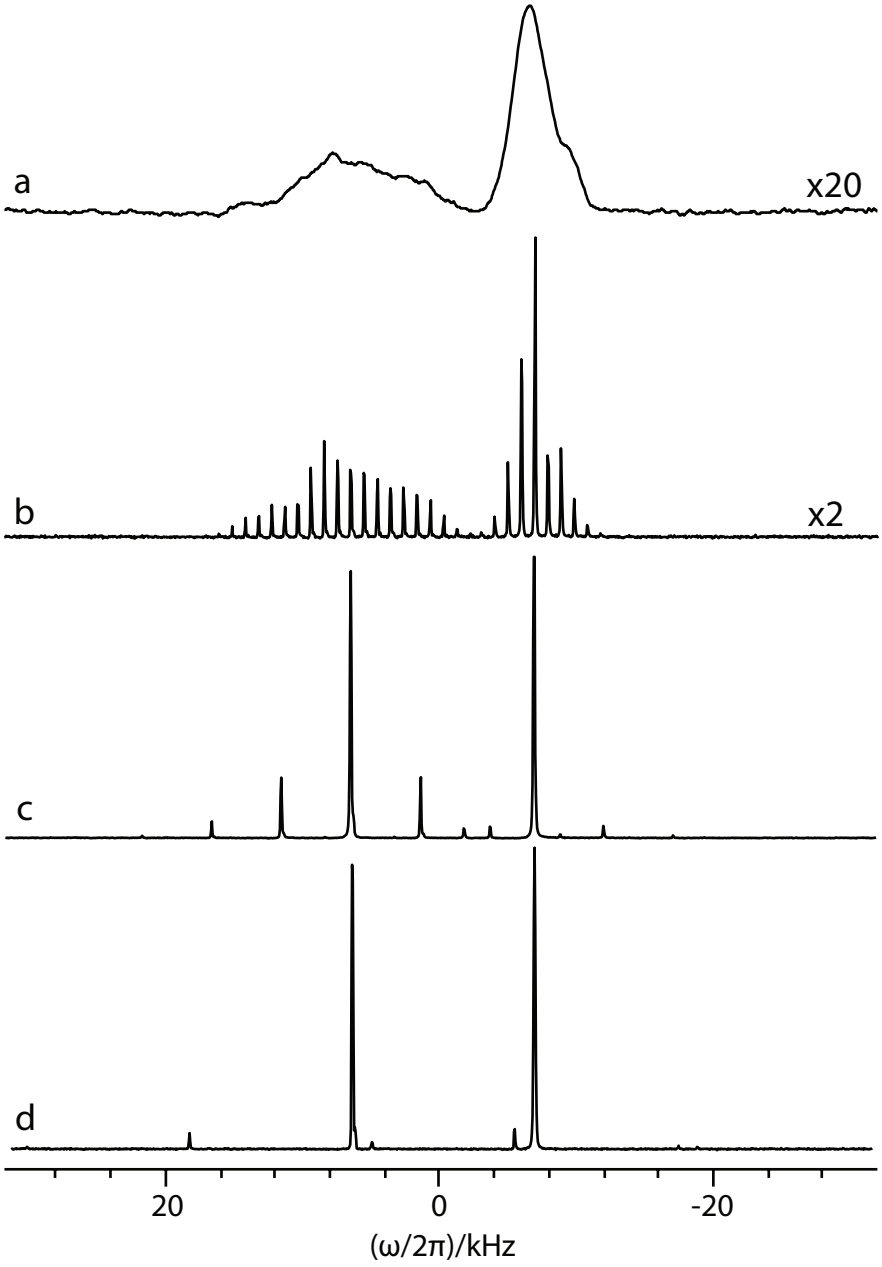


Figure 3.6: $^{13}C$ solid-state NMR spectra of a powdered sample of 99%- U-$^{13}C$-$^{15}N$-$\alpha$-glycine, acquired at a magnetic field of 9.4 T. (a) Spectrum form the static sample. Spectra (b-d) were obtained under MAS at various spinning frequencies $\omega_r$. (b) $\omega_r/2\pi$ = 964 Hz. (c) $\omega_r/2\pi$ = 5088 Hz (d) $\omega_r/2\pi$ = 12000 Hz. As the rotation frequency $\omega_r/2\pi$ increases, the anisotropic interactions are averaged out, manifested by a decrease in side-band amplitude relative to the isotropic chemical shifts.

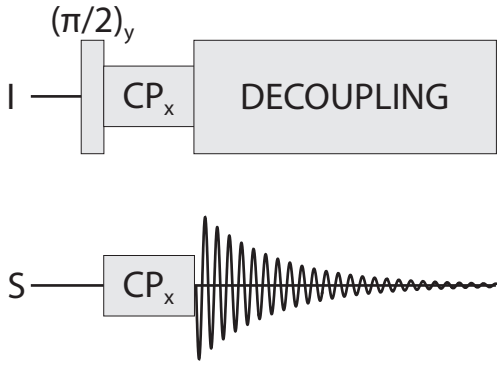


Figure 3.7: Cross polarisation pulse scheme. The scheme consists of two pulse sequences, one applied to the I-spins and one applied to the S-spins. First a $\pi/2$-pulse is applied to the I-spins thus I-spin magnetisation is rotated to the x-axis. Then a spin-lock filed (labelled CP) is applied simultaneously to both spins during which magnetisation is transferred from the I-spins to the S-spins. The enhanced S-spin signal is acquired, while the I-spins are decoupled from the S-spins.

a spin-locking field on the I- and S-spin reservoir. During this period polarisation is transferred from the I-spin reservoir to the S-spin reservoir by matching the Larmor frequencies of the I- and S-spins to the Hartmann-Hahn-condition [14]:

$$|\gamma_I B_{1I}| = |\gamma_S B_{1S}| \tag{3.1}$$

Equation 3.1 is valid under static conditions, whereas the Hartmann-Hahn-condition under magic-angle spinning is given as:

$$|\gamma_I B_{1I}| = |\gamma_S B_{1S}| + n\omega_r, \tag{3.2}$$

where $\omega_r$ is the speed of the sample rotation and n takes an integer value of 1 or 2. The term $n\omega_r$ results from the time dependence that is introduced in the dipolar coupling under magic-angle spinning. More precisely, the heteronuclear dipolar coupling terms which allow cross-polarisation oscillate at $\pm 1\omega_r$ and $\pm 2\omega_r$ while the static cross-polarisation term averages to zero. Thus, cross-polarisation under magic-angle spinning needs to be conducted at the so called sideband matching conditions Eq.3.2.

The spin locking part of the experiment is followed by an acquisition of the S-spins while the I-spins are continuously irradiated to decouple the S-spins from effects of the heteronuclear coupling. The signal enhancement of spins S that

can be achieved by cross polarisation is proportional to $\gamma_I/\gamma_S$. In the case of cross polarisation from $^1$H to $^{13}$C the theoretical maximum sensitivity increase is given by a factor of 4. However, in practice this enhancement is not reached because transfer efficiency is reduced by magic-angle spinning which scales the dipolar coupling and relaxation of $^1$H magnetisation during the spin locking part.

It was only when Schaefer and Stejskal [15] combined cross polarisation and magic-angle spinning to what is now commonly referred to as CP-MAS that MAS became a standard tool in solid-state NMR.

## 3.5. Diluted Spins and Selective Labelling

So far, the discussion of sensitivity and resolution enhancement in solid-state NMR concentrated on the NMR methodology. However, sensitivity can be enhanced by choosing an appropriate sample. It is necessary to distinguish between abundant nuclei like $^1$H which have a natural abundance in excess of 99% and rare nuclei such as $^{13}$C and $^{15}$N which have natural abundances below 2% thus only 2 (or fewer) out of every 100 atoms induce an NMR signal. This leads to the poor sensitivity of rare nuclei compared to abundant nuclei. This, however, can be overcome by chemically enriching the atoms in a molecule with their NMR active isotope producing so called *labelled samples*. It is not only possible to produce uniformly labelled samples, in which all atoms of the same kind are enriched with the NMR active isotope resulting in a multiple-spin system but also to selectively introduce one or more atoms in a molecule. The spin-ensembles in a labelled sample may be isolated from interactions with a neighbouring spin-ensemble by diluting labelled molecules with unlabelled molecules.

## 3.6. Dipolar Recoupling

Solid-state NMR is useful for structure determination in solids because the dipolar coupling between two spins is distance dependent. However, most applications of solid-state NMR require the use of MAS, which averages anisotropic interactions such as the dipolar coupling to zero, and thereby looses the distance information contained therein. It is therefore necessary to selectively reintroduce these interactions, by applying a sequence of rf-pulses that suspends the

averaging effect caused by MAS. The reintroduction of interactions suspended by MAS is generally described as *recoupling*, and the reintroduction of dipolar couplings is referred to as *dipolar recoupling*. The principles of dipolar recoupling by rf-pulses are illustrated in Figure 3.8; the averaging effect of MAS is shown in a), while the simultaneous application of MAS and a rotor synchronised pulse-sequence is shown in b). The application of such a *dipolar recoupling sequence* yields a non-zero dipolar coupling scaled by a factor $\kappa$ that depends on the chosen pulse-sequence.

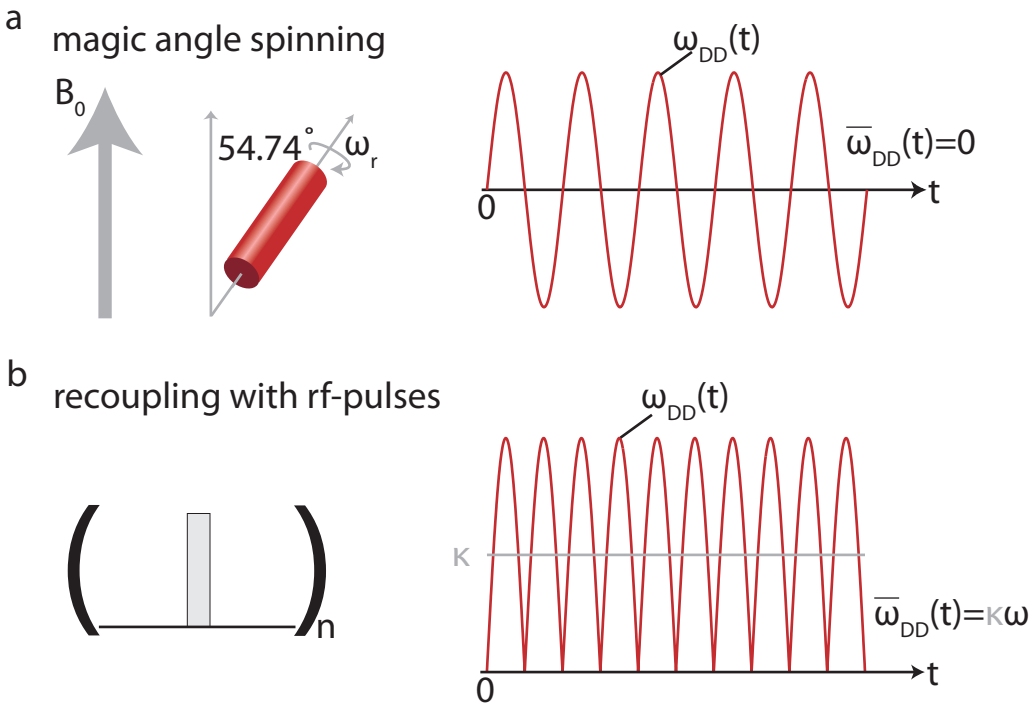


Figure 3.8: Schematic representation of the basic principles of dipolar recoupling under MAS. a) MAS induces an oscillatory behaviour of the dipolar coupling which results in the averaging of the dipolar coupling: $\overline{\omega}_{DD}(t) = 0$. b) In the heteronuclear case the application of a rotor synchronised $\pi$-pulse once per rotor period results in a non-zero dipolar coupling: $\overline{\omega}_{DD}(t) = \kappa\omega_{DD}$, where $\kappa$ is the scaling factor and depends on the chosen recoupling sequence.

Dipolar recoupling sequences are distinguished according to their properties such as the spin-system to which they are applied, their selectivity or the information that is obtained. For the context of this thesis I will focus on dipolar recoupling sequences for distance determination. Consider a two spin system with spins $j$ and $k$ that may be either of the same nucleus — a homonuclear spin system — or of different nuclei — a heteronuclear spin system. The dipolar recoupling techniques for the two cases vary due to differences in the interactions. In both cases

spins $j$ and $k$ can occur as an isolated spin-pair or as part of a multiple-spin system. Historically, dipolar recoupling sequences were developed for isolated spin-pairs in the heteronuclear case with the first recoupling scheme being introduced by Oas *et al.* in 1988 [16]. They not only introduced the rotary resonance recoupling ($R^3$) scheme, but also the term recoupling for the reintroduction of dipolar couplings that are averaged to zero by magic-angle spinning. With REDOR (rotational echo double resonance) [17] another heteronuclear recoupling scheme was introduced, prior to the introduction of the first homonuclear recoupling scheme, DRAMA, by Tycko *et al.* in 1990 [18]. Although DRAMA (dipolar recoupling at the magic angle) [18; 19; 20] is not widely used today it was the basis for many robust recoupling schemes. Solid-state NMR has advanced in recent years allowing dipolar couplings between isolated spin-pairs to be determined accurately. This is generally done by so called broadband recoupling sequences which recouple over the entire chemical shift range. Additionally, there are band selective and frequency-selective recoupling methodologies that recouple only a certain (in the selective case rather narrow) part of the spectrum. While early research on dipolar recoupling methodology was targeted at improving resolution and robustness it has shifted in the last decade towards enabling a broader range of applications. One major area of research is the application of dipolar recoupling sequences to multiply labelled compounds especially peptides and proteins [21].

## 3.7. Homonuclear Multiple-Spin Systems in Solid-State NMR

Precise distance measurements by solid-state NMR using dipolar recoupling methods on homonuclear multiple-spin systems is a recent objective in the development of solid-state NMR methodology. This is founded in the sample preparation process as it is relatively difficult and expensive to obtain samples with an isolated spin-pair compared to biosynthetic methods which yield uniformly labelled samples often referred to multiple-spin spin-systems. In multiple-spin systems strong dipolar couplings, which correspond to short distances, and weak dipolar couplings corresponding to long distances are simultaneously present. If a broadband dipolar recoupling sequence, such as those developed for isolated spin-pairs, is applied then the weak dipolar couplings are attenuated by the numerous strong couplings present in the spin system. This phenomenon is known as *dipolar truncation* [22] and prohibits the precise determination of distances

greater than 3 Å.

Different approaches to overcome dipolar truncation are used (i) odd/even labelling of the samples [23] (ii) and/or the development of spectrally selective methods for recoupling [24]. The first approach led to the first protein structure determined by solid-state NMR using a proton-assisted recoupling method [23]. However, a recent study of dipolar truncation by Bayro *et al.* [22] suggests that the dipolar truncation effect is reduced if alternate labelling schemes are used. This, though, does not solve the dipolar truncation problem completely [22]. Hence, the second approach of selective recoupling is a valuable alternative.

In the last five years several research groups have been working intensely on overcoming the problem of dipolar truncation and several frequency-selective and broad-band methods were introduced. Among them are SEASHORE (shift-evolution-assisted selective dipolar recoupling) [25], TDR (truncated dipolar recoupling) [26], SDR (stochastic dipolar recoupling) [27; 28], TOFU (triple oscillating field technique) [29], FOLD (four oscillating field technique) [30] and ZQ-SEASHORE (zero-quantum SEASHORE) [31]. Some of these sequences will be discussed in more detail in Part III after the introduction of the theoretical framework (Part II).

## 3.8. Aim of my Thesis

Starting with the need for a methodology that allows the determination of structurally important distances in uniformly labelled samples, my thesis treats the dipolar truncation problem for homonuclear multiple-spin systems. The aim of my thesis is the development of a dipolar recoupling methodology that allows the determination of weaker couplings in the presence of strong dipolar couplings. Due to the distance dependence of the dipolar coupling it is possible to infer a distance from these measurements, which could then be used in applied solid-state NMR as structural constraints.

# Part II

# Theoretical Concepts in Solid-State NMR

Chapter 4

# Basic Theory in Solid-State NMR

It is unavoidable to consider the quantum mechanical description of a nuclear spin system and its spin dynamics, if one wants to understand NMR spectroscopy. Thus, the basic concepts are established in this chapter.

## 4.1. Spin State and Spin Operator

In quantum mechanics a spin state is described by a *state vector* in a complex vector space. Utilising Dirac notation such a vector, called a *ket*, is written as $|\alpha\rangle$ and assumed to contain the entire information about the spin state.

An *observable*, such as the spin angular momentum, can be represented by an operator, A, in a vector space and, generally, acts on a state ket from the left thereby generating another ket. There is a particular set of kets, the *eigenkets* of an operator, that is of importance and denoted as:

$$|\alpha_1\rangle, |\alpha_2\rangle, \ldots, |\alpha_n\rangle. \tag{4.1}$$

Their properties are defined as:

$$A|\alpha_1\rangle = \alpha_1|\alpha_1\rangle,\ A|\alpha_2\rangle = \alpha_2|\alpha_2\rangle,\ \ldots\ A|\alpha_n\rangle = \alpha_n|\alpha_n\rangle. \tag{4.2}$$

The set of numbers $\{\alpha_i\}$ is called the set of eigenvalues of the operator A and the physical state corresponding to an eigenket is called *eigenstate*. The operator which represents a given physical observable has to be Hermitian, i.e. it has to be

equal to its own adjoint, $A = A^{\dagger}$. The eigenvalues of a Hermitian operator A are real and its eigenkets correspond to different eigenvalues and are orthogonal. The normalised eigenkets of A form a *complete orthogonal set*, which is called the basis. Any arbitrary ket $|\alpha\rangle$ in the ket space can be expanded in terms of the eigenkets of A:

$$|\alpha\rangle = \sum_{\alpha_i} c_{\alpha_i} |\alpha_i\rangle, \tag{4.3}$$

where $c_{\alpha_i}$ is a probability coefficient. If $|\alpha\rangle$ is normalised, then the probability coefficients must satisfy the following condition:

$$\sum_{\alpha_i} |c_{\alpha_i}|^2 = 1 \tag{4.4}$$

The *Zeeman basis* for a single spin-1/2 system is defined as:

$$\mathbf{S}^2 = S_x^2 + S_y^2 + S_z^2 \tag{4.5}$$

$$S^2 |S,m\rangle = S(S+1)|S,m\rangle \tag{4.6}$$

and

$$S_z |S,m\rangle = m|S,m\rangle \tag{4.7}$$

where $\mathbf{S}$ is the total spin angular momentum operator, and $S_x$, $S_y$ and $S_z$ are the x-, y- and z-components of the total spin angular momentum operator. $|S,m\rangle$ are the eigenkets of $\mathbf{S}^2$ and $S_z$. For a spin-1/2 nucleus with $S = 1/2$ and $m = \pm 1/2$ the eigenkets $|S,m\rangle$ are usually expressed as:

$$|\alpha\rangle = |\frac{1}{2}, \frac{1}{2}\rangle \tag{4.8}$$

$$|\beta\rangle = |\frac{1}{2}, -\frac{1}{2}\rangle \tag{4.9}$$

where $|\alpha\rangle$ and $|\beta\rangle$ form a complete orthogonal set. Any state ket $|\Psi\rangle$ can be expressed as linear combination of $|\alpha\rangle$ and $|\beta\rangle$:

$$|\Psi\rangle = c_\alpha |\alpha\rangle + c_\beta |\beta\rangle \tag{4.10}$$

where $c_\alpha$ and $c_\beta$ are complex coefficients that have to satisfy $|c_\alpha|^2 + |c_\beta|^2 = 1$.

## 4.2. Spin Hamiltonian Hypothesis

The quantum state of a physical system at a time point $t$ is defined by its state function $|\Psi_{full}(t)\rangle$ and its time evolution is determined by the *time-dependent Schrödinger equation*:

$$\frac{d}{dt}|\Psi_{full}(t)\rangle = -iH_{full}(t)|\Psi_{full}(t)\rangle. \tag{4.11}$$

$H_{full}(t)$ is a Hermitian operator that is associated with the total energy of the system given in angular frequency units and is called the *Hamiltonian*. The time-dependent Schrödinger equation given in Equation 4.11 contains information about all electrons and nuclei in a system and is, thus, rather complex. Since electron dynamics occur on a much faster time scale than nuclear spin dynamics it is feasible to simplify the Schrödinger equation for NMR spectroscopy using a state function, $|\Psi_{spin}(t)\rangle$, for the nuclear spin only:

$$\frac{d}{dt}|\Psi_{spin}(t)\rangle \backsimeq -iH_{spin}(t)|\Psi_{spin}(t)\rangle, \tag{4.12}$$

where $H_{spin}$ is the nuclear spin Hamiltonian. This description is called the *spin Hamiltonian hypothesis* [32] and $H_{spin}$ contains only terms that depend on the directions of the nuclear spin polarisations, assuming that only the average over the electronic interactions is observed. In the following the operator $H$ implies the nuclear spin Hamiltonian and the quantum states $|\Psi(t)\rangle$ imply nuclear spin states.

The nuclear spin Hamiltonian can be described by two terms, the *electric spin Hamiltonian*, which describes changes in the nuclear electric energy upon rotation of the nucleus, and a *magnetic spin Hamiltonian*, which describes changes in the nuclear magnetic energy upon rotation of the nucleus. Consequently, the spin Hamiltonian for a nucleus $S_j$ is expressed as:

$$H_j = H_j^{elec} + H_j^{mag}. \tag{4.13}$$

For nuclei with a spin quantum number of $S = 1/2$ the electric spin Hamiltonian vanishes as its charge distribution is spherical symmetric. This is, however, not the case for nuclei with a spin quantum number $S > 1/2$, in which the charge distribution is not spherical symmetric and thus the electric spin Hamiltonian does not vanish. Throughout this thesis only nuclei with a spin quantum number

of $S = 1/2$ are considered.

## 4.3. Euler Angles and Rotation Operators

A general rotation can be described by a rotation operator $R[\Omega]$ with Euler angles $\Omega = \{\alpha, \beta, \gamma\}$ [33]. Such a rotation $R[\Omega]$ consists of three consecutive rotations: (i) by $\gamma$ around the z-axis, (ii) by $\beta$ around the y-axis and (iii) by $\alpha$ around the z-axis. The mathematical representation of the Euler angle transformation is, thus:

$$\begin{aligned} R[\alpha,\beta,\gamma] &= R_z[\alpha] R_y[\beta] R_z[\gamma] \\ &= e^{-i\alpha S_z} e^{-i\beta S_y} e^{-i\gamma S_z} \end{aligned} \tag{4.14}$$

and the rotations are performed sequentially from the right to the left.

## 4.4. Spin Hamiltonian in Solids

The nuclear spin Hamiltonian, $H$, may be expressed by the sum over all spin interactions, $\Lambda$, in a system:

$$H = \sum_{\Lambda} H_{\Lambda}. \tag{4.15}$$

## 4.5. Tensors

Tensors are geometric entities that were introduced into mathematics and physics to extend the notion of scalars, vectors, and matrices to higher orders. The rank of a tensor is the dimensionality of the array needed to represent it. Consequently, a scalar is a tensor of rank-0 and used to describe orientation independent physical properties such as the electrical charge. Following this argument it can be deduced that a vector is a first rank (rank-1) tensor and a matrix a second rank (rank-2) tensor. For the purpose of this thesis only tensors up to rank-2 are discussed.

### 4.5.1 Cartesian Tensors

Tensors play an important role in the description of spin interactions, $\Lambda$, since the spin interaction Hamiltonian, $H^{\Lambda}$, in the Cartesian frame is expressed as:

$$\begin{aligned} H^{\Lambda} &= C^{\Lambda}\,\mathbf{X}\,\mathbb{A}^{\Lambda}\,\mathbf{Y} \\ &= C^{\Lambda}\left(X_x^{\Lambda}, X_y^{\Lambda}, X_z^{\Lambda}\right)\begin{pmatrix} A_{xx}^{\Lambda} & A_{xy}^{\Lambda} & A_{xz}^{\Lambda} \\ A_{yx}^{\Lambda} & A_{yy}^{\Lambda} & A_{yz}^{\Lambda} \\ A_{zx}^{\Lambda} & A_{zy}^{\Lambda} & A_{zz}^{\Lambda} \end{pmatrix}\begin{pmatrix} Y_x^{\Lambda} \\ Y_y^{\Lambda} \\ Y_z^{\Lambda} \end{pmatrix} \end{aligned} \tag{4.16}$$

where $\mathbb{A}^{\Lambda}$ is a second rank Cartesian tensor, $C^{\Lambda}$ is a constant specific to a given spin interaction, and $\mathbf{X}$ and $\mathbf{Y}$ are vector operators representing the interacting physical quantities. $\mathbf{X}$ and $\mathbf{Y}$ can both be nuclear spins or one of them is a nuclear spin while the other one is an external magnetic field.

### 4.5.2 Irreducible Spherical Tensors and Wigner Matrices

Cartesian tensors have the advantage that they are easy to visualise, however, they are not favourable from a mathematical point of view, as they are reducible [33]. Thus, any second rank Cartesian tensor $\mathbb{A}^{\Lambda}$ can be decomposed into three *irreducible spherical tensors*: a scalar rank-0 spherical tensor, $\mathcal{A}_0^{\Lambda}$, which is proportional to the trace of $\mathbb{A}^{\Lambda}$; an asymmetric rank-1 spherical tensor, $\mathcal{A}_1^{\Lambda}$; and a symmetric rank-2 spherical tensor, $\mathcal{A}_2^{\Lambda}$. Each irreducible spherical tensor, $\mathcal{A}_{lm}^{\Lambda}$, with ranks $l = 0, 1, 2, \ldots$ posses $(2l+1)$ components, $m = -l, -l+1, \ldots, l$. If a rotation operator $R[\Omega]$ is applied to an irreducible spherical tensor, $\mathcal{A}_{lm}^{\Lambda}$, with a given rank $l$ and components $m$ then the rotation transforms $\mathcal{A}_{lm}^{\Lambda}$ into another object, $\mathcal{A}_{lm'}^{\Lambda}$, of the same rank [7; 33]:

$$R[\Omega]\,\mathcal{A}_{lm}^{\Lambda}R^{-1}[\Omega] = \sum_{m'=-l}^{+l} D_{mm'}^{l}[\Omega]\,\mathcal{A}_{lm'}^{\Lambda}, \tag{4.17}$$

where $D_{mm'}^{l}[\Omega]$ is know as the *Wigner matrix*. The Wigner matrix is expressed as:

$$\begin{aligned} D_{mm'}^{l}[\Omega] &= \langle lm'|e^{-i\alpha S_z}e^{-i\beta S_y}e^{-i\gamma S_z}|lm\rangle \\ &= e^{-i\alpha m'}\langle lm'|e^{-i\beta S_y}|lm\rangle e^{-i\gamma m} \\ &= e^{-i\alpha m'}\,d_{m'm}^{l}[\beta]\,e^{-i\gamma m} \end{aligned} \tag{4.18}$$

where the term $d^l_{m'm}[\beta]$ is called the *reduced Wigner matrix element*. The size of the Wigner matrix depends on the $l$ values with $(2l+1)$. The reduced Wigner matrix elements for rank-1 and rank-2 are given in Tables 4.1 and 4.2.

Table 4.1: Reduced rank-1 Wigner matrix elements

| $m'$ \ $m$ | 1 | 0 | −1 |
|---|---|---|---|
| 1 | $\frac{1+\cos\beta}{2}$ | $-\frac{\sin\beta}{\sqrt{2}}$ | $\frac{1-\cos\beta}{2}$ |
| 0 | $\frac{\sin\beta}{\sqrt{2}}$ | $\cos\beta$ | $-\frac{\sin\beta}{\sqrt{2}}$ |
| 1 | $\frac{1-\cos\beta}{2}$ | $\frac{\sin\beta}{\sqrt{2}}$ | $\frac{1+\cos\beta}{2}$ |

The exact form of an irreducible spherical tensor depends of the chosen coordinate system or *reference frame*. Two reference frames $F$ and $F'$ are related to each other by a rotation that is specified by a set of Euler angles $\Omega_{FF'} = \{\alpha_{FF'}, \beta_{FF'}, \gamma_{FF'}\}$. Irreducible spherical tensors of rank $l$ with $(2l+1)$ components are defined to transform under rotation between the coordinate systems as follows:

$$\left[\mathcal{A}^{\Lambda}_{lm}\right]^{F'} = \sum_{m'=-l}^{l} \left[\mathcal{A}^{\Lambda}_{lm'}\right]^{F} D^{l}_{m'm}[\Omega_{FF'}]. \tag{4.19}$$

It is now possible to express the nuclear spin Hamiltonian of a spin interaction, $\Lambda$, as scalar product of two irreducible spherical tensors [7]:

$$H_{\Lambda} = C^{\Lambda} \sum_{l} \sum_{m=-l}^{l} (-1)^m \left[\mathcal{A}^{\lambda}_{lm}\right]^{F} \left[\mathcal{T}^{\lambda}_{l-m}\right]^{F}, \tag{4.20}$$

where $\mathcal{A}^{\lambda}_{l}$ is known as *spatial tensor*. Depending on the described interaction $\mathcal{T}^{\lambda}_{l}$ is called *spin tensor* or *spin-field tensor*. The exact form of the tensor elements depends on the chosen reference frame.

The spin-field tensor is composed of a spin part, that can be rotated by external rf-fields, and a field part, that is usually a static magnetic field and thus not subject to rotations. This allows the substitution of components $\mathcal{T}^{\Lambda}_{lm}$ of the spin-

Table 4.2: Reduced rank-2 Wigner matrix elements

| $m'$ \ $m$ | 2 | 1 | 0 | −1 | −2 |
|---|---|---|---|---|---|
| 2 | $\frac{(1+\cos\beta)^2}{4}$ | $-\frac{\sin\beta(1+\cos\beta)}{2}$ | $\frac{1}{2}\sqrt{\frac{3}{2}}\sin^2\beta$ | $-\frac{\sin\beta(1-\cos\beta)}{2}$ | $\frac{(1-\cos\beta)^2}{4}$ |
| 1 | $\frac{\sin\beta(1+\cos\beta)}{2}$ | $\frac{2\cos^2\beta+(\cos\beta)-1}{2}$ | $-\sqrt{\frac{3}{2}}\sin\beta\cos\beta$ | $-\frac{2\cos^2\beta-(\cos\beta)-1}{2}$ | $-\frac{\sin\beta(1-\cos\beta)}{2}$ |
| 0 | $\frac{1}{2}\sqrt{\frac{3}{2}}\sin^2\beta$ | $\sqrt{\frac{3}{2}}\sin\beta\cos\beta$ | $\frac{3(\cos^2\beta)-1}{2}$ | $-\sqrt{\frac{3}{2}}\sin\beta\cos\beta$ | $\frac{1}{2}\sqrt{\frac{3}{2}}\sin^2\beta$ |
| −1 | $\frac{\sin\beta(1-\cos\beta)}{2}$ | $-\frac{2\cos^2\beta-(\cos\beta)-1}{2}$ | $\sqrt{\frac{3}{2}}\sin\beta\cos\beta$ | $\frac{2\cos^2\beta+(\cos\beta)-1}{2}$ | $-\frac{\sin\beta(1+\cos\beta)}{2}$ |
| −2 | $\frac{(1-\cos\beta)^2}{4}$ | $-\frac{\sin\beta(1-\cos\beta)}{2}$ | $\frac{1}{2}\sqrt{\frac{3}{2}}\sin^2\beta$ | $-\frac{\sin\beta(1+\cos\beta)}{2}$ | $\frac{(1+\cos\beta)^2}{4}$ |

or spin-field tensors in the internal spin Hamiltonian into components $T^{\Lambda}_{\lambda\mu}$ of pure irreducible spherical spin tensors (Appendix A), where ranks $l$ and $\lambda$ can be different. Furthermore, a spatial tensors $A^{\Lambda}_{l}$ can be defined, which relates to spatial tensors $\mathcal{A}^{\Lambda}_{l}$ by numerical factors. Space and spin-parts for some spin interactions are presented in Table 4.3. The relationship between components $\mathcal{A}^{\Lambda}_{l}$ and $A^{\Lambda}_{l}$ as well as the relationship between components $\mathcal{T}^{\Lambda}_{lm}$ and $T^{\Lambda}_{\lambda\mu}$ is given in Table 4.4.

## 4.6. Reference Frames in Solid-State NMR

Handling spin interactions in rotating solids involves a set of reference frames and transformations between them, which are introduced in the following.

The *principal axis frame* denoted as PAS or $P^{\Lambda}$ is unique to a spin interaction $\Lambda$ and is defined as the reference frame in which the tensor describing the spin interaction is diagonal.

The *molecular frame*, $M$, is a common frame for all spin interactions in a molecule, thus, it is arbitrarily fixed within the molecular structure. It is related to the principal axis frame, $P^{\Lambda}$, by a set of Euler angles, $\Omega^{\Lambda}_{PM} = \{\alpha^{\Lambda}_{PM}, \beta^{\Lambda}_{PM}, \gamma^{\Lambda}_{PM}\}$, that define the relative orientation of a spin interaction to the molecular structure.

The z-axis of the *rotor frame*, R, is oriented along the spinning axis of the rotor and the relative orientation between the rotor frame, R, and the molecular frame, $M$, is characterised by a set of Euler angles, $\Omega^{\Lambda}_{MR} = \{\alpha^{\Lambda}_{MR}, \beta^{\Lambda}_{MR}, \gamma^{\Lambda}_{MR}\}$. In a powder sample many sets of randomly distributed Euler angles, $\Omega^{\Lambda}_{MR}$, are simultaneously present.

In the *laboratory frame*, $L$, the z-axis is aligned along the external magnetic field and the set of Euler angles, $\Omega^{\Lambda}_{RL} = \{\alpha^{\Lambda}_{RL}, \beta^{\Lambda}_{RL}, \gamma^{\Lambda}_{RL}\}$, relates it to the rotor frame, R.

## 4.7. High-Field Approximation

The nuclear spin Hamiltonian can be divided into a part, $H^{RF}$, representing interactions with the transverse oscillating rf-field and an interaction part, $H^{IA}$,

Table 4.3: Space and spin parts for a list of spin interaction, including relevant tensor components $A_l^\Lambda$ for different components in the high-field approximation.

| | | space part | | | | |
|---|---|---|---|---|---|---|
| interaction | F | $[A_{00}^\Lambda]^F$ | $[A_{20}^\Lambda]^F$ | $[A_{2\pm1}^\Lambda]^F$ | $[A_{2\pm2}^\Lambda]^F$ | spin part |
| Zeeman | $L$ | $\omega_0$ | – | – | – | $T_{10}^j$ |
| isoCS | $L$ | $\omega_0\delta_{iso}^j$ | – | – | – | $T_{10}^j$ |
| Zeeman + isoCS in rotating frame | $L$ | $\Omega_j$ | – | – | – | $T_{10}^j$ |
| CSA | $P$ | – | $\omega_0\left(\delta_{zz}^P-\delta_{iso}^j\right)$ | 0 | $-\frac{\eta}{\sqrt{6}}[A_{20}]^P$ | $T_{10}^j$ |
| homonuclear dipolar coupling | $P$ | – | $\sqrt{6}b_{jk}$ | 0 | 0 | $T_{20}^{jk}$ |
| homonuclear J-coupling | $L$ | $-\sqrt{3}\,2\pi J$ | – | – | – | $T_{00}^{jk}$ |
| heteronuclear dipolar coupling | $P$ | – | $2b_{jk}$ | 0 | 0 | $T_{10}^I T_{10}^S$ |
| heteronuclear J-coupling | $L$ | $2\pi J$ | – | – | – | $T_{10}^I T_{10}^S$ |

Table 4.4: Relationships between tensor components. The spatial tensor components $\mathcal{A}_l^\Lambda$ are related to the spatial tensor components $A_l^\Lambda$, while the spin-field tensor components $\mathcal{T}_{lm}^\Lambda$ are related to spin tensor components $T_{\lambda\mu}^\Lambda$.

| interaction | $C^\Lambda$ | space part | spin or spin-field part |
|---|---|---|---|
| Zeeman | $-\gamma_S$ | $[\mathcal{A}_{00}^\Lambda]^L = -\frac{\sqrt{3}}{\omega_0}[A_{00}^\Lambda]^L$ | $[\mathcal{T}_{00}^\Lambda]^L = -\frac{1}{\sqrt{3}}B_0 T_{10}^j$ |
| isoCS | $-\gamma_S$ | $[\mathcal{A}_{00}^\Lambda]^L = -\frac{\sqrt{3}}{\omega_0}[A_{00}^\Lambda]^L$ | $[\mathcal{T}_{00}^\Lambda]^L = -\frac{1}{\sqrt{3}}B_0 T_{10}^j$ |
| CSA | $-\gamma_S$ | $[\mathcal{A}_{2m}^\Lambda]^P = \frac{\sqrt{3}}{\sqrt{2}\omega_0}[A_{2m}^\Lambda]^p$ | $[\mathcal{T}_{20}^\Lambda]^L = \sqrt{\frac{3}{2}}B_0 T_{10}^j$ |
| homonuclear dipolar coupling | 1 | $[\mathcal{A}_{2m}^\Lambda]^P = [A_{2m}^\Lambda]^P$ | $[\mathcal{T}_{20}^\Lambda]^L = T_{20}^{jk}$ |
| homonuclear J-coupling | $2\pi$ | $[\mathcal{A}_{00}^\Lambda]^L = \frac{1}{2\pi}[A_{00}^\Lambda]^L$ | $[\mathcal{T}_{00}^\Lambda]^L = T_{00}^{jk}$ |
| heteronuclear dipolar coupling | 1 | $[\mathcal{A}_{2m}^\Lambda]^P = \sqrt{\frac{3}{2}}[A_{2m}^\Lambda]^p$ | $[\mathcal{T}_{20}^\Lambda]^L = \frac{2T_{10}^I T_{10}^S + T_{1-1}^I T_{11}^S + T_{11}^I T_{1-1}^S}{\sqrt{6}}$ |
| heteronuclear J-coupling | $2\pi$ | $[\mathcal{A}_{00}^\Lambda]^L = -\frac{\sqrt{3}}{2\pi}[A_{00}^\Lambda]^L$ | $[\mathcal{T}_{00}^\Lambda]^L = -\frac{2T_{10}^I T_{10}^S - T_{1-1}^I T_{11}^S - T_{11}^I T_{1-1}^S}{\sqrt{3}}$ |

containing spin interactions with the static magnetic field in form of the Zeeman Hamiltonian $H_j^Z$ as well as internal spin interactions. The Hamiltonian may be written as:

$$H = H^{RF} + H^{IA} \tag{4.21}$$

In a high magnetic field the interaction term is dominated by the Zeeman Hamiltonian, since it is several orders of magnitude larger than all other spin interactions. Consequently, it is possible to treat the remaining spin interactions as a perturbation of the Zeeman term. In practice this involves neglecting terms which do not commute with the Zeeman Hamiltonian; for a tensor $\mathbb{A}$ this involves considering only the component in the z-direction, i.e. $A_{zz}$. The terms commuting with the Zeeman Hamiltonian are known as *secular terms* and correspond to the diagonal terms in the matrix representation of the interaction. Those terms which do not commute with the Zeeman Hamiltonian are called *non secular terms* and correspond to the off-diagonal elements in the matrix representation of the interaction. The neglecting of non-secular terms is referred to as *secular or high-field approximation*. In context of spherical tensors this matches the selection of spin operators of the form $T^{\Lambda}_{\lambda 0}$.

## 4.8. External Spin Interactions

External spin interactions are spin-field interactions which comprise spin interactions with the static external magnetic field, $B_0$, and transverse rf-fields. Thus the external spin Hamiltonian, $H^{ext}$, can be written as:

$$H^{ext} = H_j^Z + H_j^{RF} \tag{4.22}$$

where $H_j^Z$ is the Zeeman Hamiltonian which represents the spin interactions with $B_0$. $H_j^{RF}$ denotes the spin interactions with a transverse oscillating rf-field, $B_{rf}$.

### 4.8.1 Zeeman Interaction

The *Zeeman interaction* of a spin, $S_j$, depends on the external magnetic field, $B_0$, as follows:

$$\begin{aligned} H_j^Z &= -\boldsymbol{\mu}_{S_j}\mathbf{B_0} \\ &= -\gamma_{S_j} S_{jz} B_0 \\ &= \omega_0 S_{jz} \end{aligned} \tag{4.23}$$

where $\mu_{S_j}$ is the magnetic moment of $S_j$, $\gamma_{S_j}$ is the gyromagnetic ratio, $S_{jz}$ is the z-component of the spin operator and $\omega_0 = -\gamma_{S_j} B_0$ is the Larmor frequency of $S_j$. The Zeeman Hamiltonian may be written in terms of irreducible spherical tensor operators:

$$H_j^Z = \left[A_{00}^Z\right] T_{10}^j = \omega_0 T_{10}^j \tag{4.24}$$

### 4.8.2 Radio-Frequency Field Interaction

Also contained within the external Hamiltonian are interactions with the transverse rf-irradiation. The oscillating rf-field during a rf-pulse is given by:

$$\mathbf{B}_{rf} = B_{rf} \cos\left[\omega_{ref}(t) + \phi_p\right] \mathbf{e}_x \tag{4.25}$$

where $B_{rf}$ is the strength of the rf-field, $\omega_{ref}$ is the spectrometer reference frequency, and $\phi_p$ is the rf-phase. It is possible to decompose the rf-field into two counter-rotating parts, and only the part that rotates in the same sense as the spins induces transitions of the spin states. Consequently, the rf-Hamiltonian of $S_j$ with the resonant part of the rf-field may be expressed as:

$$H_j^{RF}(t) = -\frac{1}{2}\gamma_{S_j} B_{rf} \left(S_{jx}\cos\left[\omega_{ref}(t) + \phi_p\right] + S_{jy}\sin\left[\omega_{ref}(t) + \phi_p\right]\right). \tag{4.26}$$

To gain a time-independent expression of $H_j^{RF}(t)$ it is possible to transform the Hamiltonian into the *rotating frame*, whose z-axis corresponds to the z-axis of the laboratory frame. However, the x- and y-axis rotate in the same direction and with the same frequency as the resonant component of $B_{rf}$. Thus, the rf-Hamiltonian in the rotating frame is given by:

$$H_j^{RF} = \omega_{nut}^j \left(S_{jx}\cos\left[\phi_p\right] + S_{jy}\sin\left[\phi_p\right]\right) \tag{4.27}$$

where the nutation frequency, $\omega_{nut}$, of the rf-field has the form:

$$\omega_{nut}^{j} = \frac{1}{2}|\gamma_{S_j} B_{rf}|. \tag{4.28}$$

The *flip-angle*, $\beta$, of a rf-pulse is defined as:

$$\beta = \omega_{nut}\tau_p \tag{4.29}$$

where $\tau_p$ is the duration of the pulse. Strong, short pulses excite a wide frequency range, while weak pulses of a long duration excite a more narrow frequency range and are referred to as frequency-selective pulses. The frequency range over which a pulse acts — its excitation profile — depends on the Fourier transform of the excitation, thus, a short rectangular pulse which accomplishes the same rotation as a long shaped pulse excites a much larger frequency range.

## 4.9. Internal Spin Interactions

The internal spin Hamiltonian, $H^{int}$, for two spins $S_j$ and $S_k$, which both have a spin quantum number $S = 1/2$, is defined as:

$$H_{jk}^{int} = H_j^{CS} + H_k^{CS} + H_{jk}^{DD} + H_{jk}^{J}, \tag{4.30}$$

where $H_j^{CS}$ and $H_k^{CS}$ represent the chemical shift interactions of spins $S_j$ and $S_k$, respectively. The dipolar coupling interaction is represented by $H_{jk}^{DD}$ and the J-couplings by $H_{jk}^{J}$.

### 4.9.1 Chemical Shift

The interaction of a spin, $S_j$, with a local magnetic field, $\mathbf{B}_{loc}^{j} = \mathbf{B}_0 + \mathbf{B}_{ind}^{j}$ is known as chemical shift interaction and depends on the static magnetic field, $\mathbf{B}_0$, as well as an induced magnetic field, $\mathbf{B}_{ind}^{j}$. $\mathbf{B}_{ind}^{j}$ is generated by electrical currents, which the static magnetic field induces in the local electronic environment of $S_j$. Thus, different molecular sites experience different local magnetic fields depending on their electronic environment.

The chemical shift interaction for a given spin can be expressed as:

$$\begin{aligned} H_j^{CS} &= -\gamma_j \mathbf{S}_j \mathbf{B}_{loc}^j \\ &= -\gamma_j \mathbf{S}_j \delta^j \mathbf{B}_0 \end{aligned} \tag{4.31}$$

where $\delta_j$ is the chemical shift tensor following the deshielding convention and as a Cartesian tensor of rank-2 ($3 \times 3$ matrix). The induced magnetic field in the matrix form can, thus, be written as:

$$\begin{aligned} \begin{pmatrix} B_{ind}^{jx} \\ B_{ind}^{jy} \\ B_{ind}^{jy} \end{pmatrix} &= \begin{pmatrix} \delta_{xx}^j & \delta_{yx}^j & \delta_{xz}^j \\ \delta_{xy}^j & \delta_{yy}^j & \delta_{yz}^j \\ \delta_{xz}^j & \delta_{yz}^j & \delta_{zz}^j \end{pmatrix} \begin{pmatrix} 0 \\ 0 \\ B_0 \end{pmatrix} \\ &= \begin{pmatrix} \delta_{xz}^j B_0 \\ \delta_{yz}^j B_0 \\ \delta_{zz}^j B_0 \end{pmatrix} \end{aligned} \tag{4.32}$$

From this it is apparent, that the induced magnetic field has components not only along the z-direction, but also along the x- and y-direction of the laboratory frame. However, components $\delta_{xz}^j$ and $\delta_{xy}^j$ along the x- and y-direction of the laboratory frame are no longer retained under the highfield approximation.

It is convenient to decompose the chemical shift tensor into three irreducible tensors:

$$\delta^j = \delta_{iso}^j + \delta_{asymm}^j + \delta_{aniso}^j, \tag{4.33}$$

where $\delta_{iso}^j$ is a rank-0 tensor known as the *isotropic chemical shift*, which is given by the trace of the chemical shift tensor:

$$\begin{aligned} \delta_{iso}^j &= \frac{1}{3}\mathrm{Tr}\left(\delta^j\right) \\ &= \frac{1}{3}\left(\delta_{xx}^j + \delta_{yy}^j + \delta_{zz}^j\right) \end{aligned} \tag{4.34}$$

The *asymmetric chemical shift* is represented by a rank-1 part, which is mostly ignored under the high-field approximation. Its secular term is proportional to $T_{10}^{jk}$ and has recently been observed by Harris *et al.* [34]. The *chemical shift anisotropy* (CSA) is a tensor of rank-2, the three diagonal elements, $\delta_{xx}^p$, $\delta_{yy}^p$ and $\delta_{zz}^p$ are called the *principal values* of the tensor and are labelled:

$$\left|\delta_{zz}^P - \delta_{iso}^j\right| \geq \left|\delta_{xx}^P - \delta_{iso}^j\right| \geq \left|\delta_{yy}^P - \delta_{iso}^j\right|. \tag{4.35}$$

The CSA can be expressed in terms of the anisotropic chemical shift frequency:

$$\omega_{aniso} = \omega_0 \left( \delta^P_{zz} - \delta^j_{iso} \right) \tag{4.36}$$

and the *asymmetry parameter*, $\eta$:

$$\eta = \frac{\delta^P_{yy} - \delta^P_{xx}}{\delta^P_{zz} - \delta^j_{iso}}. \tag{4.37}$$

The chemical shift Hamiltonian under the high-field approximation expressed as:

$$\begin{aligned} H^{CS}_j &= \omega_0 \, \delta^j_{iso} \, S_{jz} + \left[ A^{CS}_{20} \right]^L S_{jz} \\ &= \left[ A^{CS}_{00} \right]^L T^j_{10} + \left[ A^{CS}_{20} \right]^L T^j_{10} \end{aligned} \tag{4.38}$$

with:

$$\left[ A^{CS}_{20} \right]^L = \sum_{m=-2}^{2} \sum_{m'=-2}^{2} \left[ A^{CS}_{2m'} \right]^P D^2_{m'm} \left[ \Omega^{CS}_{PR}(t) \right] D^2_{m0} \left[ \Omega^{CS}_{RL} \right]. \tag{4.39}$$

It is common to combine the Zeeman Hamiltonian for spin $S_j$ in the rotating frame with the chemical shift Hamiltonian to:

$$\begin{aligned} H^{Z,CS}_j &= \Omega j \, S_{jz} + \left[ A^{CS}_{20} \right]^L S_{jz} \\ &= \left[ A^{Z,CS}_{00} \right]^L T^j_{10} + \left[ A^{CS}_{20} \right]^L T^j_{10} \end{aligned} \tag{4.40}$$

where the chemical shift frequency is defined as:

$$\Omega_j = \omega_0 \left( 1 + \delta^j_{iso} \right) - \omega_{ref}. \tag{4.41}$$

### 4.9.2 Direct Dipolar Coupling

The direct dipolar coupling or through space dipole-dipole coupling is, as the name indicates, a through space interaction between two nuclear spins based on the spins perception of each others magnetic fields. In the homonuclear case the dipolar coupling between two spins $S_j$ and $S_k$ can be described by the traceless symmetric Cartesian tensor, $\mathbb{D}$ [7]. Thus, the Hamiltonian is expressed as:

$$H^{DD}_{jk} = \mathbf{S}_j \, \mathbb{D} \, \mathbf{S}_k \tag{4.42}$$

This is consistent with the interaction between two magnetic dipols:

$$H_{jk}^{DD} = b_{jk}\left(3\left(\mathbf{S}_j\mathbf{e}_{jk}\right)\left(\mathbf{S}_k\mathbf{e}_{jk}\right) - \mathbf{S}_j\mathbf{S}_k\right) \tag{4.43}$$

where the unit vector, $\mathbf{e}_{jk}$, is oriented parallel to the internuclear axis between spins $S_j$ and $S_k$. The dipolar coupling constant, $b_{jk}$, is defined as:

$$b_{jk} = -\frac{\mu_0\gamma_j\gamma_k\hbar}{4\pi r_{jk}^3} \tag{4.44}$$

where $\gamma_j$ and $\gamma_k$ are the gyromagnetic ratios for spins $j$ and $k$, which are equivalent in the homonuclear case. The internuclear distance is given by $r_{jk}$. Unlike the dipolar Hamiltonian, the dipolar coupling constant is orientation independent. In the high-field approximation the homonuclear dipolar Hamiltonian may be written as:

$$\begin{aligned} H_{jk}^{DD} &= b_{jk}\frac{1}{2}\left(3\cos^2\left[\theta_{jk}\right]-1\right)\left(3S_{jz}S_{kz} - \mathbf{S}_j\mathbf{S}_k\right) \\ &= b_{jk}\frac{1}{2}\left(3\cos^2\left[\theta_{jk}\right]-1\right)\left(2S_{jz}S_{kz} - \frac{1}{2}\left(S_j^+S_k^- + S_j^-S_k^+\right)\right). \end{aligned} \tag{4.45}$$

The term $2S_{jz}S_{kz} - \frac{1}{2}\left(S_j^+S_k^- + S_j^-S_k^+\right)$ is called *"flip-flop-term"* and plays a crucial role in the dipolar recoupling of multiple-spin systems. Utilising spherical tensors the homonuclear dipolar coupling Hamiltonian in the high-field approximation is defined:

$$H_{jk}^{DD} = \left[A_{20}^{DD}\right]^L T_{20}^{jk} \tag{4.46}$$

where $\left[A_{20}^{DD}\right]^L$ is the orientation dependent spatial part. For the heteronuclear case under the same conditions the dipolar coupling Hamiltonian between two spins $I_j$ and $S_k$ is given:

$$\begin{aligned} H_{IS}^{DD} &= b_{jk}\left(3\cos^2\left[\Theta_{jk}\right]-1\right)I_{jz}S_{kz} \\ &= \left[A_{20}^{DD_{IS}}\right]^L T_{10}^{I_j}T_{10}^{S_k} \end{aligned} \tag{4.47}$$

### 4.9.3 J-Coupling

The J-coupling, also known as indirect dipolar coupling, is an internuclear coupling between two nuclear spins and is mediated by bonding electrons. Thus, its properties and magnitude depend strongly on the nature of the chemical bond

and the involved orbitals. The J-coupling Hamiltonian between two spins $S_j$ and $S_k$ is expressed as:

$$H_{jk}^{J} = \mathbf{S}_j \mathbb{J} \mathbf{S}_k \tag{4.48}$$

with the scalar coupling tensor, $\mathbb{J}$, and the spin operators $\mathbf{S}_j$ and $\mathbf{S}_k$. The J-coupling interaction can be decomposed into irreducible spherical tensors of rank-0, rank-1 and rank-2 and is written as:

$$\mathbb{J} = J^{(0)} + J^{(1)} + J^{(2)}. \tag{4.49}$$

The rank-0 part, $J^{(0)}$, represents the isotropic interaction:

$$\begin{aligned} H_{jk}^{J,iso} &= 2\pi J_{jk} \mathbf{S}_j \cdot \mathbf{S}_k \\ &= 2\pi J_{jk} \left( S_{jz} S_{kz} + \frac{1}{2} \left( S_j^+ S_k^- + S_j^- S_k^+ \right) \right) \\ &= \left[ A_{00}^{J_{jk}} \right]^L T_{00}^{jk} \end{aligned} \tag{4.50}$$

where $J_{jk}$ is the J-coupling constant in Hertz. It is this interaction which determines the multiplet pattern observed in liquid-state NMR. In the solid-state this contribution is still present, however, it is generally masked by broad spectral lines. The rank-1 part, $J^{(1)}$, is the asymmetric J-coupling and often ignored under the high-field approximation. However, it has a secular term which is proportional to $T_{10}^{jk}$ and has been measured in recent studies [34]. The anisotropic J-coupling (rank-2 part), can be described by an anisotropic J-coupling constant and an asymmetry parameter. The isotropic and the anisotropic J-coupling constants are typically in the same order of magnitude. However, the anisotropic J-coupling has the same transformation properties as the through space dipolar coupling, hence, they are difficult to disentangle. In tensorial form the homonuclear J-coupling can be expressed as:

$$H_{jk} = 2\pi J_{jk} T_{00}^{jk} + J_{jk}^{aniso} T_{20}^{jk}. \tag{4.51}$$

Chapter 5

# Theoretical Tools in Solid-State NMR

## 5.1. Time Evolution Operator

In quantum mechanics the evolution of a state ket $|\Psi,t\rangle$ is described by a time evolution operator, $U(t,t_0)$, called the propagator. This makes it possible to derive the state ket at a future time point, $t$, from the state ket at an earlier time point $t_0$ by employing the propagator:

$$|\Psi,t\rangle = U(t,t_0)|\Psi,t_0\rangle\,, \tag{5.1}$$

where the propagator is unitary:

$$U^{\dagger}(t,t_0)U(t,t_0) = 1. \tag{5.2}$$

$t_0$ is the starting point and $t$ is the end point of the observed evolution period. The propagator $U(t,t_0)$ over this period is the solution of the time-dependent Schrödinger equation:

$$\frac{d}{dt}U(t,t_0) = -iHU(t,t_0). \tag{5.3}$$

The evolution of any ket $|\Psi,t\rangle$ is given by:

$$\frac{d}{dt}|\Psi,t\rangle = -iH|\Psi,t\rangle\,. \tag{5.4}$$

The solution to the Schrödinger equation depends on the particular Hamiltonian under investigation. The simplest case is when the Hamiltonian, $H$, is time

independent, in which case the solutionof Equation 5.3 becomes:

$$U(t,t_0) = e^{-iH(t-t_0)}. \tag{5.5}$$

If the Hamiltonian is time dependent, but posses the property $\left[H\left(t'\right),H\left(t''\right)\right]=0$, Equation 5.3 may be solved as follows:

$$U(t,t_0) = e^{-i\int_{t_0}^{t} dt' H(t')}. \tag{5.6}$$

For a piecewise time-independent Hamiltonian with $\left[H\left(t'\right),H\left(t''\right)\right]\neq 0$ the propagator may be expressed as:

$$U(t,t_0) = e^{-iH_n\tau_n}\ldots e^{-iH_2\tau_2}e^{-iH_1\tau_1}. \tag{5.7}$$

Other cases require the use of average Hamiltonian theory [35; 36] (Section 5.3.), Floquet theory or numerical simulations to solve the Schrödinger equation.

## 5.2. Density Operator

A macroscopic sample consists of a huge number of interacting spins and the *density operator* is used to describe the quantum state of this spin ensemble, since it is not feasible to treat all spin systems individually. The density operator is defined as:

$$\begin{aligned}\rho(t) &= \overline{|\Psi_k(t)\rangle\langle\Psi_k(t)|} \\ &= \sum_k p_k |\Psi_k(t)\rangle\langle\Psi_k(t)|\end{aligned} \tag{5.8}$$

where $p_k$ is the probability of an individual spin system to be part of the spin state $|\Psi_k(t)\rangle$. The overbar indicates an average over an ensemble of N spins.

The expectation value of an operator $Q$ over the ensemble is given:

$$\begin{aligned}\left\langle\overline{Q}\right\rangle &= \{\rho(t)\,Q\} \\ &= \sum_k p_k \langle\Psi_k(t)|Q|\Psi_k(t)\rangle\end{aligned} \tag{5.9}$$

In the Zeeman basis the density operator can be written as:

$$\rho(t) = \sum_{r,s} \rho_{rs}(t) |r\rangle \langle s| . \tag{5.10}$$

The diagonal elements, $\rho_{rr}$, of the density matrix are the populations of the corresponding states, while the off-diagonal elements are known as coherences. If the off-diagonal elements are non-zero the states $|r\rangle$ and $|s\rangle$ are statistically correlated. The coherence order between spin states $|r\rangle$ and $|s\rangle$ is defined as:

$$p_{rs} = M_r - M_s \tag{5.11}$$

where

$$S_z |r\rangle = M_r |r\rangle \tag{5.12}$$

and

$$S_z |s\rangle = M_s |s\rangle . \tag{5.13}$$

Considering an external magnetic field in thermal equilibrium at a temperature T, in the high-field approximation, the density operator $\rho_{eq}$ is defined as:

$$\rho_{eq} = \frac{e^{\left(-\hbar H_S^Z\right)/(k_B T)}}{Tr\left[e^{\left(-\hbar H_S^Z\right)/(k_B T)}\right]} \tag{5.14}$$

where $\hbar$ is the Plank's constant divided by $2\pi$ and $k_B$ is the Boltzmann constant. Under the *high temperature approximation*, $k_B \gg |\hbar\omega_0|$, $\rho_{eq}$, simplifies:

$$\rho_{eq} = \frac{1}{2}(\mathbb{1} + \mathbb{B} S_z) \tag{5.15}$$

where $\mathbb{1}$ is the unity operator and $\mathbb{B}$ is the Boltzmann factor, which is defined as:

$$\mathbb{B} = \frac{\hbar \gamma_S B_0}{k_B T}. \tag{5.16}$$

The high-temperature approximation is generally fulfilled at room temperature. Commonly the unitary operator $\mathbb{1}$ and the constant $\mathbb{B}$ in Equation 5.15 are neglected leading to a simplified density operator in equilibrium:

$$\rho_{eq} \backsimeq S_z. \tag{5.17}$$

The evolution of the density operator under a time dependent Hamiltonian, $H(t)$, is governed by the *Liouville-von Neumann* equation:

$$\frac{d}{dt}\rho(t) = -i\left[H(t), \rho(t)\right]. \tag{5.18}$$

If the perturbation described by the Hamiltonian, H, is time independent the Liouville-von Neumann equation simplifies to:

$$\rho(t) = e^{-iH(t-t_0)}\,\rho(t_0)\,e^{iH(t-t_0)} \tag{5.19}$$

The density operator at a time point $t_0$ is thereby related to the density operator at a time point $t$ and the propagator $U(t,t_0)$ associated with H:

$$U(t,t_0) = e^{-iH(t-t_0)}. \tag{5.20}$$

In the case of a time-dependent Hamiltonian density operators at time point $t$ and $t_0$ are related:

$$\rho(t) = U(t,t_0)\;\rho(t_0)U^{\dagger}(t,t_0) \tag{5.21}$$

where the propagator solves Equation 5.3.

## 5.3. Average Hamiltonian Theory

The time evolution of a spin system over a time interval $[t,t_0]$ with the propagator $U(t,t_0)$ was introduced previously. This yields analytical solutions if the Hamiltonian is time-independent. However, if the Hamiltonian, $H(t)$, is time-dependent it is generally difficult to derive an analytical solution. *Average Hamiltonian theory* [35; 36] can be used to obtain an analytical approximation of the propagator $U(t,t_0)$. The propagator of the time-independent *effective Hamiltonian*, $\overline{H}$, over an time interval $[t_0, t_0+T]$ becomes:

$$U(t_0, t_0+T) = e^{-i\overline{H}T} \tag{5.22}$$

The effective Hamiltonian can be expressed using the Magnus expansion [37]:

$$\overline{H} = \overline{H}^{(1)} + \overline{H}^{(2)} + \overline{H}^{(3)} + \ldots. \tag{5.23}$$

The first two orders of the Magnus expansion are given by:

$$\overline{H}^{(1)} = \frac{1}{T}\int_{t_0}^{t_0+T} dt\, H(t)$$
$$\overline{H}^{(2)} = \frac{1}{2iT}\int_{t_0}^{t_0+T} dt' \left[H\left(t'\right), H(t)\right]. \tag{5.24}$$

The numbering of the Magnus terms shown employs a consistent scheme, in which the $k$th term is proportional to the product of $k$ Hamiltonians. The term $\overline{H}^{(1)}$ is defined as the average over the Hamiltonian $H(t)$ and thus called the *average Hamiltonian*. The term $\overline{H}^{(2)}$ is known as the *second-order correction* of the average Hamiltonian, a naming that is consistent for all other higher order terms. Provided that for any point t, $t_0 < t < T_0 + T$, the following condition is valid:

$$\|H(t)\|\, T \ll 1, \tag{5.25}$$

the Magnus expansion converges rapidly [38]. The norm, $\|H(t)\|$, may be chosen to be:

$$\|H(t)\| = \sqrt{Tr\left[H(t)^2\right]} \tag{5.26}$$

It is possible to speed up the convergence of the Magnus expansion by transforming the Hamiltonian, $H(t)$, into an appropriate frame called the *interaction* or *toggling frame*. For this purpose the Hamiltonian is expressed in two, generally time-dependent non-commuting, terms:

$$H(t) = H_A(t) + H_B(t), \tag{5.27}$$

and $H_A(t)$ is chosen so that the propagator can be easily determined analytically by solving:

$$\frac{d}{dt}U_A(t) = -iH_A(t)U_A(t). \tag{5.28}$$

The Hamiltonian in the interaction frame, $\tilde{H}(t)$, is obtained by the transformation:

$$\tilde{H}(t) = U_A^{\dagger}(t)H_B(t)U_A(t). \tag{5.29}$$

and its propagator, $\tilde{U}(t)$, is defined as:

$$\frac{d}{dt}\tilde{U}(t) = -i\tilde{H}(t)\tilde{U}(t). \tag{5.30}$$

The propagator $U(t)$ for the total Hamiltonian $H(t)$ is thus given as:

$$U(t) = U_A(t)\tilde{U}(t). \tag{5.31}$$

In solid-state magic-angle spinning NMR it is commonly assumed, that $H_A(t) = H^{RF}(t)$ and $H_B(t) = H^{IA}(t)$, where $H^{IA}(t)$ is the interaction Hamiltonian.

## 5.4. Superoperators and Liouville Space

So far, quantum mechanics have been presented in a linear vector space, the Hilbert space, and two types of objects, kets and linear operators acting on these kets, have been introduced. Analogous mathematical objects can be defined in a larger vector space, the Liouville space, which is the cross product of two Hilbert spaces [39]. The choice of vector space depends on the considered problem. It has been shown that the Liouville space is advantageous if relaxation or chemical exchange are included [40; 41]. Furthermore, it is favourable if spherical tensors, such as in Part III of this thesis, are used to manipulate the density matrix [40; 41].

In the Liouville space the ordinary quantum mechanical operators are considered to be state vectors. A state vector $|\Psi\rangle$ with the dimension $n$ in the Hilbert space posses a dimension $n \times n$ in the corresponding Liouville space [7], in which the ket and bra Liouville space vectors are written as $|Q)$ and $(Q|$, respectively. The scalar product between two Liouville space vectors, also known as the Liouville space bracket, is defined as:

$$(A|B) = \mathrm{Tr}\left\{A^\dagger B\right\} \tag{5.32}$$

where $A^\dagger$ is the Hermitian adjoint of $A$ assuming a finite Liouville space. A *Liouville operator* or *superoperator*, $\hat{C}$, is denoted by a hat and defined as:

$$\hat{C}|B) \equiv |[C,B]), \tag{5.33}$$

$$(A|\hat{C} \equiv \left|\left[C^\dagger, A\right]\right). \tag{5.34}$$

If $\hat{C}$ is an exponential operator Equation 5.33 can be rewritten utilising the op-

erator's series expansion:

$$e^{-it\hat{H}}|B) \equiv \left|e^{-itH}Be^{+itH}\right). \tag{5.35}$$

Consequently,

$$(A|e^{-it\hat{H}} \equiv \left(e^{+itH}Ae^{-itH}\right| \tag{5.36}$$

and

$$\begin{aligned}(A|e^{-it\hat{H}}|B) &\equiv \mathrm{Tr}\left\{A^{\dagger}e^{-itH}Be^{+itH}\right\} \\ &\equiv \mathrm{Tr}\left\{e^{+itH}A^{\dagger}e^{-itH}B\right\}.\end{aligned} \tag{5.37}$$

In the Liouville space the Liouville-von Neumann equation for the density matrix $\rho$ is expressed as:

$$\frac{d}{dt}\left|\rho\right) = -i\hat{H}\left|\rho\right) \tag{5.38}$$

where $\hat{H}$ is a superoperator (Equation 5.33) and $\left|\rho\right)$ is the state vector in the Liouville space. Using the same concepts for obtaining solutions in Hilbert space the formal solution of the Liouville-von Neumann equation is given by [42]:

$$\left|\rho(t)\right) = \hat{U}(t,t_0)\left|\rho(t_0)\right) \tag{5.39}$$

where

$$\frac{d}{dt}\hat{U}(t,t_0) = -i\hat{H}\hat{U}(t,t_0). \tag{5.40}$$

$\hat{U}$ is a unitary superoperator with the following symmetries:

$$\hat{U}^{-1}(t,t_0) = \hat{U}^{\dagger}(t,t_0) = \hat{U}(t_0,t) \tag{5.41}$$

and connected time intervals can be written:

$$\hat{U}(t_0,t) = \hat{U}(t,t_1)\hat{U}(t_1,t_0) \tag{5.42}$$

The solution of Equation 5.40 depends on the properties of $\hat{H}$.

The expectation value of an operator $Q$ is defined as:

$$\langle Q\rangle = \left(Q|\rho\right) \tag{5.43}$$

or

$$\langle Q(t) \rangle = \left( Q \left| \hat{U}(t_0, t) \right| \rho(t_0) \right). \tag{5.44}$$

Chapter 6

# Dipolar Recoupling

The concept of dipolar recoupling as a methodology to reintroduce dipolar couplings — averaged to zero by MAS — was briefly introduced in Section 3.6.. In the following different applications of dipolar recoupling sequences are discussed along with the different average Hamiltonians that can be recoupled. The chapter concludes with a short review of dipolar recoupling sequences focussing of those developed for isolated spin-pairs. Homonuclear dipolar recoupling in multiple-spin systems is discussed separately in Section 8.2.

The various applications of dipolar recoupling sequences cannot always be completely separated. A lot of dipolar recoupling sequences are capable of exciting different coherence orders, where the maximum coherence order in a spin-1/2 system is equivalent to plus/minus the number of spins in the system. However, only single-quantum coherence can be observed directly and thus it is necessary to reconvert zero-, double- and higher order quantum coherences into observable single-quantum coherence before they can be determined. Sequences which select for double-quantum coherence are often applied to a spin-1/2 system with a selectively labelled spin-pair to suppress the natural abundance background. Furthermore, dipolar recoupling sequences are employed to determine internuclear distances. For this purpose the evolution of the NMR-signal intensity is observed as a function of recoupling time and since the evolution depends on the dipolar coupling internuclear distances can be determined. An additional possibility of gaining structural information using dipolar recoupling sequences is the determination of bond- and torsional-angles. These experiments are conducted by determining the relative orientation of two dipolar tensors (or a dipolar and a

chemical shift tensor) through the evolution of double-quantum coherence [43]. Magnetisation exchange is a further application for dipolar recoupling sequences and summarises methods in which magnetisation is transferred between spins through their dipolar coupling. This allows not only to infer the proximity of spins but also sensitivity enhancement of low-$\gamma$ nuclei through heteronuclear dipolar couplings.

## 6.1. Homonuclear Dipolar Recoupling

Homonuclear dipolar recoupling between two like spins $S_j$ and $S_k$ can generate different dipolar average Hamiltonians depending on the recoupling sequence employed. A *homonuclear zero-quantum recoupling* sequences generates a *homonuclear zero-quantum average Hamiltonian* of the form:

$$\begin{aligned}\overline{H}^{(1)} &= \omega_{jk}\frac{1}{\sqrt{6}}\left(2S_{jz}S_{kz}-\frac{1}{2}\left(S_j^-S_k^+ + S_j^+S_k^-\right)\right)\\ &= \omega_{jk}T_{20}^{jk},\end{aligned} \tag{6.1}$$

which is equivalent to the dipolar Hamiltonian in Equation 4.46. This type of Hamiltonian is not only perfect to initialise magnetisation exchange, but also suitable for distance measurements. However, it cannot be used to excite higher order multiple-quantum coherence.

One Hamiltonian capable of exciting higher order multiple-quantum coherence is the *homonuclear single-quantum average Hamiltonian* generated by a *homonuclear single-quantum recoupling* sequences:

$$\begin{aligned}\overline{H}^{(1)} &= \omega_{jk}\frac{1}{2}\left(S_j^-S_{kz}+S_{jz}S_k^-\right)+\omega_{jk}^*\frac{1}{2}\left(S_j^+S_{kz}+S_{jz}S_k^+\right)\\ &= \omega_{jk}T_{2-1}^{jk}-\omega_{jk}^*T_{21}^{jk}.\end{aligned} \tag{6.2}$$

The *homonuclear double-quantum average Hamiltonian* generated by a *homonuclear double-quantum recoupling* sequence takes the form:

$$\begin{aligned}\overline{H}^{(1)} &= \omega_{jk}\frac{1}{2}\left(S_j^-S_k^-\right)+\omega_{jk}^*\frac{1}{2}\left(S_j^+S_k^+\right)\\ &= \omega_{jk}T_{2-2}^{jk}+\omega_{jk}^*T_{22}^{jk},\end{aligned} \tag{6.3}$$

and is extensively used for distance determination.

## 6.2. HETERONUCLEAR DIPOLAR RECOUPLING

Just as in the homonuclear case different recoupling sequences yield different heteronuclear dipolar average Hamiltonians. Considering two unlike spins $I_j$ and $S_k$ four different average Hamiltonians can be generated. The *longitudinal two-spin average Hamiltonian* has the form:

$$\begin{aligned}\overline{H}^{(1)} &= \omega_{jk} I_{jz} S_{kz} \\ &= \omega_{jk} T^j_{10} T^k_{10}.\end{aligned} \tag{6.4}$$

The terms $I_{jz}$ and $S_{kz}$ commute for different spin-pairs. Consequently, it is permitted to describe the evolution of a heteronuclear multiple-spin system as the superposition of the evolution of isolated spin-pairs. This property is exploited in many heteronuclear recoupling sequences and is the reason that distance estimations in heteronuclear multiple-spin systems can be conducted successfully. In the homonuclear case flip-flop terms which do not commute if they contain one identical spin are present and account for the dipolar truncation problem. This makes distance estimations in homonuclear multiple-spin systems successful only in certain cases.

*Hetoronuclear zero-quantum* recoupling yields a *heteronuclear zero-quantum average Hamiltonian*:

$$\begin{aligned}\overline{H}^{(1)} &= \omega_{jk} I^-_j S^+_k + \omega^*_{jk} I^-_j S^+_k \\ &= \omega_{jk} (-2) T^j_{11} T^k_{1-1} + \omega^*_{jk} 2 T^j_{1-1} T^k_{11},\end{aligned} \tag{6.5}$$

which is suitable to observe magnetisation exchange and does, just as its homonuclear counterpart, not allow the excitation of higher order multiple-quantum coherence.

Excitation of higher order multiple-quantum coherences is possible choosing a *heteronuclear single-quantum average Hamiltonian* as starting point:

$$\begin{aligned}\overline{H}^{(1)} &= \omega_{jk} I_{jz} S^-_k + \omega^*_{jk} I_{jz} S^+_k \\ &= \omega_{jk} \sqrt{2} T^j_{10} T^k_{1-1} + \omega^*_{jk} \left(-\sqrt{2}\right) T^j_{10} T^k_{11}.\end{aligned} \tag{6.6}$$

This Hamiltonian is generated by a *heteronuclear single-quantum recoupling* sequence.

The *heteronuclear double-quantum average Hamiltonian* as it is generated by a *heteronuclear double-quantum recoupling* sequence is given by:

$$\begin{aligned}\overline{H}^{(1)} &= \omega_{jk} I_j^- S_k^- + \omega_{jk}^* I_j^- S_k^+ \\ &= \omega_{jk}(-2) T_{11}^j T_{11}^k + \omega_{jk}^* 2 T_{1-1}^j T_{1-1}^k, \end{aligned} \tag{6.7}$$

and allows the excitation of higher order multiple quantum coherence.

## 6.3. Recoupling Sequences

There are two distinct ways of manipulating a spin system in solid-state NMR, one is the spatial manipulation by means of sample rotation around a single or several fixed axes and the other one is the spin rotation by rf-pulses. The combination of both techniques is the basis for almost all recoupling schemes.

The first homonuclear decoupling scheme, DRAMA, uses two strong rotor-synchronised $\pi/2-$pulses to generate a mixed zero- and double-quantum Hamiltonian [18; 19]. To date DRAMA has been replaced by more robust homonuclear recoupling schemes such as rotational resonance (RR) [44], RFDR [45; 46] and symmetry sequences [47; 48; 49].

Rotational resonance utilises the mechanical interference that occurs if the sample spinning, $\omega_r$, is equivalent to the isotropic chemical shift separation between the two investigated spins, $\Delta_{iso} = n\omega_r$, with $n$ being a small integer. It generates a homonuclear zero-quantum average Hamiltonian. Although, initially developed for isolated spin-pairs, rotational resonance is one of the few homonuclear dipolar recoupling sequences which has been successfully applied to multiple-spin systems [50; 51; 52]. This can be attributed to the selectivity of the sequence which introduces only the dipolar coupling within a desired spin-pair.

Radio frequency driven dipolar recoupling (RFDR) generates magnetisation transfer and therefore cross peaks between coupled resonance in a 2D NMR spectrum. Magnetisation exchange occurs via a pure homonuclear zero-quantum average Hamiltonian and is established by rotor-synchronised rf-pulses [45; 46].

Similar to DRAMA, DRAWS (dipolar recoupling with a windowless sequence) generates a mixed zero- and double-quantum homonuclear dipolar average Hamiltonian and overcomes several problems such as a strong interference from CSA

and narrow spectral ranges encountered for DRAMA or RR [53].

For distance estimations homonuclear dipolar recoupling sequences that generate a double-quantum or zero-quantum average Hamiltonians are usually employed. An early sequence that excites double-quantum coherence is the HORROR scheme (homonuclear rotary resonance) which is very efficient at controlling the angular orientation of the recoupled Hamiltonian. Unfortunately the sequence is sensitive to isotropic chemical shift differences and chemical shift anisotropies which can quench the dipolar recoupling [54].

The problems encountered for HORROR have been overcome in the C7-sequence [47] and its variants POST-C7 [48], CMR7 [55] and DREAM [56]. All sequences excite double-quantum coherence very efficiently. These sequence were extended to the general symmetry principles of C- and R-symmetries and can generate a variety of homo- and heteronuclear average Hamiltonians [57].

The most successful heteronuclear recoupling scheme is REDOR (rotational-echo double-resonance) which generates a longitudinal two spin term, by $\pi-$pulses that are applied synchronised with the rotor frequency [17]. The underlying spin-echo experiment is a common feature of heteronuclear recoupling [58].

Chapter 7

# Spin-Echo Experiments

The spin-echo experiment (Figure 7.1) was initially developed for NMR in inhomogeneous fields. It starts by rotating longitudinal magnetisation (1) into the

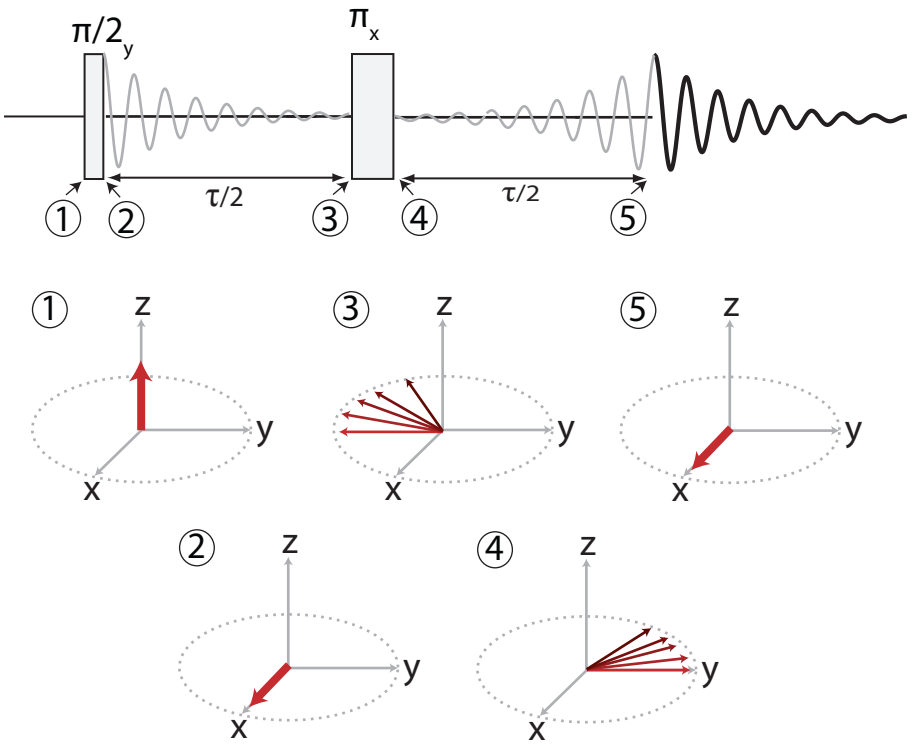


Figure 7.1: Spin echo scheme: (1) the sequence starts with longitudinal magnetisation which is rotated into the transverse plane and aligned along the x-axis (2). Transverse magnetisation evolves for a period $\tau/2$ (3) at which it is inverted (4). It now evolves for another period $\tau/2$ at whose end it again aligns along the x-axis (5).

transverse plane (2) — here magnetisation is rotated by a $\pi/2-$pulse around the y-axis generating x-magnetisation. During the first evolution-time ($\tau/2$) magnetisation evolves and dephases in the transverse plain (3). At the end of the first evolution period transverse magnetisation is rotated by a flip-angle $\pi$ around the x-axis (3). In the subsequent second evolution period magnetisation refocuses along the x-axis (5).

The same spin dynamics described with the vector picture above can be described using a mathematical description. For a single, $S_{jz}$ the propagator for the spin-echo sequence is takes the form:

$$\begin{aligned} U(t) &= e^{-i\omega\frac{\tau}{2}S_{jz}} e^{-i\pi S_{jx}} e^{-i\omega\frac{\tau}{2}S_{jz}} \\ &= e^{-i\omega\frac{\tau}{2}S_{jz}} \left( e^{-i\pi S_{jx}} e^{-i\omega\frac{\tau}{2}S_{jz}} e^{i\pi S_{jx}} \right) e^{-i\pi S_{jx}} \\ &= e^{-i\omega\frac{\tau}{2}S_{jz}} e^{i\omega\frac{\tau}{2}S_{jz}} e^{-i\pi S_{jx}} \\ &= e^{-i\pi S_{jx}} \end{aligned} \tag{7.1}$$

Assuming an initial density operator of $\rho(0) = S_{jx}$ the density operator $\rho(t)$ at the end of the sequence is:

$$\begin{aligned} \rho(t) &= U(t)\rho(0)U^{\dagger}(t) \\ &= e^{-i\pi S_{jx}} S_{jx} e^{i\pi S_{jx}} \\ &= S_{jx} \\ &= \rho(0). \end{aligned} \tag{7.2}$$

Provided the two spin-echo modulation times $\frac{\tau}{2}$ are identical, and in a rotating solid equivalent to an integer number of rotor periods, the spin-echo sequence can be used to refocus all spin Hamiltonian terms that are linearly proportional to the z-component of the spin angular momentum. This is the case for isotropic and anisotropic chemical shifts as well as heteronuclear dipolar couplings.

In the presence of two homonuclear spins $S_j$ and $S_k$ the average Hamiltonian for the evolution under the weak coupling approximation is given as:

$$\begin{aligned} \overline{H}^{(1)} &= H^Z + H^{CL} \\ &= \omega_j S_{jz} + \omega_k S_{kz} + \omega_{jk} S_{jz} S_{kz}, \end{aligned} \tag{7.3}$$

where $H^Z$ is the Zeeman Hamiltonian and $H^{CL}$ the coupling Hamiltonian, which can comprise direct and indirect dipolar couplings. For the two spin case the

propagator takes the form:

$$U(t) = e^{-i\frac{\tau}{2}H^Z} e^{-i\frac{\tau}{2}H^{CL}} e^{-i\pi S_{jx}+S_{kx}} e^{-i\frac{\tau}{2}H^{CL}} e^{-i\frac{\tau}{2}H^Z}. \tag{7.4}$$

Assuming an initial density operator of $\rho(0) = S_{jx} + S_{kx}$ the density operator $\rho(t)$ can then be derived:

$$\begin{aligned}
\rho(t) &= U(t)\rho(0)U^{\dagger}(t) \\
&= e^{-i\frac{\tau}{2}H^Z} e^{-i\frac{\tau}{2}H^{CL}} e^{-i\pi S_{jx}+S_{kx}} e^{-i\frac{\tau}{2}H^{CL}} e^{-i\frac{\tau}{2}H^Z} \left(S_{jx}+S_{kx}\right) \times \\
&\quad e^{i\frac{\tau}{2}H^Z} e^{i\frac{\tau}{2}H^{CL}} e^{i\pi S_{jx}+S_{kx}} e^{i\frac{\tau}{2}H^{CL}} e^{i\frac{\tau}{2}H^Z} \qquad (7.5) \\
&= e^{-i\tau H^{CL}} \left(S_{jx}+S_{kx}\right) \\
&= e^{-i\tau H^{CL}} \rho(0). \qquad (7.6)
\end{aligned}$$

Equations 7.2 and 7.6 demonstrate that the isotropic chemical shift terms are refocussed by the spin-echo experiment no matter whether applied to a single spin or a coupled two spin system. Moreover, it is shown that the spin-echo evolution for coupled spins is modulated by the coupling Hamiltonian. This modulation makes it feasible to determine coupling constants in the solid-state from spin-echo evolution curves.

The spin-echo modulation in the homonuclear case is now discussed in more detail choosing a weak J-coupling as coupling term and omitting the isotropic chemical shift evolution since it is refocusses. Under these conditions the coupling Hamiltonian can be written as:

$$\begin{aligned}
H^{CL} &= \omega_{jk} S_{jz} S_{kz} \\
&= 2\pi J_{jk} S_{jz} S_{kz} \\
&= 2\pi J_{jk} T^j_{10} T^k_{10}. \qquad (7.7)
\end{aligned}$$

Starting point of the evolution during the spin-echo is the same initial density operator that was chosen in the more general coupled case above:

$$\begin{aligned}
\rho(0) &= S_{jx} + S_{kx} \\
&= \frac{\sqrt{2}}{2}\left(T^j_{1-1} - T^j_{11} + T^k_{1-1} - T^k_{11}\right) \qquad (7.8)
\end{aligned}$$

The the density operator during the spin-echo sequence (Figure 7.1) evolves as

follows:

$$\frac{\sqrt{2}}{2}\left(T^j_{1-1}-T^j_{11}+T^k_{1-1}-T^k_{11}\right)\xrightarrow{2\pi J_{jk}\frac{\tau}{2}T^j_{10}T^k_{10}}\cos\left[\pi J_{jk}\frac{\tau}{2}\right]\frac{\sqrt{2}}{2}\left(T^j_{1-1}-T^j_{11}+T^k_{1-1}-T^k_{11}\right)+\sin\left[\pi J_{jk}\frac{\tau}{2}\right]2i\left(T^{jk}_{21}+T^{jk}_{2-1}\right) \tag{7.9}$$

$$\xrightarrow{\pi\frac{\sqrt{2}}{2}\left(T^j_{1-1}-T^j_{11}\right)+\pi\frac{\sqrt{2}}{2}\left(T^k_{1-1}-T^k_{11}\right)}\cos\left[\pi J_{jk}\frac{\tau}{2}\right]\frac{\sqrt{2}}{2}\left(T^j_{1-1}-T^j_{11}+T^k_{1-1}-T^k_{11}\right)+\sin\left[\pi J_{jk}\frac{\tau}{2}\right]2i\left(T^{jk}_{21}+T^{jk}_{2-1}\right) \tag{7.10}$$

$$\xrightarrow{2\pi\frac{\tau}{2}J_{jk}T^j_{10}T^k_{10}}\cos\left[\pi J_{jk}\tau\right]\frac{\sqrt{2}}{2}\left(T^j_{1-1}-T^j_{11}+T^k_{1-1}-T^k_{11}\right)+\sin\left[\pi J_{jk}\tau\right]2i\left(T^{jk}_{21}+T^{jk}_{2-1}\right) \tag{7.11}$$

Starting of with transverse magnetisation Equation 7.9 demonstrates the evolution of the J-coupling over a period $\frac{\tau}{2}$ (time interval (2)-(3) in Figure 7.1). This results in a modulation of the rank-1 terms by a cosine funtion, while the rank-2 terms are modulated by a sine function. The adjacent inversion pulse has no net effect on the terms at time point (3), thus, they are identical at time point (4) (Equation 7.10). The second evolution period, (4)-(5), adds to the modulation frequency (Equation 7.11), but has no effect further effect of the terms.

A more detailed treatment of spin-echo modulations in solids can be found in reference [59] for J-couplings and in references [60; 61] for dipolar-couplings and J-couplings.

# Part III

# Off-Magic Angle Spinning and Spherical Tensor Analysis for the Estimations of Dipolar Couplings

—

# STARS

Chapter 8

# Introduction

Dipolar couplings are proportional to the inverse cube of the distance between the two spins in a spin-pair, thereby containing valuable information for structure calculations of molecules such as proteins, polymers and glasses. This distance dependence makes solid-state NMR a powerful tool for molecular structure determination especially if other techniques are not feasible. However, most applications of solid-state NMR rely on the use of MAS, which averages anisotropic interactions, such as the dipolar coupling, to zero. For the last 20 years dipolar recoupling techniques have been established as valuable tool to extract internuclear distance information in magic-angle spinning solid-state NMR. In isolated spin-pairs, which possess simple spin dynamics, a wide variety of recoupling methods are available to accurately determine dipolar couplings and, subsequently, precise distances. For the more complex case of a multiple-spin system data interpretation is difficult; spin dynamics are dominated by short-range couplings with little influence from structurally interesting long-range couplings. The multiple-spin case is discussed in more detail in the following Section.

## 8.1. Spin Dynamics in Multiple-Spin Systems

Considering, many connected homonuclear spin-systems with coupled spins-1/2 in a high magnetic field the nuclear spin Hamiltonian is given by:

$$H = \sum_j H_j + \sum_{j<k} H_{jk} \tag{8.1}$$

and depends on the individual spin-field interactions, $H_j$, and the spin-spin interactions, $H_{jk}$. In most cases the coupling Hamiltonians for connected spin-pairs do not commute:

$$[H_{jk}, H_{kl}] \neq 0. \tag{8.2}$$

It is this non-commutativity that makes it very difficult to disentangle the effect of an individual spin-spin coupling from the others, especially, if the coupling of interest is smaller than the other couplings. In solid-state NMR this is observed as dipolar truncation [22], where small dipolar couplings are averaged by larger ones.

A similar situation termed *strong coupling* is known from liquid-state NMR, the strong coupling spin Hamiltonian is given by:

$$H^0_{strong} = \sum_j \omega^0_j S_{jz} + \sum_{j<k} 2\pi J_{jk} \mathbf{S}_j \cdot \mathbf{S}_k \tag{8.3}$$

and the term $2\mathbf{S}_j \cdot \mathbf{S}_k$ does not commute. The spin Hamiltonian in an isotropic liquid, however, can be simplified, if the chemical shift part of the Hamiltonian is larger than the J-coupling part of the Hamiltonian:

$$|\omega^0_j - \omega^0_k| \gg |\pi J_{jk}|. \tag{8.4}$$

The system is then described as *weakly coupled* and its Hamiltonian is given by:

$$H^0_{weak} = \sum_j \omega^0_j S_{jz} + \sum_{j<k} 2\pi J_{jk} S_{jz} S_{kz} \tag{8.5}$$

where the *truncated* spin-spin coupling terms $H^0_{jk}$ commute with each other:

$$[S_{jz}, S_{kz}] = 0 \tag{8.6}$$

and with the spin field terms $H_j$. Under the weak-coupling approximation not only spin-pairs but also a multiple-spin systems commute, e.g. a three spin system:

$$[S_{jz}S_{kz}, S_{kz}S_{lz}] = 0 \tag{8.7}$$

This favourable character is the basis of most solution NMR methodology [32; 62].

The weak-coupling approximation is also valid in some cases of broad-line solid-state NMR. In static solids isotropic and anisotropic chemical shifts create a

frequency dispersion which can give rise to weak coupling for the spin-spin interactions. For spin-1/2 rapid sample rotation about an axis away from the magic-angle generates scaled dipolar couplings which are often truncated by the isotropic and anisotropic chemical shifts [63; 64].

The ability to truncate the non-commuting dipolar interactions by frequency dispersion is a common starting point for the emerging dipolar recoupling technology in multiple-spin systems. The average Hamiltonian under these sequences can be written as:

$$\overline{H} = \sum_j \overline{H}_j^0 + \sum_{j<k} \left( \overline{H}_{jk}^0 + \overline{H}_{jk}^{\pm} \right) \tag{8.8}$$

where $\overline{H}_j^0$ is the frequency dispersion interactions of spins $S_j$ and the diagonal and off-diagonal parts of the recoupled dipolar interaction in the Zeeman basis are given by $\overline{H}_{jk}^0$ and $\overline{H}_{jk}^{\pm}$, respectively. In the experiments introduced in my thesis dipolar couplings are recoupled by off-magic angle spinning, which allows frequency dispersion by isotropic and anisotropic chemical shifts. In this case the average Hamiltonian terms may be written:

$$\overline{H}_j^0 = \overline{\omega}_j^0 S_{jz} \tag{8.9}$$

$$\overline{H}_{jk}^0 = \overline{\omega}_{jk}^0 2 S_{jz} S_{kz} \tag{8.10}$$

$$\overline{H}_{jk}^{\pm} = \overline{\omega}_{jk}^{\pm} \frac{1}{2} \left( S_j^+ S_k^- + S_j^- S_k^+ \right) \tag{8.11}$$

with

$$\overline{\omega}_{jk}^0 = \overline{\omega}_{jk}^{DD} + \pi J_{jk} \tag{8.12}$$

$$\overline{\omega}_{jk}^{\pm} = \overline{\omega}_{jk}^{DD} + 2\pi J_{jk} \tag{8.13}$$

where $\overline{\omega}_{jk}^{DD}$ is the recoupled dipolar interaction between spins $S_j$ and $S_k$. If all spin-pairs satisfy the weak-coupling condition,

$$|\overline{\omega}_j^0 - \overline{\omega}_k^0| \gg |\overline{\omega}_{jk}^{\pm}|, \tag{8.14}$$

the coupling terms $\overline{H}_{jk}^{\pm}$ may be truncated. Several attempts to overcome the dipolar truncation problem by truncating the coupling terms $\overline{H}_{jk}^{\pm}$ have been made and are discussed in the following Section.

## 8.2. Homonuclear Dipolar Recoupling in Multiple-Spin Systems

Early research on dipolar recoupling methodology was targeted at isolated spin-pairs and focussed on improving resolution and robustness. In the last decade aim shifted towards enabling a broader range of applications, especially targeted at multiply labelled compounds [21; 24; 65], which suffer from complicated spin dynamics. These spin dynamics lead to dipolar truncation — the attenuation of the interactions between distant spins by the presence of stronger couplings to close spins.

Bayro *et al.* analysed the dipolar truncation effect by employing standard zero- and double quantum recoupling sequences to uniformly and alternating labelled tri-peptides. Thereby, it was demonstrated that precise distances above 3 Å are not accessible in a multiple-spin system [22]. Moreover, alternating labelling schemes reduce the effect of dipolar truncation, but cannot solve the problem.

Although initially developed for isolated spin-pairs various types of frequency selective techniques, including rotational resonance (RR) [44; 50; 51; 52], can be used to access homonuclear dipolar couplings in multiple-spin systems. Application of RR to a multiple-spin system show distance estimations in uniformly $^{13}$C-labelled threonine with an accuracy better than 10% (deviation from the X-ray distance) and theoretical studies indicate that distance estimations up to 4.5 Å are possible [51]. However, RR requires relatively large isotropic chemical shift difference between investigated spins which limits spinning frequencies to a certain — field dependent — range. The spin dynamics in the RR experiment depend on zero-quantum parameters, this dependence is greatly reduced in the rotational resonance tickling (R2T) experiment which ramps the rf-field through the RR condition [66].

Chemical shift assisted dipolar recoupling sequences targeted at multiple-spin systems emerged over the last decade and produce secularised zero- or double-quantum dipolar Hamiltonians. The truncated dipolar recoupling (TDR) method [26], the triple oscillating field technique (TOFU) [29], the zero-quantum shift evolution assisted selective homonuclear recoupling (ZQ-SEASHORE) [31] and the dipolar-coupling-mediated total correlation spectroscopy (DTOCSY) [67] produce a zero-quantum dipolar Hamiltonian, whereas each the original shift-evolution assisted selective homonuclear recoupling (SEASHORE) [25] and the sto-

chastic dipolar recoupling (SDR) [27; 28] technique generate a double-quantum dipolar Hamiltonian. TDR is a frequency-selective technique, which utilises the symmetry based $C_3^1$ recoupling technique [49] to reintroduce zero-quantum homonuclear dipolar coupling terms along with the isotropic and anisotropic chemical shift terms [26]. Unfortunately, it also recouples undesired heteronuclear spin interactions therefore requiring high heteronuclear decoupling fields, which were avoided by the authors using deuterated samples. Based on the TDR method DTOCSY [67] was introduced recently removing adverse effects due to insufficient heteronuclear decoupling. The TOFU [29] technique and its advancement the four oscillating field technique (FOLD) [30] use three or four oscillating fields, respectively, to recouple the the zero-quantum homonuclear dipolar interactions while retaining the isotropic chemical shifts. FOLD recouples with a 2.5 times higher scaling factor than TOFU. Both techniques consist of a main and a reference experiment, thus a relaxation independent experimental ratio is compared to a Fresnel grid. Distance estimations have been attempted up to 2.9Å for TOFU and between 4–5 Å with FOLD, an accuracy of ±0.2 Å is claimed. The frequency-selective ZQ-SEASHORE methodology consists of alternating blocks of homonuclear dipolar zero-quantum recoupling by fpRFDR [46; 68] and chemical shift evolution. SEASHORE is a double-quantum complement to ZQ-SEASHORE and dipolar recoupling is achieved utilising POST-C7 [48], distances up to 3.0 Å were estimated. POST-C7 [48] is also used in the SDR scheme [27; 28] to accomplish homonuclear dipolar double-quantum recoupling. The broad-band recoupling sequence SDR was demonstrated on up to five spins, but no dipolar couplings were estimated.

In recent years another class of recoupling methods has emerged which accomplishes homo- or heteronuclear recoupling with the assistance of protons. This type of sequence is referred to as second order recoupling method because the average Hamiltonian (first order effective Hamiltonian) vanishes in an appropriate interaction frame and recoupling occurs via the higher order terms. The most familiar experiment in this recoupling class is proton-driven spin diffusion (PDSD) [23]. In a PDSD experiment the polarisation transfer is mediated by the second order effective Hamiltonian that is a cross term between two dipolar couplings. This transfer mechanism is different to the ones discussed so far and allows the observation of small dipolar couplings in the presence of strong couplings without sever dipolar truncation effects [69]. However, the precision of proton assisted recoupling method is generally not very high [21] and thus, precise methods for distance estimations in multiple-spin systems are still needed.

Despite recent advances in the application of dipolar recoupling sequences there is still a need for a methodology that achieves precise determination of dipolar couplings over a wide range of experimental conditions. A new frequency-selective technique is introduced in my thesis which utilises off-magic-angle spinning to achieve dipolar recoupling. This is combined with a spin-echo pulse scheme and spherical tensor analysis (STA). To restore the spectral resolution lost by off-magic-angle spinning the technique is then extend to a switched angle spinning alternative. In the following off-magic-angle spinning, switched angle spinning and STA are reviewed.

## 8.3. Off-Magic-Angle Spinning NMR

Over the last decade *residual dipolar couplings* or RDCs have evolved into one of the most important sources for structural and dynamical information of biomolecules in solution [70; 71]. The averaging of the dipolar couplings due to isotropic tumbling is prevented by dissolving the sample in oriented media, such as liquid crystals. This introduces macroscopic orientation into the sample, where the degree of solute alignment with $B_0$ — the level of orientation dependence — is tunable [70]. Thus, it is possible to determine residual dipolar couplings while preserving high spectral resolution and sensitivity. RDCs are manifested by small splittings in the spectral peak; under isotropic conditions the peak is split only by the J-coupling, while in the anisotropic case the small dipolar coupling component contributes to the splitting. This allows the precise determination of residual dipolar couplings. However, the value of the RDCs depends on the position of the nuclei involved in the structure of the solute as well as on the degree and direction of alignment. The parameters describing this orientation dependence need to be determined [72] before the RDCs can be used to gain structural information.

In solid-state NMR magic-angle spinning emulates the isotopic tumbling of the liquid-state preserving only isotropic chemical shifts and J-couplings. The solid-state analogue of the liquid-state RDC effect can be introduced by off-magic angle spinning in the solid-state. The degree of orientation dependence or the scaling factor of the anisotropic interactions under sample spinning at various angles $\beta_{RL}$ with respect to $B_0$ is illustrated in Figure 8.1.

Under magic-angle spinning it is possible to estimate small J-couplings in solids

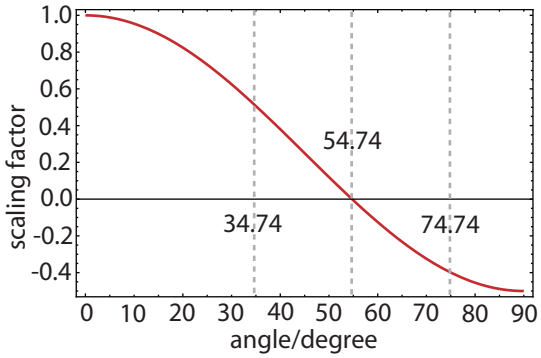


Figure 8.1: Anisotropic scaling factors under sample spinning as a function of the angle $\beta_{RL}$ with respect to $B_0$. The magic-angle at 54.74°and the maximum angle variation (34.74–74.74°) that can be achieved on a DOTY-3mm-switched angle spinning probe are indicated.

by determining the modulation frequency for a spin-echo even in cases where the J-coupling cannot be observed directly [73]. If the spin-echo is acquired under off-magic angle conditions then it is additionally modulated by residual dipolar couplings — an effect analogous to the one described in oriented media [60]. Pileio *et al.* demonstrated on an isolated spin-pair that significant changes in the modulation frequency of the spin-echo can be observed even if the the deviation from the magic-angle is only a fraction of a degree, which allows estimations of dipolar couplings without significantly degrading the spectral resolution and without introducing strongly coupled spin dynamics. This makes the recoupling of dipolar couplings by off-magic angle spinning using a rotor synchronised spin-echo a simple alternative to the often complicated rf-pulse based recoupling schemes [60].

Replacing the strong $\pi$-pulse by a dual-band frequency-selective pulse the spin-echo experiment allows dipolar coupling estimations in multiply-labelled spin systems. Single bond distances could be accurately determined by fitting the experimental results to the analytical expression. However, if the spin-echo evolution is not modulated by a J-coupling, as it is the case for structurally interesting long-range couplings, and the dipolar coupling is small then an exponential decay is observed at small magic-angle offsets. This exponential decay results from the very low frequency of the recoupled coupling such that the modulation occurs well outside the observable spin-evolution time. It makes reliable fitting of the experimental results difficult, since both, the dipolar coupling and the spin relaxation, are described by an exponential decay which are hard to disentangle during the fitting. Thus, it is difficult to obtain the desired dipolar couplings for

small couplings and the magic-angle offset needs to be increased (~10°). Such an increase in the spinning angle significantly deteriorates the spectral resolution and sensitivity, a problem that can be overcome using switched-angle spinning [63; 64; 74].

## 8.4. Switched-Angle Spinning NMR

Switching the rotation angle during a solid-state NMR experiment is a concept that is used in solid-state NMR for more than two decades. Different implementations are distinguished such as *variable-angle spinning* (VAS) [75; 76] and *switched-angle spinning* (SAS) [63; 64; 74]. Under variable-angle spinning several independent experiments at various $\beta_{RL}$ are recorded and combined to yield correlations of isotropic and anisotropic chemical shifts [75] or to extrapolate heteronuclear dipolar couplings [76]. Of more importance for the following work is switched-angle spinning NMR, in which magnetisation is excited off-magic angle while the signal is observed on the magic angle. The three main applications for switched-angle spinning NMR are: (i) determination of long-range dipolar couplings [63; 64]; (ii) isotropic-anisotropic correlation spectra [64; 74; 77]; (iii) application to strongly oriented liquid crystalline samples [77; 78].

## 8.5. Spherical Tensor Analysis

The spin density operator is a superposition of spherical signal components. All spherical signal components evolve separately during an NMR experiment and give rise to the observed NMR signal. Thus, the NMR signal is a superposition of spherical signal components, which originate from different spherical tensor operators. Van Beek *et al.* introduced a methodology which allows the decomposition of the NMR signal into individual spherical components, a procedure referred to as *spherical tensor analysis* (STA) [79].

In a generic pulse sequence, $S_0$, (Figure 8.2) an excitation sequence, $U_0$, is applied to the initial density operator, $\rho_0$, and generates a complex spin state. During the adjacent reconversion sequence, $V_0$, this complex spin state is reconverted into observable single quantum coherence, and consequently detected. The excitation and reconversion blocks in Figure 8.2 can be replaced by any combination of rf-pulses and free evolution periods.

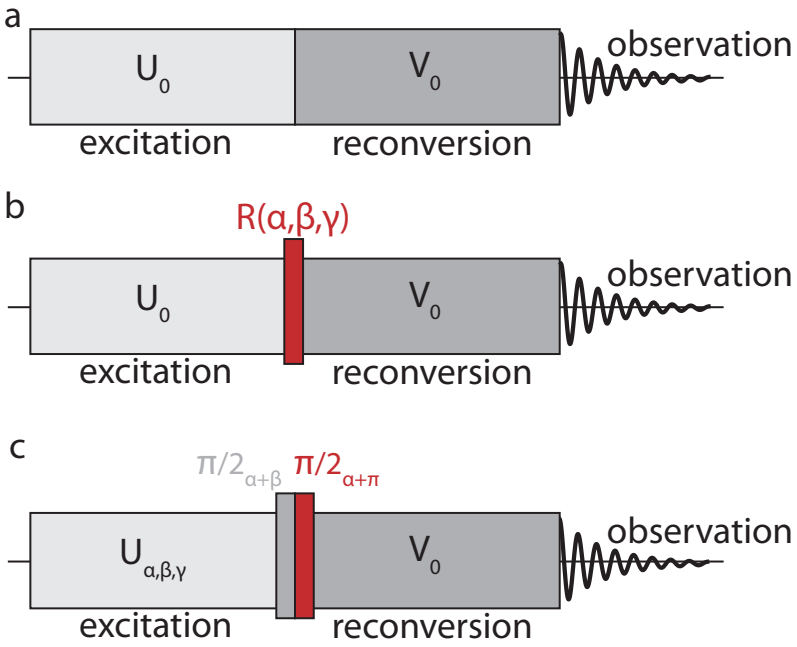


Figure 8.2: Schematic representation of the STA experiment. a) During the excitation sequence $U_0$ a set of spin operators is generated and then reconverted into observable single quantum coherence during $V_0$. Subsequently, the NMR signal is acquired. b) An idealised rotation $R[\alpha,\beta,\gamma]$ is inserted between the excitation and reconversion block. c) Practical implementation of the STA procedure [79].

The complex NMR signal, $s(S_0,t)$, detected at the end of $S_0$ is given by:

$$s(S_0,t) = (S^+|\widehat{W}_{det}(t)\,\widehat{V}_0\,\widehat{U}_0|\rho_0). \tag{8.15}$$

A mathematical representation of the pulse sequence is given by the excitation superoperator, $\widehat{U}_0$, the reconversion superoperator, $\widehat{V}_0$, and the superoperator during detection, $\widehat{W}_{det}$. The Liouville-space bracket is defined:

$$(A|B) = Tr\{A^\dagger B\}. \tag{8.16}$$

Considering the definition of irreducible spherical tensors in Equation 4.17 the NMR signal derived by $S_0$ can be expressed as:

$$s(S_0,t) = \sum_{\Lambda}\sum_{\lambda\mu}\left(S^+|\widehat{W}_{det}(t)\,\widehat{V}_0|T^{\Lambda}_{\lambda\mu}\right)\left(T^{\Lambda}_{\lambda\mu}|\widehat{U}_0|\rho_0\right). \tag{8.17}$$

Rewriting the NMR signal $s(S_0,t)$ as sum of *spherical signal components* yields:

$$s(S_0,t) = \sum_{\lambda\mu} s^0_{\lambda\mu}(t), \tag{8.18}$$

where the spherical component $s^0_{\lambda\mu}(t)$ is written:

$$s^0_{\lambda\mu}(t) = \sum_{\Lambda} \left( S^+ | \widehat{W}_{det}(t) \widehat{V}_0 | T^{\Lambda}_{\lambda\mu} \right) \left( T^{\Lambda}_{\lambda\mu} | \widehat{U}_0 | \rho_0 \right). \tag{8.19}$$

and corresponds to the part of the NMR signal with given spherical tensor operators at the end of the excitation block. In a STA experiment the spherical signal components, $s^0_{\lambda\mu}(t)$, are aimed to be decomposed completely based on their spherical rank $\lambda$ and their spherical component $\mu$.

If a rotation $R[\Omega]$ with Euler angles $\Omega = \{\alpha,\beta,\gamma\}$ is inserted into the pulse sequence, $S_0$, following the excitation block, $U_0$, then the NMR signal of the modified sequence $S_\Omega$ is given as:

$$s(S_\Omega,t) = (S^+ | \widehat{W}_{det}(t) \widehat{V}_0 \widehat{R}_z[\alpha] \widehat{R}_y[\beta] \widehat{R}_z[\gamma] \widehat{U}_0 | \rho_0) \tag{8.20}$$

and van Beek *et al.* have shown that this is equivalent to the implementation depicted in Figure 8.2.c. The NMR signal of a sequence with an inserted rotation can subsequently be written as:

$$s(S_{\Omega,t}) = \sum_{\lambda\mu'\mu} D^{\lambda}_{\mu'\mu}[\Omega]\, \sigma_{\lambda\mu'\mu}(t) \tag{8.21}$$

with the *generalised spherical signal component* defined as:

$$\sigma_{\lambda\mu'\mu}(t) = \sum_{\Lambda} \left( S^+ | \widehat{W}_{det}(t) \widehat{V}_0 | T^{\Lambda}_{\lambda\mu} \right) \left( T^{\Lambda}_{\lambda\mu} | \widehat{U}_0 | \rho_0 \right). \tag{8.22}$$

The effect of the inserted rotation is a modulation of the generalised spherical signal component according to the corresponding Wigner matrix element.

Implementation of a STA-experiment requires the acquisition of $N$ different pulse sequences $S_{\Omega_i}$ with a given set of Euler angles $\Omega_i = \{\alpha_i,\beta_i,\gamma_i\}$ from a collection $\Omega$. A different NMR signal $s(S_{\Omega_i},t)$ is observed for each $S_{\Omega_i}$ and all signals $s(S_{\Omega_i},t)$ are stored separately. Afterwards the $N$ independent experiments are

combined according to:

$$\sigma^{STA}_{\lambda\mu'\mu}(t) = \sum_{i=0}^{N-1} (2\lambda+1)\,\omega_i\, D^{\lambda^*}_{\mu'\mu}[\Omega_i]\; s(S_{\Omega_i}, t) \tag{8.23}$$

where $\omega_i$ refers to an intrinsic scaling given by the chosen sampling set, and is uniform for a regular angle set [80; 81]. The weighting factors, $\omega^i_{\lambda,\mu',\mu}$, applied during processing are thus given by:

$$\omega^i_{\lambda\mu'\mu} = (2\lambda+1)\,\omega_i\, D^{\lambda^*}_{\mu'\mu}[\Omega_i] \tag{8.24}$$

A collection of Euler angles with $N$ sets $\Omega_i = \{\alpha_i, \beta_i, \gamma_i\}$ is chosen such as

$$\sum_i w_i D^{\lambda}_{\mu 0}[\Omega_i] = 0 \text{ for } 1 \leqslant \lambda \leqslant \lambda_{max} \tag{8.25}$$

$$= 1 \text{ for } \lambda = 0 \tag{8.26}$$

where it is assumed that the third Euler angle is fixed at $\gamma_i = 0$. Such angle sets are called two-angle sets and can be derived from the geometrical properties of the regular polyhedra. These two angle sets allow to resolve the NMR signal into spherical signal components up to including $\lambda_{max} = 5$. This means that spherical signal components up to rank-5 can be resolved without contributions from other ranks and that the components $\mu$ take the values $-\lambda \leq \mu \leq \lambda$. Higher ranks can be resolved employing three-angle sets and satisfy a generalised version of Equation 8.25.

## 8.6. Effective Dipolar Couplings

In an undiluted multiple-spin system a spin $S_j$ is connected by intra- and intermolecular dipolar couplings of different magnitudes to the surrounding spins. Such a dipolar coupling network makes it difficult to access a single dominant dipolar coupling and it has been shown [82] that the experimental accessible *effective dipolar coupling* is given by the root-sum-square coupling

$$b_{rss,j} = \sqrt{\sum_{k\neq j} b^2_{jk}}. \tag{8.27}$$

Root-sum-square dipolar couplings were first utilised by Filip *et al.* to anal-

yse experimental results on adamantane, however, the principle was not established [83]. At the same time as Zorin *et al.* [82] established the root-sum-square coupling Schmedt auf der Günne employed effective couplings to analyse homonuclear $^{13}$C double-quantum dephasing experiments [84]. Recently, root-sum-square couplings were used in the analysis of $^{1}$H-$^{1}$H magnetisation exchange [85] and heteronuclear $^{15}$N-$^{17}$O dipolar couplings, where the estimated couplings were within ±20% of the calculated root-sum-square couplings [86].

Chapter 9

# Pulse Sequences

The new pulse sequence presented in this thesis combines off-magic angle spinning, spherical tensor analysis, spin-echo experiments and selective pulses to a rf-irradiation scheme called STARS deduced from Spherical Tensor analysis, Adjustment of the Rotation angle, and Site selectivity (Figure 9.1). In the STARS

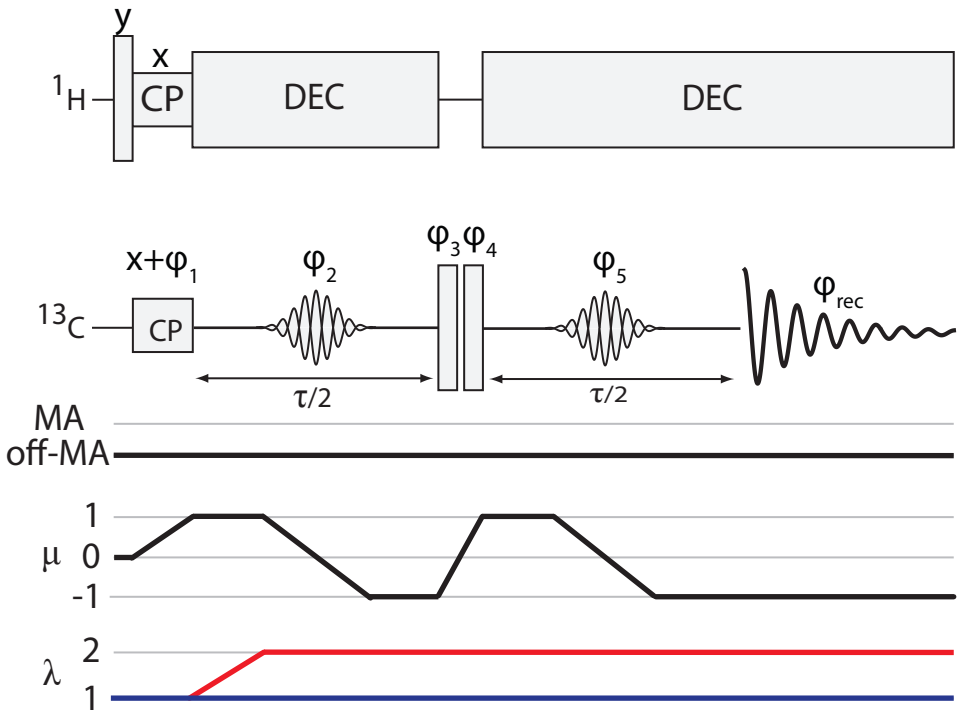


Figure 9.1: STARS pulse sequence for determining selected internuclear $^{13}$C-$^{13}$C dipolar couplings under off-magic angle spinning. The coherence order pathway ($\mu$) and tensor pathways ($\lambda$) for rank-1 (blue) and rank-2 (red) are sketched below the pulse sequence.

experiment a standard cross-polarisation transfers magnetisation from the proton to the carbon spins and is followed by two selective spin-echo sequences bracketing two strong $\pi/2$-pulses. Each selective spin-echo block of a rotor synchronised duration $\tau/2$ consists of a soft $\pi$-pulse bracketed by two variable evolution intervals. The soft pulse is implemented as an unmodulated Gaussian shape described by:

$$\omega_{nut}(t) = \omega_{nut}(t_0)\exp\left[-\alpha(t-t_0)^2\right] \tag{9.1}$$

if a single site is inverted, while the inversion of two different sites requires a dual-band selective pulse. Such a pulse is implemented as cosine-modulated Gaussian shape:

$$\omega_{nut}(t) = \omega_{nut}(t_0)\cos[\omega_m(t-t_0)]\exp\left[-\alpha(t-t_0)^2\right]. \tag{9.2}$$

The time $t_0$ is defined as the middle of the selective pulse where the amplitude is at its maximum and $\alpha$ is the Gaussian decay parameter. Strong heteronuclear coupling is employed during evolution and selective pulses.

The STA procedure is implemented by performing the pulse sequence illustrated in Figure 9.1 with the phases given for a collection of $N = 12$ Euler angle sets (Table 9.1) or for a collection of $N = 3$ Euler angle sets (Table 9.2). The Euler angle set with $N = 12$ allows to determine pure spherical signal components up to including $\lambda_{max} = 5$, whereas the $N = 3$ Euler angle set has a maximum resolution of $\lambda_{max} = 3$.

The collection of $N = 12$ Euler angle sets is derived from the vertices of an icosahedron [79] and phases are calculated as shown in Figure 8.2. Data for all twelve phase sets are stored separately and combined afterwards using Equation 8.23 with the Euler angles and weights from Table 9.1, this results in experimental rank-1 and rank-2 spherical signal components. Additional to the twelve STA experiments a 16-step phase cycle is applied on top of both $\pi$-pulses; it selects the coherence order pathway shown in Figure 9.1 and suppresses spurious signal components generated by non-ideal pulse performance.

A smaller collection of only $N = 3$ Euler angle sets with similar selection properties as for twelve angle sets was derived by Tayler *et al.* [80] and is given, along with the corresponding phases, in Table 9.2. On top of the STA-phases an eight

Table 9.1: Explicit Euler angle sets $\Omega_i = \{\alpha_i, \beta_i, \gamma_i\}$ (in degree) and rf-phases $\{\phi_{1,i}, \phi_{2,i}, \phi_{3,i}, \phi_{4,i}, \phi_{5,i}\}$ for the selection of spherical tensors of rank-1 and rank-2. The angle sets are derived from the vertices of an icosahedron [79] and phase are derived as shown in Figure 9.1.

| j | $\alpha_i$ | $\beta_i$ | $\gamma_i$ | $\omega_i$ | $\phi_{1,i}$ | $\phi_{2,i}$ | $\phi_{3,i}$ | $\phi_{4,i}$ | $\phi_{5,i}$ |
|---|---|---|---|---|---|---|---|---|---|
| 0 | 0.0 | 0.0 | 0.0 | $\frac{1}{12}$ | 0.0 | 0.0 | 0.0 | 180.0 | 0.0 |
| 1 | 0.0 | 63.4 | 144.0 | $\frac{1}{12}$ | 297.4 | 297.4 | 63.4 | 180.0 | 0.0 |
| 2 | 0.0 | 63.4 | -72.0 | $\frac{1}{12}$ | 351.4 | 351.4 | 63.4 | 180.0 | 0.0 |
| 3 | 0.0 | 63.4 | 0.0 | $\frac{1}{12}$ | 63.4 | 63.4 | 63.4 | 180.0 | 0.0 |
| 4 | 0.0 | 63.4 | 72.0 | $\frac{1}{12}$ | 135.4 | 135.4 | 63.4 | 180.0 | 0.0 |
| 5 | 0.0 | 63.4 | 144.0 | $\frac{1}{12}$ | 207.4 | 207.4 | 63.4 | 180.0 | 0.0 |
| 6 | 0.0 | 116.7 | -108.0 | $\frac{1}{12}$ | 8.7 | 8.7 | 116.7 | 180.0 | 0.0 |
| 7 | 0.0 | 116.7 | -36.0 | $\frac{1}{12}$ | 80.7 | 80.7 | 116.7 | 180.0 | 0.0 |
| 8 | 0.0 | 116.7 | 36.0 | $\frac{1}{12}$ | 152.7 | 152.7 | 116.7 | 180.0 | 0.0 |
| 9 | 0.0 | 116.7 | 108.0 | $\frac{1}{12}$ | 224.7 | 224.7 | 116.7 | 180.0 | 0.0 |
| 10 | 0.0 | 116.7 | 180.0 | $\frac{1}{12}$ | 296.7 | 296.7 | 116.7 | 180.0 | 0.0 |
| 11 | 0.0 | 180.0 | 0.0 | $\frac{1}{12}$ | 180.0 | 180.0 | 180.0 | 180.0 | 0.0 |

step cogwheel phase-cycle with $\phi_{cw} = \{0, 45, 90, 135, 180, 225, 270, 315\}$ in degrees is applied to both $\pi$-pulses selecting the coherence order pathways depicted in Figures 9.1 and 9.3.

Table 9.2: Explicit Euler angle sets $\Omega_i = \{\alpha_i, \beta_i, \gamma_i\}$ and rf-phases $\{\phi_{1,i}, \phi_{2,i}, \phi_{3,i}, \phi_{4,i}, \phi_{5,i}\}$ for the selection of spherical tensors of rank-1 and rank-2. The angles were derived by Tayler *et al.* [80]. The phases correspond to those shown in Figure 9.1 and 9.3. All angles are given in degrees.

| j | $\alpha_i$ | $\beta_i$ | $\gamma_i$ | $\omega_i$ | $\phi_{1,i}$ | $\phi_{2,i}$ | $\phi_{3,i}$ | $\phi_{4,i}$ | $\phi_{5,i}$ |
|---|---|---|---|---|---|---|---|---|---|
| 0 | 0.0 | 39.2 | 0.0 | $\frac{5}{18}$ | 39.2 | 39.2 | 39.2 | 180.0 | 0.0 |
| 1 | 0.0 | 90.0 | 0.0 | $\frac{8}{18}$ | 90.0 | 90.0 | 90.0 | 180.0 | 0.0 |
| 2 | 0.0 | 140.8 | 0.0 | $\frac{5}{18}$ | 140.8 | 140.8 | 140.8 | 180.0 | 0.0 |

The STARS-sequence has a remarkable resemblance with the homonuclear refocussed INADEQUATE experiment [87; 88]. The pulse-sequence and the coherence order pathway excited during the refocussed INADEQUATE experiment are depicted in Figure 9.2. The refocussed INADEQUATE experiment starts of by exciting transverse magnetisation employing cross-polarisation. During the adjacent spin-echo sequence S-spins evolve for a duration $2\tau$ under the isotropic homonuclear J-coupling. This is different from the STARS experiment where evolution takes places not only under the J-coupling but also under the dipolar couplings. This is due to the implementation of the STARS sequence off-magic angle which recouples the dipolar couplings that are averaged to zero under magic-angle spinning. In the presented implementation of the STARS sequence the inversion pulse is selective rather than broadband and thus only certain selected couplings evolve. This is different in the refocussed INADEQUATE experiment in which all couplings evolve. The first spin-echo sequence is followed by a $\pi/2$-pulse which creates double-quantum coherence that is converted back into single quantum coherence by a second $\pi/2$-pulse. Consequently, magnetisation in the refocussed INADEQUATE goes through irreducible spherical tensors $T^{jk}_{2\pm2}$. Contrary, in the STARS experiment magnetisation passes through irreducible spherical tensors $T^{jk}_{11}$ and $T^{jk}_{21}$ depending on the chosen pathway. During the second spin-echo the anti-phase component is reconverted into an in-phase signal for detection.

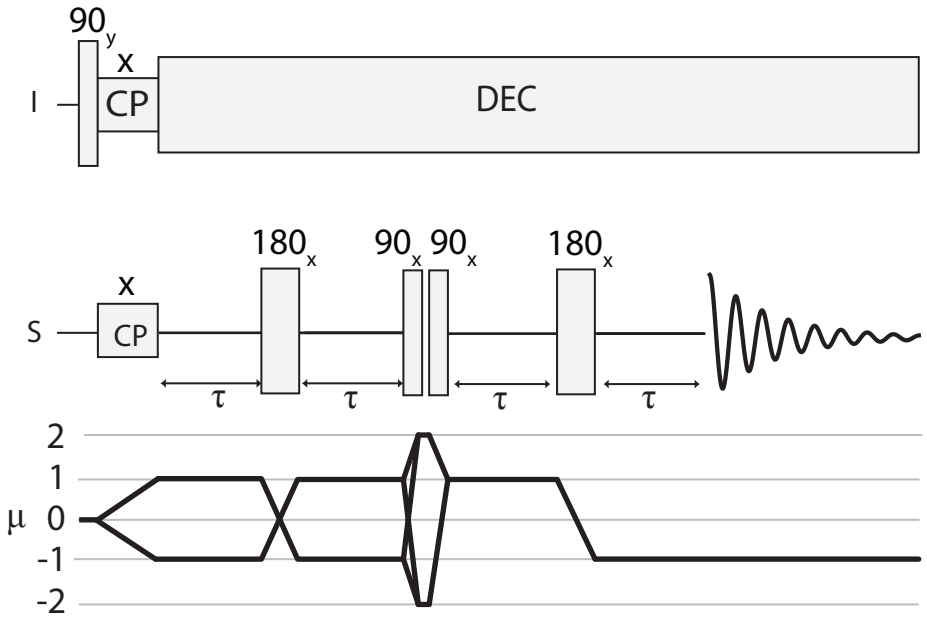


Figure 9.2: The refocussed INADEQUATE pulse sequence for determining homonuclear through-bond couplings is shown. The coherence order pathway ($\mu$) is given below the sequence.

The main differences between the STARS experiment and the refocussed INADEQUATE experiment are the underlying mechanisms for magnetisation transfer and the irreducible spherical tensors through which the signal passes. STARS transfers magnetisation via residual dipolar couplings introduced by off-magic angle spinning, since dipolar couplings are absent during the refocussed INADEQUATE experiment magnetisation transfer relies on the J-coupling. The STARS experiment allows the determination of through space distances in the structurally interesting range of > 4Å whereas those long range distances can not be determined by the trough-bond measurements in the refocussed INADEQUATE experiment. However, through-bond couplings have the advantage of being orientation independent.

The STARS-experiment discussed above loses resolution and sensitivity due to acquisition off the magic angle. This is overcome employing a switched-angle spinning version of STARS technique referred to as SA-STARS (Figure 9.3). In the SA-STARS experiment a standard proton-carbon cross-polarisation is followed by two selective spin-echo sequences bracketing two strong $\pi/2$-pulses. Each selective spin-echo block has a rotor synchronised duration of $\tau/2$ and consists of a soft $\pi$-pulse bracketed by two variable evolution intervals. The choice of the soft pulse is identical to the STARS experiment. Adjacent the last spin-echo

interval magnetisation is stored along $B_0$ by a strong $\pi/2$-pulse, followed by a z-filter during which the rotor angle is mechanically switched to the magic-angle. As soon as the angle is settled a strong readout $\pi/2$-pulse is applied and the signal is acquired, stored and processed. Strong heteronuclear coupling is employed during evolution, selective pulses and the z-filter.

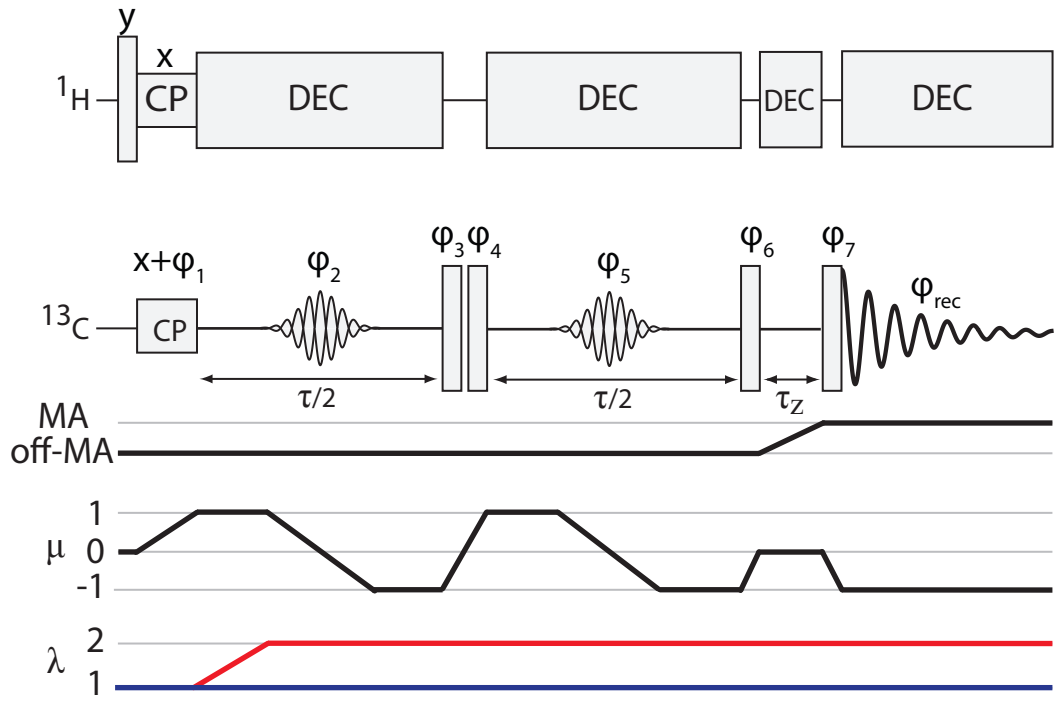


Figure 9.3: SA-STARS pulse sequence for determining selected internuclear $^{13}$C-$^{13}$C dipolar couplings. The dipolar couplings evolve off-magic angle, while the NMR signal is acquired on the magic angle. The rotor-angle at each point in the pulse sequence is shown below. The coherence order pathway ($\mu$) and tensor pathways ($\lambda$) for rank-1 (blue) and rank-2 (red) are given.

The combination of pulse sequences and Euler angle sets results in a rather cumbersome description and, thus, they will be referred to as STARS-N and SA-STARS-N where in refers to the collection of Euler angle sets. Experiments were conducted using STARS-12, STARS-3 and SA-STARS-3.

To assure that the Gaussian pulses are selective they are calibrated off-magic angle and optimised to yield an inversion efficiency of 70-80%. The spinning angle is chosen such that the recoupled peaks never overlap and it is possible to selectively invert only the desired spins.

Chapter 10

# Analytical Expressions

Analytical expressions for the magnetisation build-up of the rank-1 and rank-2 components in the STARS (Figure 9.1) and SA-STARS (Figure 9.3) experiment are derived in this chapter, considering two different forms of the free evolution Hamiltonian. First the full form of the Hamiltonian, $H^f_{jk}$, including the $T_{20}$-form of the dipolar Hamiltonian, and second the truncated or zz-form of the Hamiltonian, $H^t_{jk}$. The full Hamiltonian is valid if the CSA tensors of the two sites are identical or co-linear, while in all other cases magnetisation evolves under the truncated Hamiltonian.

## 10.1. Full Evolution Hamiltonian

The full evolution Hamiltonian, $H^f_{jk}$, for two spins $S_j$ and $S_k$ is written as:

$$\begin{aligned} H^f_{jk} &= \omega_j S_{jz} + \omega_k S_{kz} + 2\pi J_{jk}\,\mathbf{S}_j\mathbf{S}_k + \sqrt{6}\,T^{jk}_{20} \\ &= \omega_j S_{jz} + \omega_k S_{kz} + \omega_{jk}\,2S_{jz}S_{kz} - \omega^{\pm}_{jk}\frac{1}{2}\left(S^+_j S^-_k + S^-_j S^+_k\right) \end{aligned} \tag{10.1}$$

with the two coupling terms $\omega_{jk}$ and $\omega^{\pm}_{jk}$:

$$\omega_{jk} = \pi J_{jk} + d \tag{10.2}$$

$$\omega^{\pm}_{jk} = 2\pi J_{jk} - d. \tag{10.3}$$

Here, $d$ is the secular component of the through space dipolar coupling and $J$ is the J-coupling in Hz. Sample spinning introduces a time dependence into the

chemical shift frequencies $\omega_j$ and $\omega_k$ as well as into the secular dipolar coupling $d$. Those time dependent terms are expressed as a Fourier series:

$$\omega_Q = \sum_{m-2}^{2} \omega_Q^{(m)} \exp\{im\omega_r t\} \tag{10.4}$$

where $Q$ refers to any of the indices $jk, jk^{\pm}, j$ and $k$, and $\omega_r$ is the spinning frequency. The zero-order Fourier components under exact magic-angle spinning are given by:

$$\left.\begin{array}{l} \omega_j^{(0)} = \omega_j^{iso} \\ \omega_k^{(0)} = \omega_k^{iso} \\ \omega_{jk}^{(0)} = \pi J \\ \omega_{jk}^{\pm(0)} = \pi J \end{array}\right\} \text{exact MAS}$$

However, under off-magic angle spinning the zero-order Fourier components are different due to the incomplete averaging of the anisotropic interactions. The off-magic-angle zero-order Fourier components $\omega_{jk}$ and $\omega_{jk}^{\pm}$ are given by:

$$\omega_{jk}^{(0)} = \pi J + b_{jk}\, d_{00}^2\left[\beta_{PR}\right] d_{00}^2\left[\beta_{RL}\right] \tag{10.5}$$

$$\omega_{jk}^{\pm(0)} = \pi J - \frac{1}{2} b_{jk}\, d_{00}^2\left[\beta_{PR}\right] d_{00}^2\left[\beta_{RL}\right] \tag{10.6}$$

with the dipolar coupling constant $b_{jk}$ (Equation 4.44). The term $d_{00}^2\left[\beta_Q\right]$ is an element of the second-rank reduced Wigner matrix and $\beta_Q$ refers to $\beta_{PR}$ and $\beta_{RL}$. $\beta_{PR}$ is the angle between the internuclear vector and and the rotor axis and $\beta_{PR}$ is the angle between the rotor axis and the static magnetic field. In a powder sample the angle $\beta_{PR}$ is random.

The evolution of the full Hamiltonian $H_{jk}^f$ (Equation 10.1) under the STARS sequence is obtained by calculating the corresponding Liouville space bracket:

$$\sigma_{11-1} = \left(I^- \left|\hat{U}\left(\frac{\tau}{2}\right)\right| T_{11}^{jk}\right)\left(T_{1-1}^{jk} \left|\hat{U}\left(\frac{\tau}{2}\right)\right| \rho_0\right) \tag{10.7}$$

which yields the following analytical expression for the rank-1 ($T_{1\pm1}$ in Equation 7.11) powder average:

$$\begin{aligned} \sigma_{11-1}^f &= \frac{1}{2}\int_0^{\pi} \cos\left[\frac{3}{4} b_{jk}\, d_{00}^2\left[\beta_{PR}\right] d_{00}^2\left[\beta_{RL}\right](\tau - 2\cdot\tau_{sh})\right]^2 \sin\left[\beta_{PR}\right] d\beta_{PR} \\ &= \frac{1}{2} + \frac{1}{2x_f}\left(\cos\left[\theta_f\right] Fc\left[x_f\right] + Fs\left[x_f\right]\sin\left[\theta_f\right]\right). \end{aligned} \tag{10.8}$$

The Liouville space bracket has an initial density operator of $\rho_0 = T_{11}^j + T_{11}^k$ and the commutation superoperator is $\hat{U} = e^{-i\frac{\tau}{2}\hat{H}}$. $\hat{H}$ is the commutation superoperator with the evolution Hamiltonian.

Under the same conditions as for rank-1 the Liouville space bracket for rank-2 ($T_{2\pm1}$ in Equation 7.11) can be calculated:

$$\sigma_{21-1} = \left(I^- \left|\hat{U}\left(\frac{\tau}{2}\right)\right| T_{21}^{jk}\right)\left(T_{2-1}^{jk} \left|\hat{U}\left(\frac{\tau}{2}\right)\right| \rho_0\right) \tag{10.9}$$

resulting in the analytical expression for the rank-2 powder average:

$$\begin{aligned}\sigma_{21-1}^f &= \frac{1}{2}\int_0^{\pi} -\sin\left[\frac{3}{4} b_{jk}\, d_{00}^2\left[\beta_{PR}\right] d_{00}^2\left[\beta_{RL}\right](\tau - 2\cdot\tau_{sh})\right]^2 \sin\left[\beta_{PR}\right] d\beta_{PR} \\ &= -\frac{1}{2} + \frac{1}{2x_f}\left(\cos\left[\theta_f\right] Fc\left[x_f\right] + Fs\left[x_f\right]\sin\left[\theta_f\right]\right).\end{aligned} \tag{10.10}$$

The terms $x_f$ and $\theta_f$ are given by:

$$x_f = \frac{3}{\sqrt{2\pi}}\sqrt{b_{jk}\, d_{00}^2\left[\beta_{RL}\right](\tau - 2\cdot\tau_{sh})} \tag{10.11}$$

and

$$\theta_f = \frac{3}{4} b_{jk}\, d_{00}^2\left[\beta_{RL}\right](\tau - 2\cdot\tau_{sh}). \tag{10.12}$$

The parameter $\tau_{sh}$ is a correction factor which takes the spin-evolution during the Gaussian pulse into account and can be calculated from the shape of the pulse [89].

The Fresnel integrals are defined as follows:

$$Fc(x) = \int_0^x \cos\left[\frac{\pi y^2}{2}\right] \mathrm{d}y \tag{10.13}$$

and

$$Fs(x) = \int_0^x \sin\left[\frac{\pi y^2}{2}\right] \mathrm{d}y. \tag{10.14}$$

Experimental results will be fitted to the ratio of the rank-2 and rank-1 powder average ($\phi^f$):

$$\phi^f = \frac{\sigma_{21-1}^f}{\sigma_{11-1}^f} \tag{10.15}$$

No evolution of the J-coupling was observed under the full dipolar Hamiltonian, this effect is caused be the flip-flop terms which cancel the contributions between from the secular term.

The analytical powder average for the rank-1 ($\sigma^{f}_{11-1}$) and rank-2 ($\sigma^{f}_{21-1}$) component assumes an isolated spin-pair. Thus, if effective couplings are considered the assumption of a nearly isolated spin-pair does not hold and an approximate analytical form for rank-1 ($\sigma^{fse}_{11-1}$) and rank-2 ($\sigma^{fse}_{21-1}$) is derived by the series expansion of Equations 10.8 and 10.10, respectively.

$$\sigma^{fse}_{11-1} = 1 - \frac{9}{80}\left(b_{rss,j}\right)^2 \left(d^2_{00}\left[\beta_{RL}\right]\right)^2 (\tau - 2\cdot\tau_{sh})^2 \tag{10.16}$$

$$\sigma^{fse}_{21-1} = -\frac{9}{80}\left(b_{rss,j}\right)^2 \left(d^2_{00}\left[\beta_{RL}\right]\right)^2 (\tau - 2\cdot\tau_{sh})^2 \tag{10.17}$$

The ratio of the rank-2 and rank-1 series expansion is denoted $\phi^{fse}$ and takes the form:

$$\phi^{fse} = \frac{\sigma^{fse}_{21-1}}{\sigma^{fse}_{11-1}}. \tag{10.18}$$

A series expansion of the ratio in Equation 10.15 takes the same form as Equation 10.16.

## 10.2. Truncated Evolution Hamiltonian

The truncated evolution Hamiltonian, $H^{f}_{jk}$, for two spins $S_j$ and $S_k$ is written as:

$$H_{jk} = \omega_j S_{jz} + \omega_k S_{kz} + \omega_{jk} S_{jz} S_{kz} \tag{10.19}$$

using $\omega_{jk}$ as defined in in Equation 10.2.

The evolution of the truncated Hamiltonian $H^{t}_{jk}$ (Equation 10.19) under the STARS sequence yields the following analytical expression for the rank-1 powder average:

$$\begin{aligned}\sigma^{t}_{11-1} &= \frac{1}{2}\int_0^{\pi} \cos\left[\frac{1}{2}\left(b_{jk}\, d^2_{00}\left[\beta_{PR}\right] d^2_{00}\left[\beta_{RL}\right] + \pi J\right)(\tau - 2\cdot\tau_{sh})\right]^2 \sin\left[\beta_{PR}\right] d\beta_{PR} \\ &= \frac{1}{2} + \frac{1}{2x_t}\left(\cos[\theta_t] Fc[x_t] + Fs[x_t]\sin[\theta_t]\right)\end{aligned} \tag{10.20}$$

while the rank-2 powder average under equivalent conditions yields:

$$\sigma^t_{21-1} = \frac{1}{2}\int_0^{\pi} -\sin\left[\frac{1}{2}\left(b_{jk}\, d^2_{00}(\beta_{PR})\, d^2_{00}(\beta_{RL}) + \pi J\right)(\tau - 2\cdot\tau_{sh})\right]^2 \sin\left[\beta_{PR}\right] d\beta_{PR}$$
$$= -\frac{1}{2} + \frac{1}{2x_t}\left(\cos[\theta_t]\, Fc[x_t] + Fs[x_t]\sin[\theta_t]\right). \tag{10.21}$$

The terms $x_t$ and $\theta_t$ are given by:

$$x_t = \sqrt{\frac{3}{\pi} b_{jk}\, d^2_{00}\left[\beta_{RL}\right](\tau - 2\cdot\tau_{sh})} \tag{10.22}$$

and

$$\theta_t = \frac{1}{2}\left(b_{jk}\, d^2_{00}\left[\beta_{RL}\right] - 2J\pi\right)(\tau - 2\cdot\tau_{sh}) \tag{10.23}$$

and the Fresnel functions are defined as in Equations 10.13 and 10.14. Equivalent to the full Hamiltonian description the truncated powder-average-ratio, $\phi^t$, of the truncated rank-1 and rank-2 component is defined as:

$$\phi^t = \frac{\sigma^t_{21-1}}{\sigma^t_{11-1}}. \tag{10.24}$$

As for the full Hamiltonian, the analytical powder average for the rank-1 ($\sigma^t_{11-1}$) and rank-2 ($\sigma^t_{21-1}$) component assumes an isolated spin-pair. The series expansion of Equations 10.20 and 10.21 leads to the approximate analytical forms $\sigma^{tse}_{11-1}$ and $\sigma^{tse}_{21-1}$:

$$\sigma^{tse}_{11-1,zz} = 1 - \frac{1}{20}\left(\left(b^2_{rss,j}\right)\left(d^2_{00}\left[\beta_{RL}\right]\right)^2 + 5J^2\pi^2\right)(\tau - 2\cdot\tau_{sh})^2 \tag{10.25}$$

and

$$\sigma^{tse}_{21-1,zz} = \frac{1}{20}\left(\left(b_{rss,j}\right)^2\left(d^2_{00}\left[\beta_{RL}\right]\right)^2 + 5J^2\pi^2\right)(\tau - 2\cdot\tau_{sh})^2 \tag{10.26}$$

their ratio:

$$\phi^{tse} = \frac{\sigma^{tse}_{21-1}}{\sigma^{tse}_{11-1}} \tag{10.27}$$

can be used to estimate effective dipolar couplings.

Chapter 11

# Numerical Simulations

Numerical simulations for the STARS experiments (Figures 9.1 and 9.3) were performed in Mathematica 7.0 using the SpinDynamics routines as provided in mPackages [90]. For all simulations the unperturbed spin Hamiltonian takes the form:

$$H_0 = H_{CS} + H_{DD} + H_J \tag{11.1}$$

where the chemical shift Hamiltonian, $H_{CS}$, for spins $S_j$ and $S_k$ is given by:

$$H_{CS}^{j} = \omega_j S_{jz} \tag{11.2}$$

and

$$H_{CS}^{k} = \omega_k S_{kz}. \tag{11.3}$$

The dipolar coupling Hamiltonian, $H_{DD}$, is given by:

$$H_{DD}^{jk} = b_{jk}\left(-\frac{1}{2}S_j^+ S_k^- - \frac{1}{2}S_j^- S_k^+ + 2S_{jz}S_{kz}\right) d_{00}^2\left[\beta_{PR}\right] d_{00}^2\left[\beta_{RL}\right] \tag{11.4}$$

and the J-coupling Hamiltonian, $H_J$, takes the form:

$$H_J^{jk} = 2\pi \mathbf{S}_j \mathbf{S}_k. \tag{11.5}$$

Spin system parameters for the numerical simulations presented are based on a sample of L-histidine hydrochloride monohydrate, whose structure and labelling scheme are shown in Figure 11.1 along with five histidine molecules in the crystal lattice of L-histidine hydrochloride monohydrate (HISTCM01, Cambridge

Structural Database). The five C$\beta$-atoms are highlighted as simulations were conducted with up to five C$\beta$-spins to investigate the reliability of the analytical formula obtained in Chapter 10 in connection with effective dipolar couplings, $b_{rss,j}$. The dominant dipolar coupling in the C$\beta$-network is -69.6 Hz, which cor-

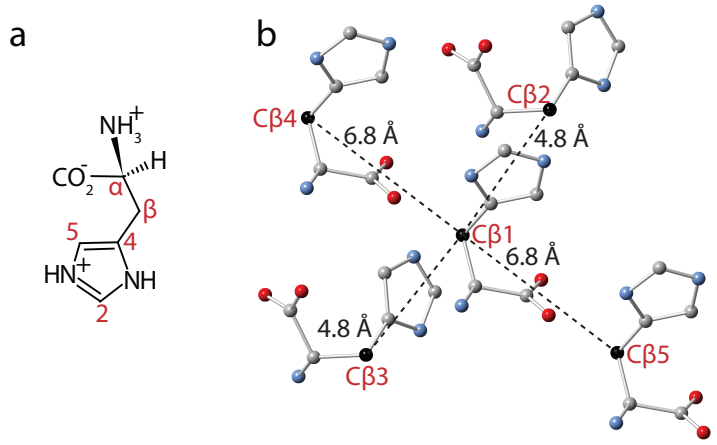


Figure 11.1: a) Structure of histidine hydrochloride monohydrate with the labelling scheme used throughout this thesis. b) C$\beta$-network in histidine hydrochloride monohydrate based on its crystal structure (HISTCM01,Cambridge Structural Database). The C$\beta$ atoms are shown in black, all other carbon atoms in grey, oxygen atoms are red and nitrogen atoms are blue. The distances of 4.8 Å and 6.8 Å correspond to dipolar coupling strength of -69.6 Hz and -23.7 Hz, respectively. The labelling C$\beta$2 and C$\beta$3 as well as C$\beta$4 and C$\beta$5 could be interchanged with each other but have been introduced in increasing order starting from C$\beta$1.

responds to an intermolecular distance of 4.8 Å. As it is visualised in Figure 11.1 there are two C$\beta$-atoms in equivalent distance to the centre C$\beta$-atom, hence, two couplings of the same strength. These two couplings cannot be separated and it is only possible to measure an effective dipolar coupling (Section 8.6.). The effective dipolar couplings for all simulated C$\beta$-spin systems are summarised in Table 11.1, corresponding effective distances, $r_{rss,j}$, are calculated to give a feeling of the distances that can be estimated using the STARS sequence, but do not correspond to a real distance in the crystal structure.

Spin system parameters for simulated C$\beta$-spin system are summarised in Tables 11.2 and 11.3. Chemical shift parameters are obtained from reference [91], CSA tensors are based on those determined for glycine-C$\alpha$ [92] and are used to calculate the Euler angles for the transformation of the CSA tensor from the principle

Table 11.1: Effective dipolar couplings between two $^{13}$C$\beta$-nuclei as they can be calculated according to Equation 8.27. They are based on distances extracted from the histidine hydrochloride monohydrate crystal structure (HISTCM01).

| number of spins | $b_{rss,j}$/Hz | $r_{rss,j}$/Å |
|---|---|---|
| 3 | -98.4 | 4.26 |
| 4 | -101.2 | 4.22 |
| 5 | -104 | 4.18 |

axis frame to the molecular frame, which has its z-axis along the $C4_1 - C5_1$ double bond.

Table 11.2: The chemical shift parameters for the C$\beta$-network include the isotropic chemical shift, $\delta_{iso}$, the anisotropic chemical shift, $\delta_{aniso}$, and the Euler angles, $\Omega_{PM} = \{\alpha_{PM}, \beta_{PM}, \gamma_{PM}\}$, for the transformation of the CSA tensor from the principle axis frame to the molecular frame.

| spin | $\delta_{iso}$/ppm | $\delta_{aniso}$/ppm | $\Omega_{PM}$/ ° |
|---|---|---|---|
| C$\beta_1$ | 26.8 | 17.0 | {152.9, 119.3, 115.7} |
| C$\beta_2$ | 26.8 | 17.0 | {-69.3, 93.4, 10.3} |
| C$\beta_3$ | 26.8 | 17.0 | {-69.3, 93.4, 10.3} |
| C$\beta_4$ | 26.8 | 17.0 | {152.9, 119.4, 115.7} |
| C$\beta_5$ | 26.8 | 17.0 | {152.9, 119.4, 115.7} |

The dipolar coupling constants in the simulated spin system and the Euler angles to transform the dipolar coupling tensor from the principle axis frame to the molecular frame are calculated from the crystal structure of histidine hydrochloride monohydrate (HISTCM01).

Table 11.3: The dipolar coupling parameters for the 5-spin C$\beta$-network include the dipolar coupling constant $b_{jk}$ for each spin-pair and the respective Euler angles, $\Omega_{PM} = \{\alpha_{PM}, \beta_{PM}, \gamma_{PM}\}$, for the transformation of the dipolar coupling tensor from the principle axis frame to the molecular frame.

| spin-pair | $b_{jk}$/Hz | $\Omega_{PM}$/ ° |
|---|---|---|
| C$\beta_1$-C$\beta_2$ | -69.6 | {-93.8, 137.0, 54.2} |
| C$\beta_1$-C$\beta_3$ | -69.6 | {60.1, 84.7, -119.5} |
| C$\beta_1$-C$\beta_4$ | -23.7 | {68.1, 109.5, -42.1} |
| C$\beta_1$-C$\beta_5$ | -23.7 | {-68.1, 70.5, 137.9} |
| C$\beta_2$-C$\beta_3$ | -10.7 | {73.0, 63.8,-122.1} |
| C$\beta_2$-C$\beta_4$ | -17.0 | {56.9, 80.8, -67.5} |
| C$\beta_2$-C$\beta_5$ | -10.4 | {-129.6, 50.1, 165.9} |
| C$\beta_3$-C$\beta_4$ | -17.0 | {9.2, 110.8, -1.5} |
| C$\beta_3$-C$\beta_5$ | -10.4 | {-63.4, 78.2, 106.1} |
| C$\beta_4$-C$\beta_5$ | -3.0 | {-68.1, 70.5, 137.9} |

With the above spin system parameters simulations were carried out at a Larmor frequency of $\omega_0/2\pi$ = 100.541 MHz, a spinning speed of $\omega_r/2\pi$ = 13.100 kHz and a rotor angle of $\beta_{RL} = 51.74°$. Selective inversion was accomplished by a single Gaussian irradiating at the C$\beta$-frequency, it had a width of $\Delta_G$ = 2600 Hz and a decay parameter $\alpha = 1.69 \cdot 10^6 \mathrm{s}^{-2}$. The STARS-3 sequence was implemented for simulations utilising the Euler angle sets in Table 9.2. Simulations started with magnetisation on all spins, but only C$\beta_1$ was observed.

The results of the numerical simulations for a 2-spin, 3-spin, 4-spin and 5-spin system are shown in Figure 11.2 and compared to the analytical formulae obtained with the truncated Hamiltonian ($\phi^t$ and $\phi^{tse}$). Simulations of the isolated 2-spin system indicate a better agreement with the theoretical curve $\phi^{tse}$ than with $\phi^t$, even though this is the case in which $\phi^t$ is valid. This discrepancy can be quantified by fitting the numerical data points to both truncated ana-

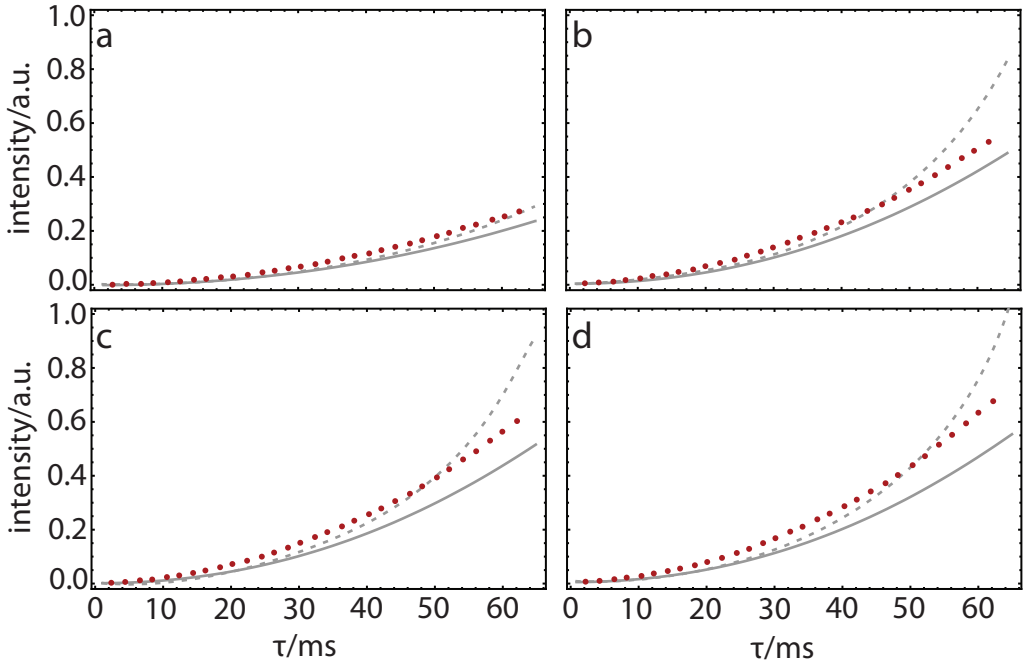


Figure 11.2: Numerical simulations for C$\beta$-spin systems of different size are shown (red dots) along with the analytical ratios for the truncated Hamiltonian. The solid grey line corresponds to the powder average (Equation 10.24) and the dashed grey line to the series expansion (Equation 10.27). The analytical expressions are derived using the dipolar coupling or effective dipolar coupling as calculated from the X-ray structure for the respective spin system. a) 2-spin system ($b_{jk}/2\pi = -69.6$ Hz), b) 3-spin system ($b_{rss,j}/2\pi = -98.4$ Hz), c) 4-spin system ($b_{rss,j}/2\pi = -101.2$ Hz) and d) 5-spin system ($b_{rss,j}/2\pi = -104$ Hz).

lytical expressions. A dipolar coupling of -78.2±0.4 Hz — 8.6 Hz stronger than the calculated value — is estimated for $\phi^t$, while $\phi^{tse}$ yields a dipolar coupling of -72.3±0.8 Hz which is only 2.7 Hz stronger than the calculated coupling of -69.6 Hz. In both cases the estimated dipolar coupling is stronger than the calculated value. Additional simulations indicate that the small anisotropic chemical shift of 17 ppm for the C$\beta$-sites causes the discrepancy between numerical simulation and analytical data points. Thus, the stronger coupling that is estimated arises from a Hamiltonian which is a mix between the full $T_{20}$ Hamiltonian and the truncated Hamiltonian. Further work is under way to include this observation into data analysis.

In cases of the 3-spin, 4-spin and 5-spin system, in which the series expansion, $\phi^{tse}$, of the analytical formula is valid, again a better agreement of the numerical results with $\phi^{tse}$ is observed, especially at evolution times smaller than 50 ms. At evolution times above 50 ms a steep increase in the analytical formula is ob-

served, which does not match the numerical results. Fits of the numerical data obtained for multiple-spin systems with $\phi^{tse}$ yield dipolar couplings which are 5 Hz weaker than those calculated; up to 16 Hz stronger couplings are estimated for those systems with $\phi^{t}$. Summarising the results in terms of structurally interesting distances one estimates distances that are ~0.2 Å shorter by fitting with $\phi^{t}$, while distances estimated employing $\phi^{tse}$ are less than 0.1 Å longer. The discrepancies observed might result from the different tensor orientations of the various spins. Fitting the numerical simulations to weighted analytical formulae, $\frac{2}{3}\phi^{t} + \frac{1}{3}\phi^{p}$ for a 4-spin system and $\frac{1}{2}\phi^{t} + \frac{1}{2}\phi^{p}$ for a 5-spin system, couplings which are 5–10 Hz weaker than the calculated effective coupling are obtained. Currently further studies are under way to reliably incorporate the different tensor orientations into the analytical expressions.

The robustness of the effective coupling as experimental accessible parameter is investigated by 3-spin simulations, in which the angle $\theta$ between spin C$\beta_1$, C$\beta_2$, and C$\beta_3$ is altered (Figure 11.3.a). It is apparent that the dipolar coupling

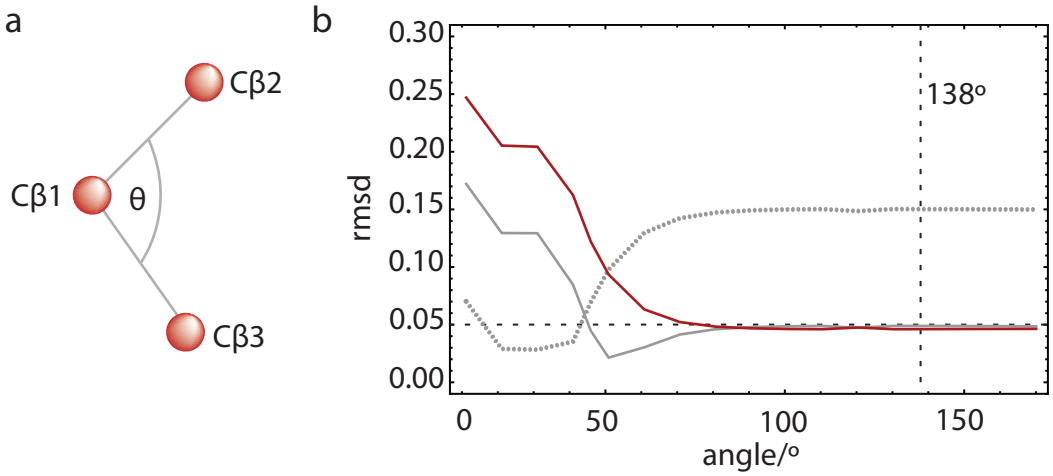


Figure 11.3: a) Illustration of the varied angle $\theta$ in a C$\beta$-3-spin system. b) Numerical simulations for C$\beta$-3-spin systems with different angles $\theta$ were conducted. The rmsd between the data points and $\phi^{t}$ with $b_{jk}/2\pi = -69.6$ Hz is plotted as dotted grey line, the rmsd between data points and $\phi^{t}$ with $b_{jk}/2\pi = -98.4$ Hz is plotted as solid grey line and the rmsd between data points and $\phi^{tse}$ with $b_{jk}/2\pi = -98.4$ Hz is plotted as solid red line. The dashed line at 138°emphasizes the rmsd for the realistic 3-spin system as it is shown in Figure 11.2.b).

of the 2-spin system ($b_{jk}/2\pi = -69.6$ Hz) is not the accessible distance, if C$\beta_1$ is coupled to two spins with equivalent coupling strength. A comparison between $\phi^{t}$ and $\phi^{tse}$ with the calculated effective dipolar coupling of -98.4 Hz shows that

both analytical expressions converge to an rmsd of 0.05 if $\theta$ is larger than 80°. At $\theta$ = 80° the dipolar coupling between C$\beta_2$ and C$\beta_3$ is -32.75 Hz and thereby weaker than the the couplings with C$\beta_1$. This is, however, not true for $\theta$ < 60° where the C$\beta_2$-C$\beta_3$ coupling exceeds the dipolar couplings with C$\beta_1$ and thus the calculated effective coupling is no longer valid. It cannot be predicted from the rmsd whether $\phi^t$ or $\phi^{tse}$ is in better agreement with the calculated dipolar coupling. However, fitting to the numerical results with $\phi^t$ and $\phi^{tse}$ have previously demonstrated that $\phi^{tse}$ allows a more accurate estimation of the effective dipolar coupling.

All simulations show have been conducted with a realistic Gaussian pulse, keeping the parameters for the Gaussian pulse within experimental realistic limits. For such a set-up no differences have been observed compared to the implementation with an ideal selective pulse.

Chapter 12

# Experimental Details

All experiments were performed on a 9.4 T Varian Infinity plus NMR spectrometer using a 3 mm DOTY switched-angle probe in double resonance mode. The probe is equipped with a servo-controller motor which connects to the stator by two belts. The motor itself is connected to a controller which is operated by a computer with a graphical interface to set a fixed rotor angle in the range $\pm 20°$with respect to the magic angle. Furthermore, it is possible to program a list of angles between which the controller switches if the spectrometer sends a signal (TTL pulse). This implies that the controller is connected to the spectrometer which can send signals to the controller. The signal can be directly programmed into a desired pulse program allowing accurate timing of the angle switch. After each switch a so called settling-time is needed for the angle to stabilise. For angle offsets of up to $5°$a settling time of 2 ms proofed to be sufficient, however, for larger switches longer times a expected. The manufacture suggests a settling time of 60 ms.

Additional to the mechanical switching of the rotation angle the probe is equipped with a Hall-effect device, which allows an independent measure of the rotation angle [93].If the Hall device is mounted parallel to the magnetic field it becomes sensitive to the rotation angle and if mounted perfectly no voltage is measured at the magic angle. However, this is never the case and thus it is necessary to calibrate the device. This is done by recording a spin-echo modulation curve of U-[$^{13}$C]-$\alpha$-glycine at different positions of the belt [60]. The spin-echo curves can then be fitted to determine the exact spinning-angle. A calibration curve of spinning-angle vs. Hall voltage can be determined and the Hall voltage at

the magic angle determined. The magic-angle is now set according to the Hall voltage. This has to be done only once and afterwards the controller remembers the position of the magic angle. As an additional control over the angle the Hall voltage is monitored throughout the sequence to detect any instabilities in the angle.

Currently the 3 mm DOTY switched-angle probe is not interfaced to the spinning controller due to different manufactures. Therefore, the spinning speed is set but not controlled during the experiments resulting in the relatively large drift reported below.

Processing for the STARS and SA-STARS experiments, as explained in Section 8.5., were carried out using home written routines in Mathematica 7.0, which was also used for data analysis.

## 12.1. Experiments on an Isolated Spin-Pair

A sample of 1-[$^{13}$C]-$\alpha$-glycine, whose polymorph was confirmed by X-ray powder diffraction, was purchased from Cambridge Isotope Laboratories, Inc. and used as a model compound containing an isolated spin-pair. Experiments were conducted utilising the STARS-12 pulse sequence[1] at a rotor angle of 52.74°, -2°off-magic-angle, while spinning at 11.92 ± 0.02 kHz. Proton and carbon $\pi/2$-pulses were implemented with a duration of 2.4 $\mu s$ and 2.7 $\mu s$, respectively. During a cross-polarisation of 4 ms spin-lock fields of $\omega_{rf}^{1H}/2\pi$ = 50 kHz and $\omega_{rf}^{13C}/2\pi$ = 37 kHz were applied. SPINAL-64 was implemented as a heteronuclear recoupling sequence with a nutation frequency of $\omega_{dec}^{1H}/2\pi$ = 95 kHz and a pulse duration of 4.8 $\mu s$. The single site selective Gaussian pulse is given by a frequency width of $\Delta_G$ = 2500 Hz, a decay parameter $\alpha = 11.63 \cdot 10^6 s^{-2}$, a Gaussian time shift $\tau_{sh}$ = 0.30 ms and a truncation level of 1%. Using a recycle delay of 7 s 16 transients were added for each experiment.

[1] All experiments conducted with the STARS-12 pulse sequence were recorded by Pierre Thureau.

## 12.2. Multiple-Spin System Experiments on Histidine Hydrochloride Monohydrate

All experiments described in this Section were performed on a sample of U-[$^{13}$C-$^{15}$N]-L-histidine·HCl·$H_2O$ purchased from Cambridge Isotope Laboratories, Inc. and data were acquired at ambient temperatures.

### Experimental details: C2-C5 dipolar coupling estimation

Experiments to estimate the intramolecular C2-C5 dipolar coupling in histidine hydrochloride monohydrate were conducted using the STARS-12 pulse sequence (Figure 9.1), thus utilising the isosahedral phase cycle introduced in Table 9.1. The sample was spun at a rotation angle of 53.94 ± 0.05°— -0.80 °off-magic angle — employing a spinning speed of 13.93 ± 0.07 kHz. The duration of the proton and carbon $\pi/2$-pulses were 2.2 $\mu$s and 2.55 $\mu$s, respectively. Magnetisation was transferred for 0.7 ms during a CP with $\omega_{rf}^{1H}/2\pi$ = 54 kHz and $\omega_{rf}^{13C}/2\pi$ = 40 kHz. Heteronuclear decoupling at $\omega_{dec}^{1H}/2\pi$ = 90 kHz was implemented with swTPPM. The C2 and C5 site were selected by a dual-band selective cosine modulated Gaussian pulse with a Gaussian frequency width $\Delta_G$ = 650 Hz, a decay parameter $\alpha = 0.901 \cdot 10^6 s^{-2}$, a Gaussian time shift $\tau_{sh}$ = 1.09 ms and a truncation level of 1%. 16 transients were added for each experiment and the recycle delay was set to 7 s.

### Experimental details: CO-C5 dipolar coupling estimation

The intramolecular CO-C5 dipolar coupling was determined with the STARS-12 pulse sequence (Figure 9.1). Sample spinning was set to 14.03 ± 0.03 kHz at a rotation angle of 53.24 ± 0.05°, thus a magic-angle offset of -1.5°. Proton and carbon $\pi/2$-pulses lasted 2.55 $\mu$, while a contact time of 0.7 ms with $\omega_{rf}^{1H}/2\pi$ = 54 kHz and $\omega_{rf}^{13C}/2\pi$ = 40 kHz was set for the CP. Heteronuclear decoupling at $\omega_{dec}^{1H}/2\pi$ = 92 kHz was implemented using SPINAL-64. Selection of the CO and C5 site was accomplished using a dual-band selective cosine modulated Gaussian pulse employing a Gaussian frequency width $\Delta_G$ = 950 Hz, a decay parameter $\alpha = 1.791 \cdot 10^6 s^{-2}$, a Gaussian time shift $\tau_{sh}$ = 0.77 ms and a truncation level of 1%. The recycle delay was 8 s and 16 transients were added for each experiment.

**Experimental details: C$\beta$-C$\beta$ dipolar coupling estimation**

The STARS-3 sequence (Figure 9.1), thus employing the collection of three Euler angle sets (Table 9.2) and an 8-step cogwheel-phasecycle (Chapter 9), was used to estimate the intermolecular C$\beta$-C$\beta$ dipolar coupling. Here, the sample was spun at 13.00±0.02 kHz around a rotation angle of 51.74 ± 0.05°. This is a magic-angle offset of -3°. A duration of 2.5 $\mu$s was calibrated for the proton $\pi$/2-pulse, while the carbon $\pi$/2-pulse duration was 3 $\mu$s. Cross-polarisation was implemented with a contact time of 1.25 ms, and nutation frequencies of $\omega_{rf}^{1H}/2\pi$ = 48 kHz and $\omega_{rf}^{13C}/2\pi$ = 43 kHz. SPINAL-64 at $\omega_{dec}^{1H}/2\pi$ = 83 kHz and with a pulse duration of 4.2 $\mu$s was used for heteronuclear decoupling. A single-band frequency selective Gaussian pulse with $\Delta_G$ = 1000 Hz, a decay parameter $\alpha = 2.467 \cdot 10^6 s^{-2}$ and a Gaussian time shift of $\tau_{sh}$ = 0.66 ms was applied to selectively invert the C$\beta$-site. The truncation level for the Gaussian was 1%. Using a recycle delay of 8 s each experiments was acquired with 128 transients.

**Experimental details: C2-C$\beta$ dipolar coupling estimation**

To estimate the C2-C$\beta$ dipolar coupling in histidine hydrochloride monohydrate the SA-STARS-3 pulse sequence (Figure 9.3) was applied. Sample spinning was set to 13.10 ± 0.03 kHz at a rotation angle of 53.54 ± 0.05°, thus a magic-angle offset of -1.3°. A duration of 2.5 $\mu$s was calibrated for the $^1$H $\pi$/2-pulse, while the $^1$H $\pi$/2-pulse duration was 3 $\mu$s. 1.25 ms were allowed for cross-polarisation under spin-lock fields of $\omega_{rf}^{1H}/2\pi$ = 48 kHz and $\omega_{rf}^{13C}/2\pi$ = 43 kHz. Heteronuclear decoupling at $\omega_{dec}^{1H}/2\pi$ = 83 kHz was implemented using SPINAL-64 with a pulse duration of 5.2$\mu$s. Selection of the C2 and C$\beta$ sites in the sample was achieved using a dual-band selective cosine modulated Gaussian pulse. It was truncated by 1% and is described by its excitation width $\Delta_G$ = 785 Hz and the Gaussian decay parameter $\alpha = 1.528 \cdot 10^6 s^{-2}$, this gives a Gaussian time shift of $\tau_{sh}$ = 0.84 ms. The z-filter delay during which the rotation angle was switched back to the magic angle was $\tau_z$ = 20ms. The recycle delay was 8 s and 128 transients were recorded for each experiment.

**Experimental details: CO-CO dipolar coupling estimation**

Again the SA-STARS-3 pulse sequence (Figure 9.3) was applied, here, to estimate the internuclear CO-CO dipolar coupling. Under sample spinning at 14.15 ± 0.03 kHz and at a rotation angle of 48.74 ± 0.05°— -6°off-magic an-

gle — the proton $^{1}$H $\pi/2$-pulse length is 2.5 $\mu$s and the respective carbon $\pi/2$-pulse length is 3 $\mu$s. The cross-polarisation nutation frequencies were $\omega_{rf}^{1H}/2\pi$ = 46 kHz and $\omega_{rf}^{13C}/2\pi$ = 43 kHz applied for a contact time of 1.25 ms. SPINAL-64 at $\omega_{dec}^{1H}/2\pi$ = 83 kHz and with a pulse duration of 4.3 $\mu$s was used for heteronuclear decoupling. A single-band frequency selective Gaussian pulse with $\Delta_G$ = 2600 Hz, a decay parameter $\alpha = 16.68 \cdot 10^6 s^{-2}$ and a Gaussian time shift of $\tau_{sh}$ = 0.25 ms was applied to selectively invert the CO-site. The Gaussian was truncated by 1% and the recycle delay was 8 s. 128 transients were recorded for each experiment.

Chapter 13

# Experimental Results

## 13.1. Singly-Labelled Spin System

The STARS-12 sequence is demonstrated on the intermolecular CO-CO coupling in 1-[$^{13}$C]-$\alpha$-glycine (Figure 13.1), in which the strongest CO-CO dipolar coupling is $-254$ Hz (3.1 Å). The CSA tensors of the two considered CO-sites are identical and co-linear [92], thus data analysis uses the analytical ratio derived for the full Hamiltonian ($\phi^f$). Additional to the dominant coupling there are three further distances up tp 5.5 Å with couplings of -101 Hz, -57 Hz and -47 Hz. These couplings result in an effective dipolar coupling of -283 Hz. The recou-

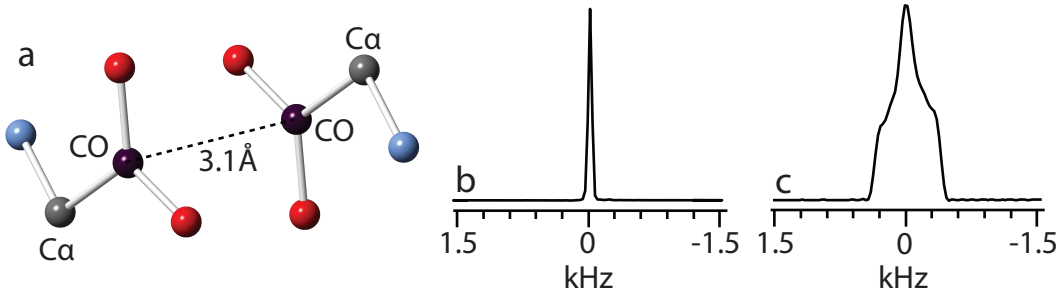


Figure 13.1: a) Two glycine molecules crystallised in the $\alpha$-polymorph (Cambridge structural data base, GLYCIN28) are shown, and the shortest CO-CO distance 3.1 Å ($-254$ Hz) in the crystal structure is indicated. The colour scheme for the atoms is as follows: CO-carbon – black, carbon – grey, nitrogen – blue and oxygen – red. Protons were omitted. b) CP-MAS spectrum of 1-[$^{13}$C]-$\alpha$-glycine at the magic-angle ($\beta_{RL} = 54.74°$). c) CP-MAS spectrum of 1-[$^{13}$C]-$\alpha$-glycine at a rotor-angle of $\beta_{RL} = 52.72°$— a magic-angle offset of $-2°$.

pling of the chemical shift anisotropies by off-magic-angle spinning is depicted

in Figures 13.1.b-c, which show the CO peak observed on the magic-angle and at $-2°$off the magic-angle, respectively. The recombined spectra observed with the STARS-12 experiment are shown in Figure 13.2, a) shows the rank-1 component and b) the rank-2 component. Integration of those peaks leads to the experi-

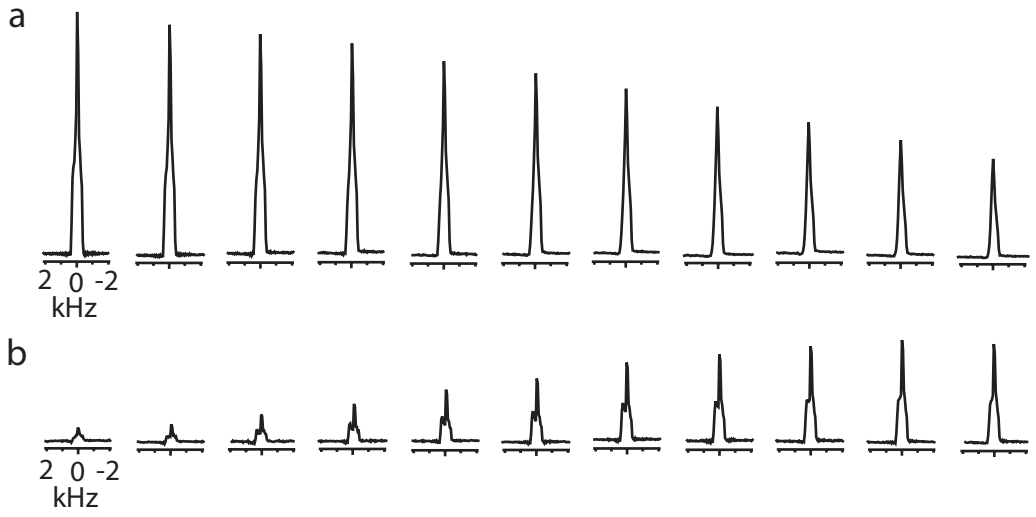


Figure 13.2: Spectra of the recombined STA-12 results on 1-[$^{13}$C]-$\alpha$-glycine obtained at $\beta_{RL} = 52.74 \pm 0.05°$. a) Rank-1 data at increasing echo times. b) Rank-2 data at increasing echo times. The spin-echo evolution times increase from left to right and are for the rank-1 and -2 spectra: 1.4 ms, 4.7 ms, 8.1 ms, 11.4 ms, 14.8 ms, 18.1 ms, 21.5 ms, 24.8 ms, 28.2 ms, 31.6 ms, 34.9 ms.

mental rank-1 and rank-2 spherical signal components shown in Figure 13.3.a, where the rank-1 component decreases while the rank-2 component builds-up slowly. The ratio of both experimental spherical signal components is plotted in Figure 13.3.b along with the best fit of the data to $\phi^f$. The fit yields a dipolar coupling of $-282 \pm 9$ Hz, which is 28 Hz stronger than the calculated coupling for the dominant coupling, and corresponds to a distance that would be 0.1 Å shorter than the one extracted from the crystal structure. However, the coupling to additional spins needs to be considered and, if a cutoff of 5.5 Å is applied, the effective dipolar coupling is very close to the experimentally determined value. Further distances can be taken into account. At a cutoff of 7 Å another seven couplings need to be included into the effective dipolar coupling calculation yielding a coupling of -334 Hz. This coupling is 50 Hz stonger than the experimental value corresponding to 0.3 Å shorter distance. Preliminary analytical fits taking mixed collinear and non-collinear contribution into account yield a fit of -339 Hz if the functions $\phi^f$ and $\phi^t$ are equally weighted and are thus in good agreement with the effective coupling including all distances up to 7 Å. Numerical simulations

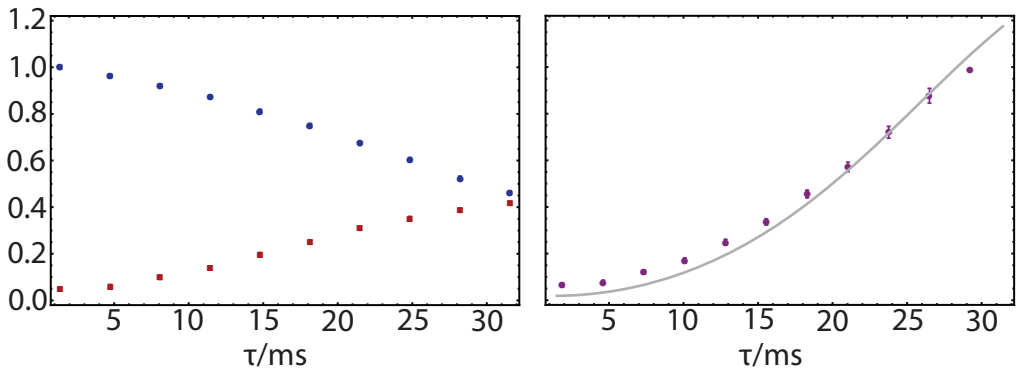


Figure 13.3: STARS-12 results on 1-[$^{13}$C]-$\alpha$-glycine obtained at $\beta_{RL} = 52.74 \pm 0.05°$. a) The experimental rank-1 spherical signal component is visualised by blue dots, while red squares visualise the rank-2 component. The experimental error is smaller than the plot markers. b) The experimental ratio, $\phi^{exp}$, is displayed by purple dots. The grey line corresponds to the best fit with $\phi^{f}$ yielding a dipolar coupling of $-282 \pm 9$ Hz.

which explore the influence of mixed collinear and non-collinear contributions to the analytical expression are currently underway and should give further insight into the appropiate analytical expressions.

Once the dipolar coupling is obtained by fitting data to the ratio in Figure 13.3.b it should be possible to extract the relaxation rate from the rank-1 and rank-2 components shown in Figure 13.3.a. However, no attempts have been made so far to extract those relaxation parameters.

## 13.2. Multiple-Spin System

In the following the performance of the different STARS-sequences when applied to a multiple-spin system, here a powder of U-[$^{13}$C-$^{15}$N]-L-histidine·HCl·$H_2O$, was investigated estimating dipolar couplings of different strength. The effects of a spinning angle offset and selective pulses on U-[$^{13}$C-$^{15}$N]-L-histidine·HCl·-$H_2O$ are shown in Figure 13.4. Figure 13.4.a shows the magic-angle spinning spectrum while b) and c) were acquired using a sample rotation around $\beta_{RL} = 53.94 \pm 0.05°$. To obtain Figure 13.4.c a cosine-modulated Gaussian pulse was used to invert the z-magnetisation of two selected $^{13}$C-peaks, before exciting transverse magnetisation by a $\pi/2$-pulse. This spectrum shows a clean magnetisation inversion for the selected sites.

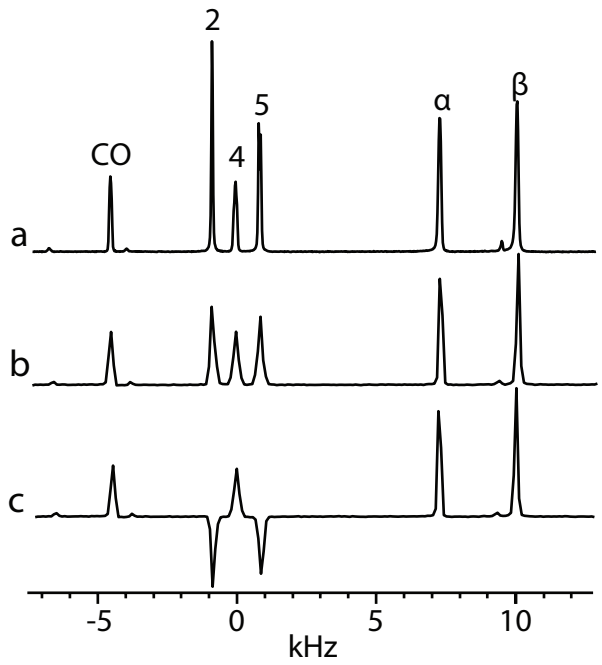


Figure 13.4: Spectra of U-[$^{13}$C-$^{15}$N]-L-histidine·HCl·$H_2O$. a) CP-MAS spectrum at the magic angle. b) CP-MAS spectrum at $\beta_{RL} = 53.94°$, $-0.8°$off-magic- angle. c) as in b) but using a cosine-modulated Gaussian $\pi$-pulse to selectively invert the magnetisation of sites C2 and C5.

Two intramolecular dipolar couplings, the strong C2-C5 ($-715$ Hz) coupling and the CO-C5 ($-251$ Hz) coupling, were estimated utilising the STARS-12 pulse sequence. For both couplings only the dominant interaction was assumed to contribute to the observable coupling as next nearest dipolar couplings are small. This and the non co-linear CSA tensor orientation make $\phi^t$ the appropriate form for data analysis. Build-up curves for rank-1 and -2 spherical signal components as well as the experimental ratios with their best fits are shown in Figure 13.5. Data fits for the C2-C5 ratio estimate a dipolar coupling of $-725 \pm 15$ Hz, which is in excellent agreement with the calculated $-715$ Hz. The CO-C5 dipolar coupling is estimated as $-225 \pm 7$ Hz, thus ~25 Hz weaker than the one inferred from the crystal structure, and corresponds to a distance of 3.23 Å which is 0.11 Å shorter than in the crystal structure.

Reducing the minimum number of transients that need to be recorded for a single data point the STARS-3 sequence was employed to estimate the C$\beta$-C$\beta$ dipolar coupling in U-[$^{13}$C-$^{15}$N]-L-histidine·HCl·$H_2O$. The crystal structure of U-[$^{13}$C-$^{15}$N]-L-histidine·HCl·$H_2O$ shows that C$\beta$ has two nearest C$\beta$ neighbours, each at a distance of 4.78 Å, and two more distant neighbours, each at 6.85 Å. The effective dipolar coupling corresponding to the four nearest C$\beta$ neighbours of a

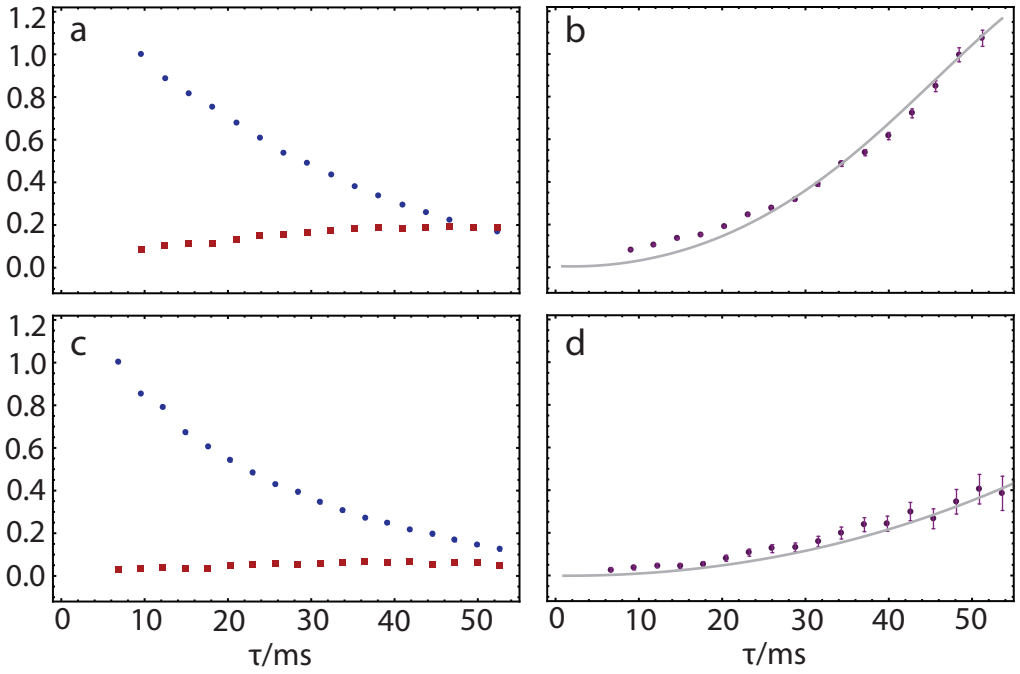


Figure 13.5: STARS-12 results on U-[$^{13}$C-$^{15}$N]-L-histidine·HCl·$H_2O$. a) The spherical signal components obtained for the C2-C5 dipolar coupling by integration over the C2-peak. Data were obtained at $\beta_{RL} = 53.94 \pm 0.05°$. Rank-1 and -2 are visualised be blue dots and red squares, respectively. b) The experimental ratio of rank-2/rank-1 components shown in a) (purple dots) is shown with the best fit to $\phi^t$ (grey line). The best fit yields a dipolar coupling of $-725$ $\pm 15$ Hz. c) Spherical signal components obtained for the CO-C5 dipolar coupling by integration over the CO-peak. Data were obtained at $\beta_{RL} = 53.24 \pm 0.05°$. Rank-1 and -2 are visualised by blue dots and red squares, respectively. d) The experimental ratio of rank-2/rank-1 components shown in c) (purple dots) is shown with the best fit to $\phi^t$ (grey line). The best fit yields a dipolar coupling of $-225$ $\pm 7$ Hz.

given C$\beta$ is $-104$ Hz. This is not significantly altered, if further C$\beta$ neighbours are taken into account. Experimental results are, thus compared to a 5-spin effective dipolar coupling. Fitting of the experimental data, Figure 13.6, was accomplished with the ratio $\phi^{tse}$ and yields a dipolar coupling of $-103 \pm 6$ Hz. This is in excellent agreement with the calculated effective dipolar coupling. The application of weighted analytical expressions show less agreement with the calculated coupling and are not discussed in detail as further research is necessary before they can be readily applied.

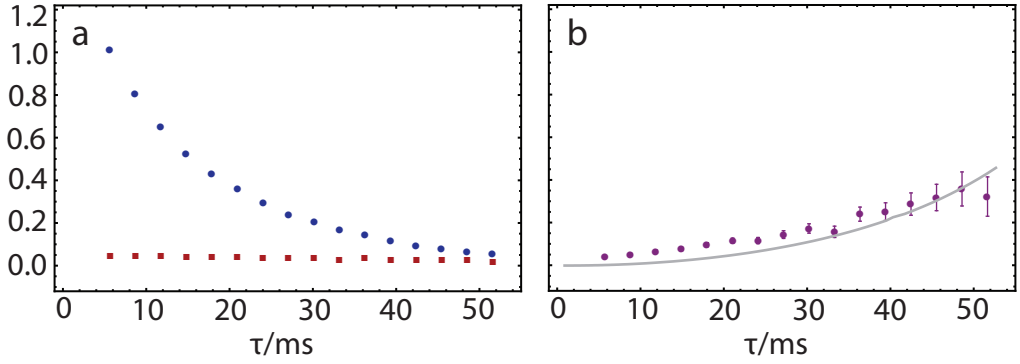


Figure 13.6: STARS-3 results on U-[$^{13}$C-$^{15}$N]-L-histidine·HCl·$H_2O$. a) Spherical signal components obtained for the C$\beta$-C$\beta$ dipolar coupling by integration over the C$\beta$-peak. Data were obtained at $\beta_{RL} = 51.74°$. Rank-1 and -2 are visualised by blue dots and red squares, respectively. b) The experimental ratio of rank-2/rank-1 components shown in a) (purple dots) is shown with the best fit to $\phi^{tse}$ (grey line). The best fit yields a dipolar coupling of $-103 \pm 6$ Hz.

## 13.3. Multiple-Spin System and Switched Angle Spinning

So far, the spectral broadening during data acquisition was tolerable. However, to access long-range dipolar couplings a larger magic-angle offset is required and degrades spectral resolution significantly. Thus, switched-angle-spinning and STARS-3 was combined to SA-STARS-3 to determine the C2-C$\beta$ and the CO-CO dipolar couplings in U-[$^{13}$C-$^{15}$N]-L-histidine·HCl·$H_2O$ (Figure 13.7). Both dipolar coupling estimations were received by fitting the experimental ratios to $\phi^{tse}$ as only effective dipolar couplings are accessible and the CSA tensors are not colinear. The dominant C2-C$\beta$ dipolar coupling corresponds to a crystal structure distance of 3.64 Å yielding a dipolar coupling of $-158$ Hz. Taking into account all C2-C$\beta$ and C$\beta$-C$\beta$ dipolar couplings smaller than 7 Å the effective dipolar coupling for observation on the C$\beta$-peak takes a value of $-220$ Hz. This corresponds well to the observed coupling of $-247 \pm 18$ Hz, consequently the NMR distance is 0.13 Å shorter than the one from X-ray crystallography. Weighted analytical functions with $\frac{2}{3}\phi^{tse} + \frac{1}{3}\phi^{pse}$ yield an effective coupling of $-202 \pm 11$ Hz which is in slightly better agreement with the calculated coupling than the observed by fits to $\phi^{tse}$.

The crystal structure of U-[$^{13}$C-$^{15}$N]-L-histidine·HCl·$H_2O$ shows that each CO site has two nearest neighbours, each at a distance of 5.98 Å, and two more distant neighbours each at a distance of 6.85 Å. The effective dipolar coupling

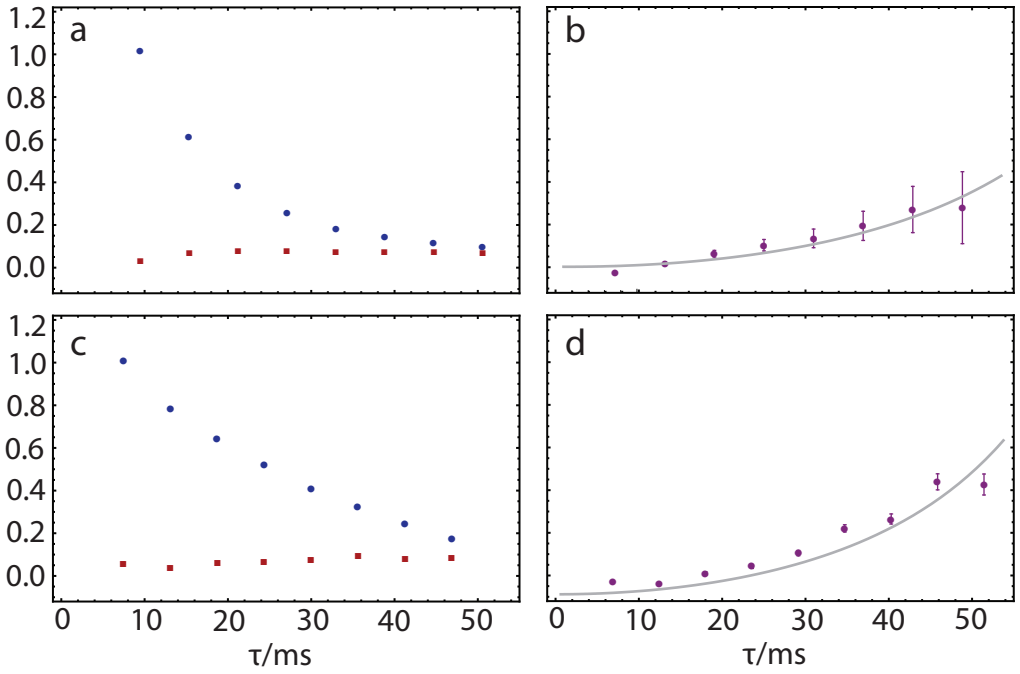


Figure 13.7: SA-STARS-3 results on U-[$^{13}$C-$^{15}$N]-L-histidine·HCl·$H_2O$. a) The spherical signal components obtained for the C2-C$\beta$ dipolar coupling by integration over the C$\beta$-peak. Data were obtained at $\beta_{RL} = 53.54°$. Rank-1 and -2 are visualised be blue dots and red squares, respectively. b) The experimental ratio of rank-2/rank-1 components shown in a) (purple dots) is shown with the best fit to $\phi^{tse}$ (grey line). The best fit yields a dipolar coupling of −247 ±18 Hz. c) Spherical signal components obtained for the CO-CO dipolar coupling by integration over the CO-peak. Data were obtained at $\beta_{RL} = 48.74°$. Rank-1 and -2 are visualised by blue dots and red squares, respectively. d) The experimental ratio of rank-2/rank-1 components shown in c) (purple dots) is shown with the best fit to $\phi^{tse}$ (grey line). The best fit yields a dipolar coupling of −54 ±3 Hz.

including the four nearest neighbours to a given CO-site is -60 Hz. However, if the twelve nearest neighbours, all at a distance smaller than 8 Å, are taken into account the calculated effective coupling yields −83 Hz. For a fit of the experimental CO-CO-ratio with $\phi^{tse}$ a coupling of −54 ± 4 Hz is determined, if the same distance is fitted to $\frac{2}{3}\phi^{tse}+\frac{1}{3}\phi^{pse}$ a coupling of −81 ± 2 Hz is determined. The later one is in good agreement with the calculated coupling.

Weighted analytical functions wich take into account mixed colinnear and non-collinear tensors have been applied. However, they seem to improve results just in some cases while the the match with the calculated effetive coupling starts to deviate more in other cases. Thus, these results should be treated with caution until they can be backed by numerical simulations.

Chapter 14

# Discussion

In the previous chapter experimental results estimating dipolar couplings of different strength were reported. For experiments on a singly labelled spin-system as well as in a multiple-spin systems precise distances could be determined in cases with individual dipolar couplings as weak as $-70$ Hz. Furthermore, weak effective dipolar couplings of $-104$ Hz were accessible yielding precise quantitative results. Thus, the presented STARS methodology allows estimations of biologically relevant internuclear distances between $4-5$ Å which deviate less than 12% from those obtained be X-ray crystallography. However, the CO-CO distance in histidine hydrochloride monohydrate which exhibits an effective coupling of -83 Hz could not be determined precisely. Thus it is concluded that effective dipolar couplings which exclusively include long-range couplings corresponding to distances above 6 Å cannot yet be determined precisely.

The spinning instabilities reported in Chapter 12 have no observable influence on the acquired data, because the dipolar recoupling mechanism does not rely on rotor synchronisation. This robustness with respect to spinning instabilities is a major advantage of the presented work over many recoupling sequences, such as REDOR [17; 94], which rely heavily on rotor synchronisation to accomplish recoupling.

If the results are examined closely it is apparent that experimental data points show a horizontal offset compared to the analytical solutions at small evolution times $\tau$. This effect is attributed to imperfections of the selective pulse.

The extension from the off-magic angle experiment to the switched-angle exper-

iment is not any more difficult to perform once the sequence is programmed.

However, the angle-switching adds some time, the z-filter, to the experiment. This results from the time needed for the angle to stabilise in its new position and takes minimum time of 20 ms. To avoid spin-diffusion during the z-filter it is necessary to apply proton decoupling, this can result in timing problems for probes which have conservative decoupling times. The experiments shown apply decoupling for 80 ms and the probe is specified for decoupling at 120 kHz for up to 150 ms.

Chapter 15

# Conclusions and Final Remarks

A new method that is insensitive to incoherent relaxation effects and may be used to estimate weak dipolar couplings in the presence of strong dipolar couplings was introduced. Weak internuclear $^{13}$C dipolar couplings between nuclei at distances between $4-5$ Å are estimated precisely. Thus, a significant progress towards the general solution of the estimation of structurally relevant long-range dipolar couplings has been demonstrated. Here, quantitative distance estimation were provided in contrast to most other techniques addressing the problem [21; 25; 27; 28; 29; 30; 31; 51; 95] and in a range between $4-5$ Å deviations from X-ray crystallography were no larger that 0.13 Å.

STARS is a frequency selective method which does not suffer from dipolar truncation as it is observed for many common dipolar recoupling sequences such as RFDR, SR4$^1_4$, DRAWS and R12$^5_2$ [22] when applied to multiple-spin systems. Employing STARS it is possible to precisely determine effective dipolar couplings that resemble an internuclear distance of 4.2 Å while much stronger couplings due to single bonds are present.

Compared to RR experiments in multiple-spin systems distances within an equivalent range can be determined with both techniques [51; 52]. Both techniques require a good chemical shift resolution —RR at the magic angle and STARS off-magic angle — to allow for selection of the desired couplings. The required chemical shift resolution is a disadvantage of both methods, which can be overcome for RR by going to higher magnetic fields. STARS has the advantage that the recoupling mechanism does not depend on the spinning speed and is thus robust with respect to spinning speed fluctuations during the experiment.

STARS is part of the recently emerging class of dipolar coupling sequences, that try to tackle dipolar truncation. SEASHORE has been applied to uniformly labelled alanine and uniformly labelled amyloid fibrils in which a maximum distance of 3.9 Å was determined [25]. TDR has so far only yielded a distance of 2.5 Å in U-$^{13}$C,$^{15}$N,$^{7}H$-L-alanine. This is a rather short distance and it is necessary to deuterate the sample to avoid interference from undesired heteronuclear interactions [26]. SDR has been applied to two and five spin systems, but no distances have been estimated and thus the precision of the sequence is difficult to judge. In the laboratory of N. Nielsen TOFU and FOLD [29; 30] have been developed. These sequences use several oscillating fields to truncate the flip-flop term in the homonuclear dipolar Hamiltonian. Distances in the range of $4-5$ Å with a deviation of $\pm 0.2$ Å were obtained for multiple spin systems in uniformly $^{13}$C labelled samples of L-alanine, L-threonine and ubiquitine. However, the distances were estimated by visual comparison to a Fresnel grid thus are more ambiguous than if data are fitted to an analytical solution. Employing the STARS-experiment it is possible to determine longer couplings than those estimated for SEASHORE and TDR [25; 26]. Other than for TOFU and FOLD an analytical formula could be derived for STARS which allows a robust estimation of the dipolar couplings from the obtained data [29; 30].

The STARS sequence has the advantage of being robust with respect to spinning instabilities. Furthermore, the analytical formulae provided allow unambiguous distance estimations. However, a high chemical shift resolution off-magic angle is necessary to allow the selective inversion of a desired spin-pair and makes selective inversion in crowded spectral regions difficult. Hence, magic angle techniques might yield more precise distances if the chemical shift resolution is low. Especially for the switched-angle experiment long decoupling times are necessary, which can be problematic for some probes. The ideal probe for these experiments allows decoupling at at least 100 kHz for 120 ms as well as very short settling times after the magic angle switching. The settling times of 20 ms observed using the servo-controller are similar to those observed for a pneumatic angle switching mechanism developed in the laboratory of R. Martin [96]. No difficulties regarding the shimming or the spinning speed stabilities during angle switching are observed.

Future developments for this methodology include the refinement of the selective pulse, and the extension of the methodology to a higher dimensional scheme to provide enough resolution to apply this methodology to larger systems such as

proteins. Additionally, a different set of Euler angles to implement the STA-procedure has been suggested by Michael Tayler (personal communication) that has a favourable scaling of the rank-2 spherical signal component, hence, would allow a stronger signal.

Appendix A

# Irreducible Spherical Spin Tensor Operators

## 1.1. Single Spin

The irreducible spherical tensor operators $T^j_{\lambda\mu}$ are:

$$T^j_{10} = S_{jz} \tag{A.1}$$

$$T^j_{1\pm1} = \mp\frac{1}{\sqrt{2}} S^{\pm}_j \tag{A.2}$$

## 1.2. Two Spins

The irreducible spherical tensor operators $T^{jk}_{\lambda\mu}$ for two spins are as follows:

$$T^{jk}_{00} = -\frac{1}{\sqrt{3}} S_j \cdot S_k \tag{A.3}$$

$$T^{jk}_{10} = \frac{1}{2\sqrt{2}} \left( S^+_j S^-_k - S^-_j S^+_k \right) \tag{A.4}$$

$$T^{jk}_{1\pm1} = \frac{1}{2} \left( S^{\pm}_j S_{kz} - S_{jz} S^{\pm}_k \right) \tag{A.5}$$

$$T^{jk}_{20} = \frac{1}{\sqrt{6}} \left( 3 S_{jz} S_{kz} - S_j \cdot S_k \right) \tag{A.6}$$

$$T^{jk}_{2\pm1} = \mp\frac{1}{2}\left(S^{\pm}_{j}S_{kz} + S_{jz}S^{\pm}_{k}\right) \tag{A.7}$$

$$T^{jk}_{2\pm2} = \frac{1}{2}S^{\pm}_{j}S^{\pm}_{k} \tag{A.8}$$

# Bibliography


[1] E. M. Purcell, H. C. Torrey, and R. V. Pound, "Resonance Absorption by Nuclear Magnetic Moments in a Solid," *Physical Review*, vol. 69, no. 1-2, pp. 37–38, 1946.

[2] F. Bloch, W. W. Hansen, and M. Packard, "Nuclear Induction," *Physical Review*, vol. 69, no. 3-4, pp. 127–127, 1946.

[3] E. R. Andrew and E. Szczesniak, "A historical account of NMR in the solid state," *Progress in Nuclear Magnetic Resonance Spectroscopy*, vol. 28, no. 1, pp. 11–36, 1995.

[4] E. R. Andrew, A. Bradbury, and R. G. Eades, "Nuclear Magnetic Resonance Spectra from a Crystal rotated at High Speed," *Nature*, vol. 182, pp. 1659–1659, Dec. 1958.

[5] E. R. Andrew, A. Bradbury, Y, and R. G. Eades, "Removal of Dipolar Broadening of Nuclear Magnetic Resonance Spectra of Solids by Specimen Rotation," *Nature*, vol. 183, pp. 1802–1803, June 1959.

[6] I. Lowe, "Free Induction Decays of Rotating Solids," *Physical Review Letters*, vol. 2, pp. 285–287, Apr. 1959.

[7] M. Mehring, *Principles of high resolution NMR in solids*. Springer-Verlag, second ed., 1983.

[8] A. E. Bennett, C. M. Rienstra, M. Auger, K. V. Lakshmi, and R. G. Griffin, "Heteronuclear decoupling in rotating solids," *The Journal of Chemical Physics*, vol. 103, no. 16, p. 6951, 1995.

[9] B. M. Fung, A. K. Khitrin, and K. Ermolaev, "An improved broadband decoupling sequence for liquid crystals and solids.," *Journal of Magnetic Resonance*, vol. 142, pp. 97–101, Jan. 2000.

[10] M. Ernst, "Heteronuclear spin decoupling in solid-state NMR under magic-angle sample spinning," *Journal of Magnetic Resonance*, vol. 162, pp. 1–34, May 2003.

[11] P. Hodgkinson, "Heteronuclear decoupling in the NMR of solids," *Progress in Nuclear Magnetic Resonance Spectroscopy*, vol. 46, pp. 197–222, Sept. 2005.

[12] R. S. Thakur, N. D. Kurur, and P. K. Madhu, "An analysis of phase-modulated heteronuclear dipolar decoupling sequences in solid-state nuclear magnetic resonance.," *Journal of Magnetic Resonance*, vol. 193, pp. 77–88, July 2008.

[13] A. Pines, M. G. Gibby, and J. S. Waugh, "Proton-Enhanced Nuclear Induction Spectroscopy. A Method for High Resolution NMR of Dilute Spins in Solids," *The Journal of Chemical Physics*, vol. 56, p. 1776, Dec. 1972.

[14] S. Hartmann and E. Hahn, "Nuclear Double Resonance in the Rotating Frame," *Physical Review*, vol. 128, pp. 2042–2053, Dec. 1962.

[15] J. Schaefer and E. O. Stejskal, "Carbon-13 nuclear magnetic resonance of polymers spinning at the magic angle," *Journal of the American Chemical Society*, vol. 98, pp. 1031–1032, Feb. 1976.

[16] T. G. Oas, R. G. Griffin, and M. H. Levitt, "Rotary resonance recoupling of dipolar interactions in solid-state nuclear magnetic resonance spectroscopy," *The Journal of Chemical Physics*, vol. 89, no. 2, p. 692, 1988.

[17] T. Gullion and J. Schaefer, "Rotational-echo double-resonance NMR," *Journal of Magnetic Resonance*, vol. 81, pp. 196–200, Jan. 1989.

[18] R. Tycko and G. Dabbagh, "Measurement of nuclear magnetic dipole-dipole couplings in magic angle spinning NMR," *Chemical Physics Letters*, vol. 173, pp. 461–465, Oct. 1990.

[19] R. Tycko and G. Dabbagh, "Double-quantum filtering in magic-angle-spinning NMR spectroscopy: an approach to spectral simplification and molecular structure determination," *Journal of the American Chemical Society*, vol. 113, pp. 9444–9448, Dec. 1991.

[20] R. Tycko and S. O. Smith, "Symmetry principles in the design of pulse sequences for structural measurements in magic angle spinning nuclear magnetic resonance," *The Journal of Chemical Physics*, vol. 98, no. 2, p. 932, 1993.

[21] V. Ladizhansky, "Homonuclear dipolar recoupling techniques for structure determination in uniformly 13C-labeled proteins.," *Solid state nuclear magnetic resonance*, vol. 36, no. 3, pp. 119–128, 2009.

[22] M. J. Bayro, M. Huber, R. Ramachandran, T. C. Davenport, B. H. Meier, M. Ernst, and R. G. Griffin, "Dipolar truncation in magic-angle spinning NMR recoupling experiments," *The Journal of Chemical Physics*, vol. 130, no. 11, 2009.

[23] F. Castellani, B. J. Van Rossum, A. Diehl, M. Schubert, K. Rehbein, and H. Oschkinat, "Structure of a protein determined by solid-state magic-angle-spinning NMR spectroscopy," *Nature*, vol. 420, no. 6911, pp. 98–102, 2002.

[24] V. Ladizhansky and R. G. Griffin, "Band-selective carbonyl to aliphatic side chain 13C-13C distance measurements in U-13C,15N-labeled solid peptides by magic angle spinning NMR.," *Journal of the American Chemical Society*, vol. 126, pp. 948–58, Jan. 2004.

[25] A. K. Paravastu and R. Tycko, "Frequency-selective homonuclear dipolar recoupling in solid state NMR.," *The Journal of Chemical Physics*, vol. 124, no. 19, p. 194303, 2006.

[26] I. Marin-Montesinos, G. Mollica, M. Carravetta, A. Gansmuller, G. Pileio, M. Bechmann, A. Sebald, and M. H. Levitt, "Truncated dipolar recoupling in solid-state nuclear magnetic resonance," *Chemical Physics Letters*, vol. 432, pp. 572–578, Dec. 2006.

[27] R. Tycko, "Stochastic Dipolar Recoupling in Nuclear Magnetic Resonance of Solids," *Physical Review Letters*, vol. 99, no. 18, pp. 1–4, 2007.

[28] R. Tycko, "Theory of stochastic dipolar recoupling in solid-state nuclear magnetic resonance.," *The Journal of Physical Chemistry B*, vol. 112, pp. 6114–21, May 2008.

[29] N. Khaneja and N. C. Nielsen, "Triple oscillating field technique for accurate distance measurements by solid-state NMR.," *The Journal of Chemical Physics*, vol. 128, no. 1, p. 015103, 2008.

[30] L. A. Straasø, M. Bjerring, N. Khaneja, and N. C. Nielsen, "Multiple-oscillating-field techniques for accurate distance measurements by solid-state NMR.," *The Journal of Chemical Physics*, vol. 130, no. 22, p. 225103, 2009.

[31] K.-N. Hu and R. Tycko, "Zero-quantum frequency-selective recoupling of homonuclear dipole-dipole interactions in solid state nuclear magnetic resonance.," *The Journal of Chemical Physics*, vol. 131, p. 045101, July 2009.

[32] M. H. Levitt, *Spin dynamics: basics of nuclear magnetic resonance*. Chichester: John Wiley & Sons, first ed., 2001.

[33] M. E. Rose, *Elementary theory of angular momentum*. New York: Dover Publications, Inc., 1995.

[34] K. J. Harris, D. L. Bryce, and R. E. Wasylishen, "NMR line shapes from AB spin systems in solids - The role of antisymmetric spin-spin coupling," *Canadian Journal of Chemistry*, vol. 87, no. 10, pp. 1338–1351, 2009.

[35] U. Haeberlen and J. Waugh, "Coherent Averaging Effects in Magnetic Resonance," *Physical Review*, vol. 175, pp. 453–467, Nov. 1968.

[36] U. Haeberlen, *High resolution NMR in Solids. Selective Averaging.* New York: Academic Press, 1976.

[37] W. Magnus, "On the exponential solution of differential equations for a linear operator," *Communications on Pure and Applied Mathematics*, vol. 7, pp. 649–673, Nov. 1954.

[38] M. M. Maricq, "Application of average Hamiltonian theory to the NMR of solids," *Physical Review B*, vol. 25, pp. 6622–6632, June 1982.

[39] "Wolfram Mathworld," *http://mathworld.wolfram.com/*, 2010.

[40] N. Pyper, "Theory of symmetry in nuclear magnetic relaxation including applications to high resolution N.M.R. line shapes," *Molecular Physics*, vol. 21, pp. 1–33, Jan. 1971.

[41] N. Pyper, "Theory of symmetry in nuclear magnetic relaxation," *Molecular Physics*, vol. 22, no. 3, pp. 433–458, 1971.

[42] J. Jenner, "Superoperators in magnetic resonance," *Advances in Magnetic Resonance*, vol. 10, pp. 1–51, 1982.

[43] X. Feng, Y. Lee, D. Sandstrom, M. Eden, H. Maisel, A. Sebald, and M. Levitt, "Direct determination of a molecular torsional angle by solid-state NMR," *Chemical Physics Letters*, vol. 257, pp. 314–320, July 1996.

[44] D. Raleigh, M. H. Levitt, and R. G. Griffin, "Rotational resonance in solid state NMR," *Chemical Physics Letters*, vol. 146, pp. 71–76, Apr. 1988.

[45] A. E. Bennett, R. G. Griffin, J. H. Ok, and S. Vega, "Chemical shift correlation spectroscopy in rotating solids: Radio frequency-driven dipolar recoupling and longitudinal exchange," *The Journal of Chemical Physics*, vol. 96, no. 11, p. 8624, 1992.

[46] A. E. Bennett, C. M. Rienstra, J. M. Griffiths, W. Zhen, P. T. Lansbury, and R. G. Griffin, "Homonuclear radio frequency-driven recoupling in rotating solids," *The Journal of Chemical Physics*, vol. 108, no. 22, p. 9463, 1998.

[47] Y. K. Lee, N. D. Kurur, M. Helmle, O. G. Johannessen, N. C. Nielsen, and M. H. Levitt, "Efficient dipolar recoupling in the NMR of rotating solids. A sevenfold symmetric radiofrequency pulse sequence," *Chemical Physics Letters*, vol. 242, pp. 304–309, Aug. 1995.

[48] M. Hohwy, H. J. Jakobsen, M. Eden, M. H. Levitt, and N. C. Nielsen, "Broadband dipolar recoupling in the nuclear magnetic resonance of rotating solids: A compensated C7 pulse sequence," *The Journal of Chemical Physics*, vol. 108, no. 7, p. 2686, 1998.

[49] M. H. Levitt, *Symmetry-Based Pulse Sequences in Magic-Angle Spinning Solid-State NMR Symmetry-Based Pulse Sequences in Magic-Angle Spinning Solid-State NMR*, vol. 9, pp. 165–196. Chichester: John Wiley & Sons, 2002.

[50] A. T. Petkova and R. Tycko, "Rotational resonance in uniformly 13C-labeled solids: effects on high-resolution magic-angle spinning NMR spectra and applications in structural studies of biomolecular systems.," *Journal of magnetic resonance (San Diego, Calif. : 1997)*, vol. 168, pp. 137–46, May 2004.

[51] P. T. F. Williamson, A. Verhoeven, M. Ernst, and B. H. Meier, "Determination of internuclear distances in uniformly labeled molecules by rotational-resonance solid-state NMR.," *Journal of the American Chemical Society*, vol. 125, pp. 2718–22, Mar. 2003.

[52] A. Verhoeven, P. T. F. Williamson, H. Zimmermann, M. Ernst, and B. H. Meier, "Rotational-resonance distance measurements in multi-spin systems.," *Journal of Magnetic Resonance*, vol. 168, pp. 314–26, June 2004.

[53] D. M. Gregory, D. J. Mitchell, J. A. Stringer, S. R. Kiihne, J. C. Shiels, J. Callahan, M. Mehta, and G. P. Drobny, "Windowless dipolar recoupling: the detection of weak dipolar couplings between spin 1/2 nuclei with large chemical shift anisotropies," *Chemical Physics Letters*, vol. 246, pp. 654–663, Dec. 1995.

[54] N. C. Nielsen, H. BildsoÌÿe, H. J. Jakobsen, and M. H. Levitt, "Double-quantum homonuclear rotary resonance: Efficient dipolar recovery in magic-angle spinning nuclear magnetic resonance," *The Journal of Chemical Physics*, vol. 101, no. 3, p. 1805, 1994.

[55] C. M. Rienstra, M. E. Hatcher, L. J. Mueller, S. W. Fesik, and R. G. Griffin, "Efficient Multispin Homonuclear Double-Quantum Recoupling for Magic-Angle Spinning NMR: 13 CâĹŠ 13 C Correlation Spectroscopy of U- 13 C-Erythromycin A," *Journal of the American Chemical Society*, vol. 120, pp. 10602–10612, Oct. 1998.

[56] R. Verel, M. Ernst, and B. H. Meier, "Adiabatic dipolar recoupling in solid-state NMR: the DREAM scheme.," *Journal of Magnetic Resonance*, vol. 150, pp. 81–99, May 2001.

[57] M. H. Levitt, "Symmetry-based pulse sequences in magic-angle spinning solid-state NMR," *Encyclopidia of Nuclear Magnetic Resonance*, vol. Supplement, pp. 165–196, 2002.

[58] M. J. Duer, *Introduction to solid-state NMR spectroscopy*. Oxford: Blackwell Publishing Ltd, 2004.

[59] L. Duma, W. C. Lai, M. Carravetta, L. Emsley, S. P. Brown, and M. H. Levitt, "Principles of spin-echo modulation by J-couplings in magic-angle-spinning solid-state NMR.," *Chemical Physics and Physical Chemistry*, vol. 5, pp. 815–33, June 2004.

[60] G. Pileio, Y. Guo, T. N. Pham, J. M. Griffin, M. H. Levitt, and S. P. Brown, "Residual dipolar couplings by off-magic-angle spinning in solid-state nuclear magnetic resonance spectroscopy.," *Journal of the American Chemical Society*, vol. 129, pp. 10972–3, Sept. 2007.

[61] G. Pileio, S. Mamone, G. Mollica, I. M. Montesinos, A. Gansmüller, M. Carravetta, S. P. Brown, and M. H. Levitt, "Estimation of internuclear couplings in the solid-state NMR of multiple-spin systems. Selective spin echoes and off-magic-angle sample spinning," *Chemical Physics Letters*, vol. 456, pp. 116–121, Apr. 2008.

[62] R. R. Ernst, G. Bodenhausen, and A. Wokaun, *Principles of Nuclear Magnetic Resonance in One and Two Dimensions*. Oxford: Clarendon Press, 1990.

[63] R. Tycko, "Normal Angle Spinning Dipolar Spectroscopy for Structural Studies by Solid-State Nuclear Magnetic Resonance," *Journal of the American Chemical Society*, vol. 116, pp. 2217–2218, Mar. 1994.

[64] A. C. Kolbert, P. J. Grandinetti, M. Baldwin, S. B. Prusiner, and A. Pines, "Measurement of Internuclear Distances by Switched Angle Spinning NMR," *The Journal of Physical Chemistry*, vol. 98, pp. 7936–7938, Aug. 1994.

[65] R. G. Griffin, "Dipolar recoupling in MAS spectra of biological solids.," *Nature structural biology*, vol. 5 Suppl, pp. 508–12, July 1998.

[66] P. R. Costa, B. Sun, and R. G. Griffin, "Rotational Resonance Tickling: Accurate Internuclear Distance Measurement in Solids," *Journal of the American Chemical Society*, vol. 119, pp. 10821–10830, Nov. 1997.

[67] J. Spano and S. Wi, "Dipolar-coupling-mediated total correlation spectroscopy in solid-state (13)C NMR: Selection of individual (13)C-(13)C dipolar interactions.," *Journal of Magnetic Resonance*, vol. 204, pp. 314–326, Mar. 2010.

[68] Y. Ishii, J. J. Balbach, and R. Tycko, "Measurement of dipole-coupled lineshapes in a many-spin system by constant-time two-dimensional solid state NMR with high-speed magic-angle spinning," *Chemical Physics*, vol. 266, pp. 231–236, May 2001.

[69] A. Grommek, B. H. Meier, and M. Ernst, "Distance information from proton-driven spin diffusion under MAS," *Chemical Physics Letters*, vol. 427, pp. 404–409, Aug. 2006.

[70] N. Tjandra and A. Bax, "Direct Measurement of Distances and Angles in Biomolecules by NMR in a Dilute Liquid Crystalline Medium," *Science*, vol. 278, pp. 1111–1114, Nov. 1997.

[71] M. Blackledge, "Recent progress in the study of biomolecular structure and dynamics in solution from residual dipolar couplings," *Progress in Nuclear Magnetic Resonance Spectroscopy*, vol. 46, pp. 23–61, Mar. 2005.

[72] R. S. Lipsitz and N. Tjandra, "Residual dipolar couplings in NMR structure analysis.," *Annual review of biophysics and biomolecular structure*, vol. 33, pp. 387–413, Jan. 2004.

[73] L. Duma, D. Abergel, P. Tekely, and G. Bodenhausen, "Proton chemical shift anisotropy measurements of hydrogen-bonded functional groups by fast magic-angle spinning solid-state NMR spectroscopy," *Chem.Commun.*, no. 20, pp. 2361–2363, 2008.

[74] T. Terao, H. Miura, and A. Saika, "Dipolar SASS NMR spectroscopy: Separation of heteronuclear dipolar powder patterns in rotating solids," *The Journal of Chemical Physics*, vol. 85, no. 7, p. 3816, 1986.

[75] L. Frydman, G. C. Chingas, Y. K. Lee, P. J. Grandinetti, M. A. Eastman, G. A. Barrall, and A. Pines, "Variable-angle correlation spectroscopy in solid-state nuclear magnetic resonancea)," *The Journal of Chemical Physics*, vol. 97, no. 7, p. 4800, 1992.

[76] C. Qian, P. Thureau, and R. W. Martin, "Variable angle spinning (VAS) experiments for strongly oriented systems: methods development and preliminary results," *Magnetic Resonance in Chemistry*, vol. 46, no. 4, pp. 351–355, 2008.

[77] G. Zandomeneghi, P. T. F. Williamson, A. Hunkeler, and B. H. Meier, "Switched-angle spinning applied to bicelles containing phospholipid-associated peptides.," *Journal of Biomolecular NMR*, vol. 25, pp. 125–32, Feb. 2003.

[78] R. H. Havlin, G. H. J. Park, T. Mazur, and A. Pines, "Using switched angle spinning to simplify NMR spectra of strongly oriented samples.," *Journal of the American Chemical Society*, vol. 125, pp. 7998–8006, July 2003.

[79] J. D. van Beek, M. Carravetta, G. C. Antonioli, and M. H. Levitt, "Spherical tensor analysis of nuclear magnetic resonance signals.," *The Journal of Chemical Physics*, vol. 122, no. 24, p. 244510, 2005.

[80] M. C. D. Tayler, "Signal-to-noise sensitivity within spherical-tensor based schemes of phase cycling." 2009.

[81] M. H. Levitt, *An orientational sampling scheme for magnetic resonance based on a four-dimensional polytope*, pp. 1–20. 2009.

[82] V. E. Zorin, S. P. Brown, and P. Hodgkinson, "Quantification of homonuclear dipolar coupling networks from magic-angle spinning 1 H NMR," *Molecular Physics*, vol. 104, pp. 293–304, Jan. 2006.

[83] C. Filip, S. Hafner, I. Schnell, D. E. Demco, and H. W. Spiess, "Solid-state nuclear magnetic resonance spectra of dipolar-coupled multi-spin systems under fast magic angle spinning," *The Journal of Chemical Physics*, vol. 110, no. 1, p. 423, 1999.

[84] J. Schmedt auf der Günne, "Effective dipolar couplings determined by dipolar dephasing of double-quantum coherences.," *Journal of Magnetic Resonance*, vol. 180, pp. 186–96, June 2006.

[85] M. Aluas, C. Tripon, J. M. Griffin, X. Filip, V. Ladizhansky, R. G. Griffin, S. P. Brown, and C. Filip, "CHHC and 1H-1H magnetization exchange: analysis by experimental solid-state NMR and 11-spin density-matrix simulations.," *Journal of Magnetic Resonance*, vol. 199, pp. 173–87, Aug. 2009.

[86] I. Hung, A.-C. Uldry, J. Becker-Baldus, A. L. Webber, A. Wong, M. E. Smith, S. A. Joyce, J. R. Yates, C. J. Pickard, R. Dupree, and S. P. Brown, "Probing heteronuclear (15)N-(17)O and (13)C-(17)O connectivities and proximities by solid-state NMR spectroscopy.," *Journal of the American Chemical Society*, vol. 131, pp. 1820–34, Feb. 2009.

[87] A. Lesage, M. Bardet, and L. Emsley, "Through-Bond CarbonâĹŠCarbon Connectivities in Disordered Solids by NMR," *Journal of the American Chemical Society*, vol. 121, pp. 10987–10993, Dec. 1999.

[88] S. Cadars, J. Sein, L. Duma, A. Lesage, T. N. Pham, J. H. Baltisberger, S. P. Brown, and L. Emsley, "The refocused INADEQUATE MAS NMR experiment in multiple spin-systems: interpreting observed correlation peaks and optimising lineshapes.," *Journal of Magnetic Resonance*, vol. 188, pp. 24–34, Sept. 2007.

[89] G. Pileio, S. Mamone, G. Mollica, I. M. Montesinos, A. Gansmüller, M. Carravetta, S. P. Brown, and M. H. Levitt, "Estimation of internuclear couplings in the solid-state NMR of multiple-spin systems. Selective spin echoes and off-magic-angle sample spinning," *Chemical Physics Letters*, vol. 456, pp. 116–121, Apr. 2008.

[90] M. H. Levitt, "mPackages," *http://www.mhl.soton.ac.uk/public/-Main/software/mPackages/index.html*.

[91] C. Ye, R. Fu, J. Hu, L. Hou, and S. Ding, "Carbon-13 chemical shift anisotropies of solid amino acids," *Magnetic Resonance in Chemistry*, vol. 31, pp. 699–704, Aug. 1993.

[92] R. A. Haberkorn, R. E. Stark, H. Van Willigen, and R. G. Griffin, "Determination of bond distances and bond angles by solid-state nuclear magnetic resonance. Carbon-13 and nitrogen-14 NMR study of glycine," *Journal of the American Chemical Society*, vol. 103, pp. 2534–2539, May 1981.

[93] S. Mamone, A. Dorsch, O. G. Johannessen, M. V. Naik, P. K. Madhu, and M. H. Levitt, "A Hall effect angle detector for solid-state NMR.," *Journal of Magnetic Resonance*, vol. 190, pp. 135–41, Jan. 2008.

[94] C. P. Jaroniec, *Dipolar Recoupling: Heteronuclear*. Chichester: John Wiley & Sons, Ltd, 2009.

[95] R. Tycko, "Symmetry-based constant-time homonuclear dipolar recoupling in solid state NMR.," *The Journal of Chemical Physics*, vol. 126, no. 6, p. 064506, 2007.

[96] I. M. Litvak, C. A. Espinosa, R. A. Shapiro, A. N. Oldham, V. V. Duong, and R. W. Martin, "Pneumatic switched angle spinning NMR probe with capacitively coupled double saddle coil.," *Journal of Magnetic Resonance*, vol. 206, pp. 183–9, Oct. 2010.